



National Library  
of Canada

Bibliothèque nationale  
du Canada

Canadian Theses Service

Service des thèses canadiennes

Ottawa, Canada  
K1A 0N4

## NOTICE

The quality of this microform is heavily dependent upon the quality of the original thesis submitted for microfilming. Every effort has been made to ensure the highest quality of reproduction possible.

If pages are missing, contact the university which granted the degree.

Some pages may have indistinct print especially if the original pages were typed with a poor typewriter ribbon or if the university sent us an inferior photocopy.

Reproduction in full or in part of this microform is governed by the Canadian Copyright Act, R.S.C. 1970, c. C-30, and subsequent amendments.

## AVIS

La qualité de cette microforme dépend grandement de la qualité de la thèse soumise au microfilmage. Nous avons tout fait pour assurer une qualité supérieure de reproduction.

S'il manque des pages, veuillez communiquer avec l'université qui a conféré le grade.

La qualité d'impression de certaines pages peut laisser à désirer, surtout si les pages originales ont été dactylographiées à l'aide d'un ruban usé ou si l'université nous a fait parvenir une photocopie de qualité inférieure.

La reproduction, même partielle, de cette microforme est soumise à la Loi canadienne sur le droit d'auteur, SRC 1970, c. C-30, et ses amendements subséquents.

INTERACTIONS BETWEEN PHYSICAL AND  
BIOLOGICAL PROCESSES IN THE EQUATORIAL  
PACIFIC

By  
Mary-Elena Carr

SUBMITTED IN PARTIAL FULFILLMENT OF THE  
REQUIREMENTS FOR THE DEGREE OF  
DOCTOR OF PHILOSOPHY  
AT  
DALHOUSIE UNIVERSITY  
HALIFAX, NOVA SCOTIA  
SEPTEMBER 1991

© Copyright by Mary-Elena Carr, 1991



National Library  
of Canada

Bibliothèque nationale  
du Canada

Canadian Theses Service    Service des thèses canadiennes

Ottawa, Canada  
K1A 0N4

The author has granted an irrevocable non-exclusive licence allowing the National Library of Canada to reproduce, loan, distribute or sell copies of his/her thesis by any means and in any form or format, making this thesis available to interested persons.

The author retains ownership of the copyright in his/her thesis. Neither the thesis nor substantial extracts from it may be printed or otherwise reproduced without his/her permission.

L'auteur a accordé une licence irrévocable et non exclusive permettant à la Bibliothèque nationale du Canada de reproduire, prêter, distribuer ou vendre des copies de sa thèse de quelque manière et sous quelque forme que ce soit pour mettre des exemplaires de cette thèse à la disposition des personnes intéressées.

L'auteur conserve la propriété du droit d'auteur qui protège sa thèse. Ni la thèse ni des extraits substantiels de celle-ci ne doivent être imprimés ou autrement reproduits sans son autorisation.

ISBN 0-315-71454-9

Canada

*A mi madre*

## ABSTRACT

Physical and biological processes are examined for the upper layer of the equatorial Pacific using data from a meridional transect along 150°W, and from a five day time series made at 0°. The data were acquired in spring of 1988. A free-fall vertical microstructure profiler, ELITESONDE, was used to estimate the rate of dissipation of turbulent kinetic energy. The goals of this study were to understand how the forcing due to air-sea fluxes and the fine-scale velocity and density structure influenced the meridional and temporal patterns of dissipation and to make a nitrate budget for the euphotic layer of the equatorial region. Hydrographic and meteorological data were typical for spring: the wind speed was low, the air temperature was higher than the water temperature and the equatorial undercurrent (EUC) was shallow and intense.

The meridional transect revealed a maximum in the rate of dissipation of turbulent kinetic energy,  $\epsilon$ . This peak was statistically significant to 95% confidence intervals between 1°S and 0° below 40 m, coinciding with the high vertical shear associated with the EUC.

The time series observations at 0° revealed a weak diurnal cycle in dissipation, confined to the upper 20 m and without deep night-time maxima as observed in Tropic Heat 1. The low wind speeds and shallow EUC core during the measurement period are consistent with the absence of deep mixing events at night. Dissipation was maximum during the day at 55 m, possibly associated with tidal forcing. The diurnal variability of the water column was governed by internal forcing rather than air-sea fluxes as was the case in Tropic Heat 1.

The zonal momentum budget was studied using the data from the five day time series. The wind stress at the surface was comparable to the climatological value of the integrated zonal pressure gradient between 0 and 60 m. The high dissipation values within the water column provided a large turbulent stress term at 55m. Consequently, the residual of the proposed momentum balance was only -19% of the zonal pressure gradient.

The nitrate budget is estimated for the equatorial region. Vertical advection into the meridional box was estimated from the observed meridional currents. The turbulent flux of nitrate was estimated from the dissipation measurements and the nitrate profile assuming gradient transport. The net supply due to advection (vertical supply minus meridional loss) is three times the turbulent flux. The total supply is compared with two concurrent measurements of biological consumption to provide an approximate budget. The supply was larger than the measured incorporation of nitrate into particles but comparable to the rate of nitrate disappearance from incubated samples. The discrepancy between new production estimates from physical supply or nitrate disappearance and from nitrate incorporation into particles suggests that dissolved organic nitrogen (DON) may play an important role in the equatorial region.

# List of symbols

$C_{ox}$	Cox number	
$C_D$	drag coefficient	
$C_p$	specific heat	
$C$	scalar	Chapter 4
$D$	molecular diffusivity	
$D$	mixed layer depth	Chapter 5
$E$	downwelling irradiance	
$E_{10}$	wind energy flux at 10 m	
$EL$	euphotic layer depth	Chapter 4
$E_{ml}$	integrated energy dissipation in the mixed layer	
$g$	gravitational acceleration	
$J_b$	buoyancy flux	
$J_{b+}$	buoyancy flux associated with surface heat losses	
$J_{b-}$	buoyancy flux associated with surface heat gain	
$J_{NO_3}$	vertical turbulent nitrate flux	
$J_q$	turbulent heat flux	
$K_m$	vertical eddy diffusivity for momentum	
$K_\rho$	vertical eddy diffusivity for mass	

$K_t$	vertical eddy diffusivity for heat	
$ml$	mixed layer depth	Chapter 3
$N$	buoyancy frequency	
$[\text{NO}_3]$	nitrate concentration	
$[\text{NO}_3]_N$	mean nitrate concentration at the northern edge of the meridional box	Chapter 4
$[\text{NO}_3]_S$	mean nitrate concentration at the southern edge of the meridional box	Chapter 4
$[\text{NO}_3]_B$	mean nitrate concentration at the bottom of the meridional box	Chapter 4
$[\text{NO}_2]$	nitrite concentration	
$P$	pressure	Chapter 3
$Q$	net surface heat flux	
$Q_+$	total surface heat losses	
$Ri$	gradient Richardson number	
$R_f$	flux Richardson number	
$R_{rho}$	density ratio for salt-fingers	
$S$	salinity	
$[\text{SiO}_3]$	silicate concentration	
$t$	time	
$T$	temperature	
$T'$	microscale temperature fluctuations	
$T^*$	non-dimensionalized temperature	Chapter 5
$T_N$	mean temperature at the northern edge of the meridional box	Chapter 4
$T_S$	mean temperature at the southern edge of the meridional box	Chapter 4
$T_B$	mean temperature at the bottom of the meridional box	Chapter 4

$u$	east-west velocity component	
$u'$	microscale fluctuations of the east-west velocity component	
$U$	velocity	
$U'$	meso-scale fluctuations of the east-west velocity component	Chapter 3
$v$	north-south velocity component	
$v'$	microscale fluctuations of the north-south velocity component	
$V'$	meso-scale fluctuations of the north-south velocity component	Chapter 3
$w$	vertical velocity component	
$W$	wind speed	
$z$	vertical coordinate	
$\alpha$	thermal expansion coefficient	
$\lambda$	rate of dissipation of thermal variance	
$c$	rate of dissipation of turbulent kinetic energy	
$\bar{\epsilon}_{ml}$	average rate of dissipation of turbulent kinetic energy in the mixed layer	
$c_{mod}$	modelled rate of dissipation of turbulent kinetic energy using similarity scaling	
$\Gamma$	mixing efficiency	
$\kappa$	von Karman's constant	
$\nu$	kinematic viscosity	
$\rho$	density	
$\rho_a$	air density	
$\tau$	wind stress	
$\tau^x$	east-west component of turbulent stress	
$\Delta\tau$	difference between the turbulent stress at the top and bottom of a layer	

# Acknowledgements

For this thesis I have changed fields from straight Biology and Ecology to an interdisciplinary approach to oceanography and it would not have been possible without the help and encouragement of the members of my committee. I shall always be grateful to Marlon Lewis for involving me in this project, for fearlessly encouraging me towards ever challenging topics and for his unflagging support. Neil Oakey has spent many, many hours patiently explaining and discussing concepts ranging from 'how-to' in the early stages of ELITESONDE construction to science and writing in more recent times. It has been a pleasure to work with both supervisors. Dan Kelley was always there to assist me in problems both large (on scales from galaxies to oceans) and small (say molecular ...) and both theoretical and practical. Dan unfailingly answers one's queries with additional questions, frustrating habit (!), but it pushes one onward on one's own propulsion. Thank you Dan! Barry Ruddick always had stimulating ideas and suggestions and extremely detailed assistance when least expected. Chris Garrett, when a committee member, was consistently challenging and inspiring. I have learned tremendously from all of you and am very grateful for all the comments and criticisms. Thank-you!

But many other people were also helpful. Scott Mclean built ELITESONDE and collected the data for this thesis together with Rob Palmer and Dave Hazen, and has given much support. The nutrient data of Burt Jones was used in the thesis. Owen Hertzmann gave practical assistance and mind-broadening conversations; Glen Lesins, Fred Dobson and Stu Smith generously provided formulae and programs various. Conversations with Dave Hebert have been very helpful in understanding the

equatorial region and his encouragement very appreciated. The presence of John Cullen this past year has been an unmitigated pleasure; he has forced me to recall my original training (and much more) and always urged me to look at things from a different direction.

All the people in the 2nd floor D-lab, past and present, have been extremely supportive. I thank my friends and family for the years of patience and love. And a special thanks to my father, who kept me going at the low points, greatly raising my spirits and the stock value of MT&T, and to Darek, who made life enjoyable.

# Contents

<b>Abstract</b>	<b>v</b>
<b>List of symbols</b>	<b>vi</b>
<b>Acknowledgements</b>	<b>ix</b>
<b>1 Introduction</b>	<b>1</b>
<b>2 Hydrographic patterns and vertical mixing</b>	<b>7</b>
2.1 Introduction . . . . .	7
2.2 Experimental details and data analysis . . . . .	8
2.2.1 Fine-scale measurements of scalars and velocity . . . . .	8
2.2.2 Microstructure measurements and analysis . . . . .	12
2.2.3 Meteorological measurements . . . . .	15
2.3 Meridional transect . . . . .	16
2.3.1 Meteorological conditions . . . . .	16
2.3.2 Hydrographic patterns . . . . .	17
2.3.3 Meridional transect of dissipation and vertical mixing . . . . .	27
2.4 Time series at the equator . . . . .	31
2.4.1 Meteorological conditions . . . . .	31
2.4.2 Hydrographic patterns . . . . .	31
2.4.3 Temporal variability of dissipation and vertical mixing . . . . .	40
2.5 Parameterization of mixing . . . . .	49

2.6	Summary . . . . .	54
<b>3</b>	<b>The spatial pattern of dissipation, its relationship to surface forcing and the role of turbulent fluxes in large scale budgets</b>	<b>56</b>
3.1	Introduction . . . . .	56
3.2	Experimental methods . . . . .	57
3.3	Vertical structure of dissipation along the meridional transect . . . . .	60
3.3.1	The equatorial maximum in turbulent dissipation . . . . .	60
3.3.2	The depth structure of dissipation: similarity scaling . . . . .	63
3.4	The role of turbulent fluxes in the large-scale balances of the equatorial Pacific . . . . .	76
3.4.1	Turbulent stress in the zonal momentum balance . . . . .	76
3.4.2	Diurnal variation of sea-surface temperature: the roles of turbulent mixing and penetrative irradiance . . . . .	85
3.5	Discussion . . . . .	90
3.5.1	Spatial and temporal variability in the equatorial region . . . . .	90
3.5.2	The role of turbulent mixing in the large-scale momentum balance . . . . .	95
3.6	Summary . . . . .	96
<b>4</b>	<b>A physical estimate of new production</b>	<b>98</b>
4.1	Introduction . . . . .	98
4.2	Material and methods . . . . .	99
4.2.1	Turbulent nitrate flux . . . . .	99
4.2.2	Simple advective box model . . . . .	100
4.2.3	Estimates of biological consumption of nitrate . . . . .	101
4.3	Results . . . . .	103
4.3.1	Turbulent nitrate supply and measured biological uptake rates . . . . .	103
4.3.2	Simple two-dimensional advective balance . . . . .	107
4.3.3	The nitrate budget for the equatorial region . . . . .	109

4.4	Discussion . . . . .	112
4.5	Summary . . . . .	119
<b>5</b>	<b>Influence of phytoplankton on the thermal structure of the upper ocean</b>	<b>121</b>
5.1	Introduction . . . . .	121
5.1.1	Diurnal heating of the oceans . . . . .	121
5.1.2	The role of light in the diurnal heating signal . . . . .	122
5.2	Some experimental evidence of the importance of variability in the chlorophyll concentration . . . . .	123
5.3	A simple model describing the role of chlorophyll in the heating rate of the upper ocean . . . . .	126
5.4	Conclusions . . . . .	132
<b>6</b>	<b>Conclusions</b>	<b>135</b>
	<b>Bibliography</b>	<b>139</b>

# List of Tables

3.1	Surface forcing in the meridional transect. Correlation matrix of the latitude averages of surface forcing terms and dissipation. . . . .	66
3.2	The average mixed layer dissipation and forcing terms for the day and night-time periods at 0° . . . . .	70
3.3	Forcing in the equatorial time series. Correlation matrix of the twelve-hour averages of forcing terms and dissipation at 0°. . . . .	71
3.4	The momentum budget for the top 60 m. . . . .	84
4.1	The two-dimensional advective nitrate balance of the equatorial region.	108
4.2	The nitrate budget of the equatorial Pacific. . . . .	111

# List of Figures

2.1	Sampling scheme. . . . .	9
2.2	Meteorological conditions along the meridional transect. . . . .	18
2.3	Contour plots of temperature and salinity along the meridional transect. . . . .	19
2.4	Contour plots of relative east-west velocity and relative north-south velocity . . . . .	21
2.5	Contour plots of nutrient concentrations along the meridional transect. . . . .	23
2.6	Contour plot of chlorophyll concentration in the meridional transect. . . . .	24
2.7	The $N^2$ , $U_z^2$ and $Ri$ along the meridional transect. . . . .	26
2.8	Turbulent kinetic energy dissipation, dissipation of thermal variance and vertical eddy diffusivity along the meridional transect. . . . .	29
2.9	Meteorological conditions at the equator. . . . .	32
2.10	Temperature in the upper layer at the equator. . . . .	33
2.11	Contour plots of temperature and salinity for the time series at the equator. . . . .	35
2.12	Contour plots of relative east-west velocity and north-south velocity for the time series at the equator. . . . .	36
2.13	Contour plots of nitrate concentration, nitrite concentration and chlorophyll concentration at the equator. . . . .	39
2.14	Canonical day in temperature at $0^\circ$ . . . . .	41
2.15	The time series of $N^2$ , $U_z^2$ and $Ri$ at the equator. . . . .	42
2.16	Time series of turbulent kinetic energy dissipation, and of dissipation of thermal variance at the equator. . . . .	44

2.17	Canonical day in turbulent dissipation at $0^\circ$ . . . . .	45
2.18	Time series of the vertical eddy diffusivity coefficients. . . . .	48
2.19	Time series of turbulent heat flux, $J_q$ , at the equator. . . . .	50
2.20	The eddy diffusivity coefficient as a function of the Richardson number. . . . .	53
3.1	Mixed layer depth. . . . .	58
3.2	Meridional pattern of turbulent dissipation assuming the null hypothesis that the equatorial population could have generated the observed pattern given the sampling errors. . . . .	62
3.3	Scatter plot of the total energy dissipated in the mixed layer <i>versus</i> the wind energy flux at 10 m for the meridional transect. . . . .	67
3.4	Dissipation modelled using similarity scaling and measured mixed layer dissipation. . . . .	68
3.5	Time series of wind energy flux at 10 m and the energy dissipated by turbulent mixing in the mixed layer. . . . .	72
3.6	Dissipation modelled using similarity scaling and measured mixed layer dissipation at $0^\circ$ . . . . .	74
3.7	The shear between 14 and 22 m and mixed layer dissipation. . . . .	75
3.8	Turbulent stress at the equator. . . . .	80
3.9	Contour plot of the time series of turbulent stress. . . . .	81
3.10	Turbulent stress divergence for the equatorial time series. . . . .	82
3.11	Time series of the terms of the one-dimensional heat flux . . . . .	87
3.12	Heat budget for the surface layer during the time series. . . . .	89
4.1	Cartoon of the two-dimensional advective box model. . . . .	102
4.2	The nitrate concentration gradient and vertical eddy diffusivity at the base of the euphotic layer. . . . .	105
4.3	The turbulent rate of nitrate supply and two measures of biological nitrate consumption. . . . .	106
4.4	Nitrate budget for the meridional boxes. . . . .	110

5.1	The parameter dependence of $K_2D$ . . . . .	129
5.2	The parameter dependence of $\Delta T^*/\Delta t$ . . . . .	131



# Chapter 1

## Introduction

The large-scale variations of velocity and of scalars, such as temperature, nutrient concentrations and biological productivity, are meridional in the equatorial Pacific. The zonal flow is driven by easterly winds: at the surface between  $0^\circ$  and  $8^\circ\text{S}$  (and to a depth of 300 m in its southern region) the South Equatorial Current (SEC) flows to the west. At  $0^\circ$ , below the SEC, the Equatorial Undercurrent (EUC) flows eastward. The EUC is a narrow, intense jet (with speeds of around  $1 \text{ m s}^{-1}$ ), confined to the equatorial waveguide between  $2^\circ\text{N}$  and  $2^\circ\text{S}$ . Between  $4^\circ$  and  $9^\circ\text{N}$ , the North Equatorial Counter Current (NECC) flows to the east in the top 150 m.

Associated with the intense zonal flow is a weaker meridional circulation which is poleward on the mean above the EUC (Ekman divergence) and equatorward below. An upwelling velocity, estimated to be  $1\text{--}3 \cdot 10^{-5} \text{ m s}^{-1}$  [Bryden and Brady, 1985, Brady and Bryden, 1987, Halpern and Freitag, 1987, Halpern *et al.*, 1989] is associated with the Ekman divergence above the EUC core. The upwelling of cold, nutrient-rich water which warms because of solar heating and becomes nutrient depleted due to biological uptake as it flows poleward explains the characteristic temperature minimum and nutrient and chlorophyll maximum found at the equator [Liu and Gautier, 1990, Feldman, 1986].

The primary production that is fueled by nutrients that are 'newly' introduced into the upper layer (as opposed to that running on regenerated nutrients from within the layer), or *new production*, is equivalent over long time scales to the export flux of organic matter from that layer [Dugdale and Goering, 1967, Eppley and Peterson, 1979]. This sinking organic matter can become isolated from the upper layer and thus may signify a sink for atmospheric carbon. The potentially large role of the equatorial Pacific in global new production was discussed by Chavez and Barber [1987]. They estimated an upper bound for new production by calculating the advective supply of nitrate to the euphotic zone due to upwelling. This estimate ignores the lateral loss of nitrate due to meridional flow. The new production value thus obtained was 50-60% of the total measured primary production. Since the area considered is very large, equatorial new production would make up a significant proportion (18-56%) of global new production. In this study a more appropriate estimate of the advective supply is made and the turbulent supply is estimated as well.

However, recent measurements of new production in the eastern equatorial Pacific, including observations of particle flux into sediment traps [Murray *et al.*, 1989], residence times of dissolved  $^{234}\text{Th}$  [Coale and Bruland, 1987, Murray *et al.*, 1989] and uptake of  $^{15}\text{N}$ -labelled nitrate [Murray *et al.*, 1989, Dugdale *et al.*, 1991, Wilkerson and Dugdale, 1991], indicate that new production is only 10-20% of the total primary production, rather than the 50-60% suggested by Chavez and Barber [1987]. In Chapter 4, an estimate is made of the supply of nitrate to the upper layer due to advective transport and vertical mixing and compared with two measures of biological consumption. A reason is suggested for the low values of production and export of particles.

The long-term mean as described above is subject to variability on time scales ranging from the interannual, such as the El Niño-Southern Oscillation (ENSO) [Wyrtki, 1975a, Philander, 1989] to higher frequencies, *e.g.* the 4-day 'pulses' corresponding to the passage of equatorially trapped Kelvin waves [Wunsch and Gill, 1976,

Cherkeskin *et al.*, 1986]. On an intermediate time scale, the seasonal cycle of the equatorial region [Wyrtki, 1974, Wyrtki, 1975b, McPhaden and Taft, 1988, Wilson and Leetma, 1988] is characterized by small variations in surface temperature (compared with higher latitudes) and significant changes in the strength and position of the equatorial current system. The strongest westward winds are observed in autumn and are accompanied by maximum westward flow. In boreal spring, the SEC flows to the east [Wilson and Leetma, 1988, McPhaden and Hayes, 1990], as the EUC shoals and attains maximum intensity [McPhaden and Taft, 1988, Wilson and Leetma, 1988]. The observations addressed in this thesis were made in boreal spring.

The interaction between large- and small-scale physics is unique in the equatorial region. The EUC, although subject to the above variability, provides a steady large vertical shear. This mean shear makes the region above the EUC core an 'ocean-scale laboratory for shear-driven turbulence' [Peters and Gregg, 1988]. Although the waters in the equatorial region are stratified, the high shear values are sufficient to reduce the gradient Richardson number below critical values [Moum *et al.*, 1989]. This leads to the expectation that turbulent mixing is larger in the vicinity of the EUC [Crawford, 1982].

A desire for a better understanding of the complex atmosphere-ocean coupling (specifically ENSO) and of the interaction of small- and large-scale processes inspired the oceanographic community to establish in 1981 the research program entitled Tropic Heat [Eriksen, 1985]. One of the goals of Tropic Heat was to parameterize turbulent mixing in terms of quantities which are measured routinely by ship or mooring and which are easily resolvable in models.

Intensive measurements of microscale (order centimeter) shear and temperature variance were made to obtain turbulent dissipation rates during Tropic Heat 1 in November 1984, and Tropic Heat 2 in April 1987. These studies enabled close examination of vertical mixing in the equatorial region. A composite data set prior to Tropic Heat [Crawford, 1982] revealed a strong maximum in energy dissipation,

$\epsilon$ , within 100 km of the equator. Later studies have not always found a dissipation maximum so narrowly confined to the equator. Intensive sampling in the Tropic Heat program revealed that at the equator itself, temporal variability associated with the diurnal cycle [Gregg *et al.*, 1985] was very large (a hundred-fold) and that there was a strong relationship between turbulent mixing in the upper layer and local winds [Moum *et al.*, 1986, Moum *et al.*, 1989]. Moum *et al.* [1989] reported that for a transect from 3°N to 3°S there was no spatial variation in  $\epsilon$  associated with either the equator or the EUC. Recent studies [Peters *et al.*, 1989, Hebert *et al.*, 1991a] that distinguish between the dissipation in the thermocline and in the mixed layer have found that dissipation in the thermocline peaked within a degree of the equator.

One aspect of the unique interaction between small and large-scale physical processes in the equatorial region is that the turbulent mixing of heat and momentum have been put forward as playing a significant role in the basin-wide dynamics. Niler and Stevenson [1982] found that for the annual mean heat budget of the tropical Pacific warm water pools, the net surface heating is balanced by the turbulent flux of heat into the thermocline. During the Tropic Heat 1 experiment, the turbulent heat flux at the base of the mixed layer was comparable to the net surface heat flux into the ocean [Gregg *et al.*, 1985, Peters *et al.*, 1988, Moum *et al.*, 1989]. Cold or warm sea-surface temperature anomalies in the equatorial Pacific, which result from variability in the mean flow and its fluctuations, modify the air-sea exchange of heat and moisture, and have been linked to displaced atmospheric circulation patterns over the American continent [Bjerknes, 1969, Wyrski, 1975a, Horel and Wallace, 1981, Eriksen, 1985, Trenberth *et al.*, 1988].

Crawford and Osborn [1982] proposed that vertical friction was the dominant energy sink for the EUC system. The actual role of the turbulent stress divergence in the zonal momentum balance does not appear to be as simple as assumed by the large-scale balances carried out by Bryden and Brady [1985, 1989] and internal waves may be an important mechanism for the downward transport of momentum [Dillon *et al.*, 1989, Hebert *et al.*, 1991b].

This thesis concentrates on the data collected in an equatorial transect along 150°W, and a short time series at 0°. The main goal of the cruise was to quantify the role of the equatorial region in global biogeochemical processes. The objective of this thesis is to discuss the physical forcing during this period, focussing mainly on the temporal and spatial variability of the small-scale mixing in the surface layer and its role in the large scale and long term balances of the region. These physical processes (advection, surface fluxes and vertical mixing) are then addressed in the context of nutrient supply to the upper layer, thus providing an estimate of the potential importance of the region in the global CO<sub>2</sub> cycle.

The questions that are addressed in this thesis are:

- What were the large scale patterns of surface forcing (heat fluxes, wind and buoyancy flux), temperature, salinity, nutrients and velocity along the meridional transect and for the equatorial time series?
- What was the meridional pattern of dissipation; was there a maximum associated with the EUC?
- What dominated the temporal variability of the equatorial time series? Did the dissipation in the upper layer respond directly to surface forcing?
- What role does turbulent stress play in the large scale zonal momentum balance at 0°?
- What controlled the heat budget of the upper layer at 0°?
- What is the nitrate budget of the equatorial region? Is the physical supply of nitrate dominated by advection or turbulent mixing? Does the supply balance the uptake of nitrate by the organisms?
- How can we quantify the potential importance of the optical properties of the water column in the heating rate of the upper layer?

In Chapter 2, the mean large-scale hydrographic patterns are presented and the small-scale mixing parameters observed along the meridional transect and during the equatorial time series are introduced. In Chapter 3, the vertical mixing is analysed in more detail: further statistical testing of the meridional structure of turbulent energy dissipation is carried out and the observed mixed layer dissipation is modelled in terms of the surface forcing terms. The turbulence measurements made during the equatorial time series are used to assess the role of vertical friction in the annual zonal momentum balance and a simple one-dimensional heat budget is done for the upper layer. New production is estimated as the rate of physical supply of nitrate to the upper layer and compared to concurrent measurements of biological nitrate consumption in Chapter 4. A short discussion on the role of penetrative irradiance in the diurnal heating rate of the upper ocean is made in Chapter 5. The general conclusions of the thesis are given in Chapter 6.

# Chapter 2

## Hydrographic patterns and vertical mixing

### 2.1 Introduction

The large- and fine-scale patterns (from hundreds of kilometers to meters) of scalars, velocity and vertical mixing parameters observed during the cruise are presented in this chapter. The objective is twofold: to set the stage for the rest of the thesis dealing specifically with the meridional transect (Chapters 3 and 4) and to interpret the patterns of vertical mixing in terms of the larger scale hydrography.

The large-scale conditions were typical for northern spring. The sampling period coincided with the end of the warming episode of the 1986-1987 El Niño and the start of a cooling event, which would culminate in May with sea surface temperature anomaly patterns that have been linked to the extensive drought conditions observed in summer of 1988 in North America [Janowiak, 1988, Trenberth *et al.*, 1988]. Cold sea-surface temperatures during our study period led to low values of surface heat losses to the atmosphere and were accompanied by high values of turbulent heat flux at depth.

A discussion of experimental details and data analysis techniques used is given in section 2.2. In section 2.3, the results of the meridional transect are presented:

meteorological conditions, hydrographic patterns and the small-scale physics. The equatorial time series is discussed in section 2.4, also by examining the meteorological conditions, large-scale hydrography and microstructure measurements. The parameterization of vertical mixing using the Richardson number is addressed in section 2.5, followed by conclusions in section 2.7.

## 2.2 Experimental details and data analysis

The R/V *Wecoma* surveyed from 15°N to 15°S along 150°W (cruise WEC88) in February-March 1988. The sampling scheme is summarized in Figure 2.1. Time is expressed in Figure 2.1 and in all subsequent discussion of the equatorial time series in **1988 year days**. The year day is defined as the day number of the annual period, where 1 January 1988 is year day 1. Because 1988 was a leap year, 1 March 1988 is year day 61.

### 2.2.1 Fine-scale measurements of scalars and velocity

CTD measurements were made (using a Neil Brown system) of finescale temperature and salinity of the top 400 m in hydrographic drops every 2°30' between 15° and 5° (S and N) and then at 2°, 1° and 0° every 6 hours when on site. *In situ* density,  $\rho(S, T, 0)$ , was obtained using the International Equation of State of Sea Water [Gill, 1982] Since we are working in the upper part of the water column (top 100 m) the correction for pressure was unnecessary.

The buoyancy frequency squared is given by

$$N^2 = -\frac{g}{\rho_0} \frac{\partial \rho}{\partial z} \quad (2.1)$$

where  $g$  is the acceleration due to gravity ( $g = 9.81 \text{ m s}^{-2}$ ) and  $\rho_0$  is the density at the surface;  $\partial \rho / \partial z$  was determined by doing a 13 m least-squares linear fit of density to depth. The error in  $N^2$  is estimated to be less than 10% for large values ( $N^2 \simeq 10^{-4} \text{ s}^{-2}$ ) while small values ( $N^2 \simeq 10^{-6} \text{ s}^{-2}$ ) are within a factor of two.

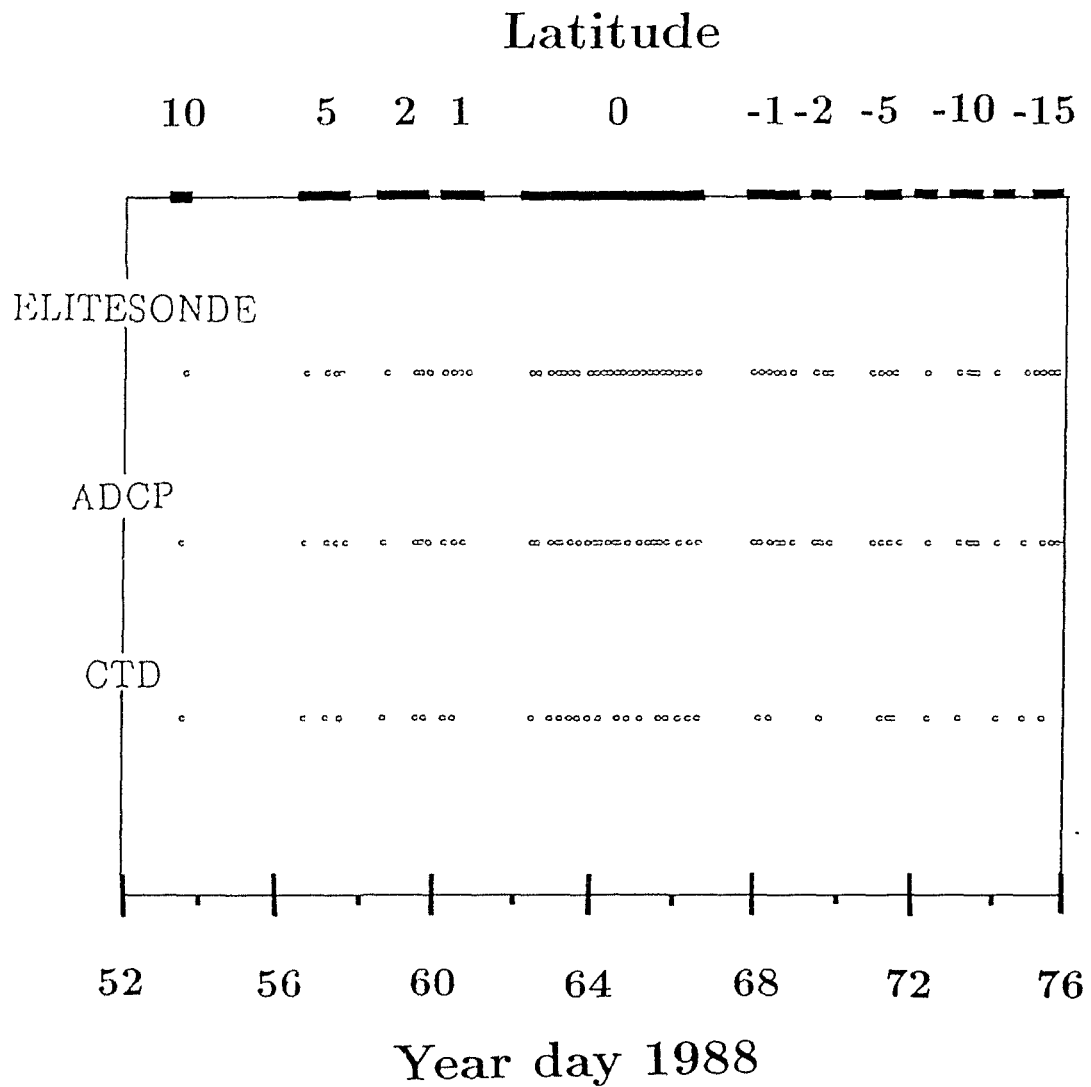


Figure 2.1: Sampling scheme. The horizontal axes are time (lower) and latitude (upper). The circles indicate stations from either hydrographic casts (CTD and nutrients), ELITESONDE or ADCP.

Currents were measured to a depth of approximately 150 m with an RDI Acoustic Doppler Current Profiler (ADCP). The Doppler-shifted frequency of the reflected signal was used to calculate the water motion relative to the ship in 8 m bins. Absolute velocities can be obtained using precise navigational records or an independent estimate of current to remove the ship motion. Lacking both of these, an arbitrary reference depth was chosen and subtracted from all depth bins. The chosen depth bin for the velocities shown in this chapter was centered at 14 m, based on the results of Bryden and Brady [1985] which indicate that for the long-term annual mean velocity at the equator, the cross-over between the westward flowing surface current and the eastward undercurrent occurs at around 15 m. This choice may be suitable for the zonal flow at the equator but probably was not the best choice for the rest of the transect. However, for the purposes of this chapter, a qualitative picture of general flow patterns is sufficient. The main use of the ADCP data here is to estimate shear, which is independent of the reference depth chosen. Two minute velocity measurements were averaged to provide hourly estimates that made up the basic data set. The error associated with the relative velocities is estimated to be less than  $0.05 \text{ m s}^{-1}$ .

Shear was calculated by first differencing the relative velocities (ADCP) measured below 20 m depth from adjacent 8 m bins and was then interpolated to 10 m depth intervals. The uncertainty associated with this method is twofold. Due to the averaging procedure inherent to the ADCP system, the velocities obtained for each depth bin are the result of triangular spatial filtering of the Doppler shifted signals. This low pass filter leads to an underestimation of shear. Shear values are underestimated at all scales but particularly so at scales close to the bin size [Toole *et al.*, 1987]. To assess the implications of this averaging, as in Toole *et al.* [1987], comparison was made between shear calculated over 8, 16 and 32 m depth intervals. The shear was the same within 15% for each case. The only difference was found at the equator: shear was 50% greater when calculated from the 8 m bin size in the 16 m region above the EUC core. This suggests that there was high wavenumber variability which was

averaged out on scales larger than around 20 m. In the case of Toole *et al.* [1987], where larger bin sizes yielded higher shear estimates, the low-wavenumber variability was not resolvable on the smaller scale. Because it is not possible to estimate shear at smaller intervals than the bin size, our measurement is less than or equal to the actual shear. This implies that Richardson number and  $K_m$  may be overestimated. The error associated with the shear values was estimated as in Toole *et al.* [1987] by calculating the variance of the hourly averages. It is found to be less than 10% of the measured shear for both components.

The Richardson number was estimated from the CTD and ADCP data using

$$Ri = \frac{N^2}{U_z^2} \quad (2.2)$$

$$\text{where} \quad U_z^2 = u_z^2 + v_z^2$$

and  $u$  and  $v$  are the north and east velocity components. The error in Richardson number is estimated from the uncertainty in  $N^2$  and  $U_z$  to be approximately 20% for large  $N^2$  and 100% for small  $N^2$ . In general, the largest shears (observed above the EUC) coincide with large values of  $N^2$ .

The concentrations of nitrate, nitrite and silicate were measured using standard automated techniques [Whitledge *et al.*, 1981] on water samples collected during the hydrographic casts using 5 l Niskin bottles on a rosette. The uncertainty of the nitrate and silicate determination is less than 5%. Chlorophyll concentrations, obtained by filtering water samples on Whatman GF/F filters and extracting in 90% acetone, were determined with a Turner Designs 10-005R fluorometer. Standard deviations of replicate determinations were less than 5% of the mean value.

Downwelling visible irradiance (300–700 nm) was measured within the water column with a QSP-200L sensor (BioSpherical Instruments). These light measurements were used to determine the depth of the euphotic zone (or illuminated layer) and to obtain an estimate of the diffuse attenuation coefficient for the equatorial time series.

### 2.2.2 Microstructure measurements and analysis

Microstructure measurements of temperature and shear were made with ELITESONDE, a 1.75 m free-falling vertical profiler, similar to EPSONDE [Oakey, 1988]. The instrument measures temperature microstructure with a glass-bead thermistor and two components of horizontal velocity shear using probes similar to those described by Osborn and Crawford [1980]. Two to ten profiles were taken approximately four minutes apart and averaged together for each station. There were one to twenty-four stations at each latitude: 10°N, 5°N, 2°N, 1°N, 0°, 1°S, 2°S, 5°S, 7.5°S, 10°S, 12.5°S and 15°S. The dissipation values of the stations at each latitude were also averaged to give the latitude mean. A time series of four and a half days, with stations every four hours was carried out at the equator.

Microstructure data analysis was similar to that of Oakey [1985]. The power spectra of shear variance (having corrected for sensor and instrument electronic response) were examined to determine the spectral minimum (separating signal and noise) which was used as the cutoff point for integration. A variety of editing criteria (including comparison to a theoretical universal curve) were used to reject data contaminated by spurious instrument noise. In the case of temperature variance, the frequency response of the glass-bead thermistor was unable to resolve the minimum between signal and noise at high dissipation rates. Temperature variance was determined to a fixed frequency (or wavenumber) and the 'lost' variance was estimated by comparing the variance obtained by integrating the theoretical Batchelor curve [Batchelor, 1959] to the fixed wavenumber with that obtained by integrating to the Batchelor cut-off wavenumber,  $k_B$  ( $k_B = (\epsilon/\nu D^2)^{1/4}$  (where  $D$  is the molecular diffusivity,  $D = 1.4 \cdot 10^{-7} \text{ m}^2 \text{ s}^{-1}$  and  $\nu$  is the kinematic viscosity,  $\nu = 1.3 \cdot 10^{-6} \text{ m}^2 \text{ s}^{-1}$ ). The variance resulting from integrating to  $k_B$  was taken to be 100%. The fraction of thermal variance that was resolved by our thermistor varied from 99% in regions of low dissipation, to 30% in the high shear zone at the equator (see Figure 2.16b).

The rate of dissipation of turbulent kinetic energy,  $\epsilon$ , is calculated for each segment

[Oakey, 1985] assuming isotropic turbulence with

$$\epsilon = \frac{15}{2} \nu \overline{\left(\frac{\partial u'}{\partial z}\right)^2} \quad [\text{W kg}^{-1}] \quad (2.3)$$

where the  $\partial u'/\partial z$  is the fluctuating horizontal shear, as opposed to the mean (Reynolds decomposition), and is measured with ELITESONDE at 256 Hz, meaning that the shear is measured every few millimeters at the observed fall rates.

The rate of dissipation of thermal variance,  $\chi$ , is given by [Oakey, 1985]

$$\chi = 6 D \overline{\left(\frac{\partial T'}{\partial z}\right)^2} \quad [^{\circ}\text{C}^2 \text{ s}^{-1}] \quad (2.4)$$

where  $\partial T'/\partial z$  is the microscale temperature gradient measured at 256 Hz as well.

The microstructure data of the first 10 m are discarded because of noise from wave action and the ship. Mean values for microscale shear and temperature variance are found for each 'segment', an 8 second interval (corresponding to approximately 6 m depth). The parameters  $\epsilon$  and  $\chi$  were estimated for each segment and then interpolated to produce values for 10 m depth intervals. For the equatorial time series, the 95% confidence intervals for the mean value at each station and depth intervals were calculated assuming a lognormal distribution and using the method outlined in Baker and Gibson [1987]. For the meridional transect, the 95% confidence limits of the latitude mean were calculated using a bootstrap method [Efron and Gong, 1983].

Three coefficients of vertical eddy diffusivity were estimated using microstructure and fine-scale measurements. The vertical eddy coefficient for heat,  $K_T$ , is estimated using the Osborn-Cox model [Osborn and Cox, 1972]:

$$K_T = 3 D Cox \quad [\text{m}^2 \text{ s}^{-1}] \quad (2.5)$$

$$\text{where} \quad Cox = \frac{\overline{(\partial T'/\partial z)^2}}{(\partial \bar{T}/\partial z)^2} + 1$$

where  $T'$  is the microscale temperature fluctuation and  $\bar{T}$  is the mean temperature measured at 16 Hz (or approximately every 5 cm) by ELITESONDE.

The flux of scalars in stratified fluids with well-defined gradients is often parameterized assuming gradient transport, analogously to molecular diffusion. Following this reasoning, the turbulent heat flux,  $J_q$ , was estimated using

$$J_q = -\rho C_p K_T \frac{\partial \bar{T}}{\partial z} \quad [\text{W m}^{-2}] \quad (2.6)$$

where  $C_p$  is the specific heat of water ( $C_p = 4.129 \cdot 10^3 \text{ J (kg } ^\circ\text{C)}^{-1}$ ) [Gill, 1982].  $K_T$  and  $J_q$  were estimated for each segment and then interpolated to provide 10 m averages.

The vertical eddy diffusivities for mass and momentum are estimated by merging the microstructure data from ELITESONDE and the fine-scale data from the CTD and ADCP respectively. The CTD cast used was the one closest in time to the microstructure station, usually within one hour. The temperature profiles measured by ELITESONDE and the CTD were always compared and on occasion, the two were different (the thermocline had changed its depth). In such cases, the T-S relationship for different segments of the water column was obtained from the CTD drop and salinity values were assigned to the temperature profile from ELITESONDE. This was then used to obtain density and  $N^2$  for that ELITESONDE station. This method was only necessary for thirteen of the sixty-one stations. The ADCP was operating almost continuously, and it was fairly easy to choose an hourly value close to the microstructure station. Usually, the ADCP data used was within two hours of the ELITESONDE drops.

The vertical eddy diffusivity for mass,  $K_\rho$ , is calculated using the Osborn model [Osborn, 1980] with the 10 m values of  $\epsilon$  (from ELITESONDE) and of  $N^2$  (from the CTD)

$$K_\rho = \frac{R_f}{1 - R_f} \frac{\epsilon}{N^2} \quad [\text{m}^2 \text{ s}^{-1}] \quad (2.7)$$

$$\text{where} \quad \frac{R_f}{1 - R_f} = \Gamma \quad (2.8)$$

where  $R_f$  is the flux Richardson number and  $\Gamma$  is called the mixing efficiency. Values for  $\Gamma$  have been proposed on theoretical grounds, based on a critical value for  $R_f$

[Osborn, 1980], as well as using actual measurements of shear and thermal variance, and assuming that the coefficients for heat and mass are the same [Oakey, 1985]. Both approaches lead to an approximate value of 0.25 for  $\Gamma$ .

The dissipation method [Gregg *et al.*, 1985] is used to obtain a value for the diffusivity for momentum,  $K_m$ , from the 10 m values of  $\epsilon$  and of shear squared (from the ADCP),

$$K_m = \frac{\epsilon}{U_z^2} \quad [\text{m}^2 \text{ s}^{-1}] \quad (2.9)$$

This method is only applicable where the major source of turbulent mixing is a steady mean shear and therefore is not appropriate for most of the open ocean, where turbulence is usually either surface-driven or the result of intermittent shear due to internal waves [Gregg, 1987]. Here it is used only at the equator, where the shear above the EUC was steady and large.

### 2.2.3 Meteorological measurements

Standard meteorological measurements were made of dry and wet bulb air temperature and sea-surface temperature. Wind speed and direction were measured with the ship anemometer at 20 m every 10 minutes. The 10-minute measurements were averaged to obtain hourly values. They were then corrected to 10 m with the logarithmic wind profile and the air-sea temperature difference using a program [B. Toulany and F. Dobson, pers. comm., 1991] based on the procedures outlined in Smith [1988]. Surface heat fluxes were calculated with standard bulk formulae [Gill, 1982] using wind speeds measured by the ship anemometers. Incoming irradiance was taken to be twice the value of the visible radiation measured on the ships deck by the visible irradiance sensor [Siegel and Dickey, 1987]. Humidity was estimated using wet and dry bulb temperatures. The surface buoyancy flux,  $J_b$  was estimated using:

$$J_b = J_{b+} + J_{b-} = \frac{g \alpha}{\rho C_p} (Q_+ + E) \quad [\text{W kg}^{-1}] \quad (2.10)$$

where  $Q_+$  is the sum of latent, sensible and long-wave flux (*i.e.* the convective case),  $E$  is the incoming short-wave flux, and  $\alpha$  is the thermal expansion coefficient

for seawater. Given the range of sea-surface temperatures observed, the  $\alpha$  used was  $3 \cdot 10^{-4} \text{ }^\circ\text{C}^{-1}$  [Gill, 1982]. To express the variability along the meridional transect only the positive buoyancy flux was estimated because the incoming solar irradiance was essentially the same at all latitudes. The total surface heat flux (losses plus the incoming short-wave flux during the day) was used to calculate  $J_b$  for the equatorial time series.

## 2.3 Meridional transect

It took 30 days to complete the  $30^\circ$  meridional transect, a period which is long compared to some of the most energetic phenomena controlling equatorial dynamics. ‘Slow’ variability at a given site, *e.g.* associated with the 20- and 4-day waves [Chereskin *et al.*, 1986] cannot be resolved adequately by a cruise spanning  $30^\circ$  of latitude. Another problem is the aliasing introduced by insufficient sampling of the diurnal cycle. Peters *et al.* [1989] found that for a transect from  $3^\circ\text{N}$  to  $3^\circ\text{S}$  the diurnal variability in turbulent dissipation was two decades while the spatial variability was a factor of three. In our  $30^\circ$  transect, there were latitudes for which only day stations were taken ( $10^\circ\text{N}$ ,  $7.5^\circ\text{S}$  and  $12.5^\circ\text{S}$ ) and others that had predominantly night stations:  $2^\circ\text{S}$  and  $15^\circ\text{S}$ . However, the remaining latitudes had 2 day and 2 night stations (the equatorial time series had 14 day and 10 night stations). Thus, we consider that the diurnal cycle has been adequately sampled at most latitudes and consequently the meridional structure will not be aliased by diurnal variability.

### 2.3.1 Meteorological conditions

The observed values of wind speed, surface heat loss (sum of latent, sensible and long-wave) and convective buoyancy flux were averaged at each latitude (Figure 2.2). The most conspicuous aspect of both sea surface (SST) and air temperature (Figure 2.2a) along the cruise track is the equatorial minimum, increasing to maxima at  $5^\circ\text{N}$  and  $10^\circ\text{S}$ . The average air temperature was consistently greater than the SST. The largest

wind speed (Figure 2.2b) was observed at 10°N and for the rest of the transect, wind speeds were less than 7 m s<sup>-1</sup>. The surface heat loss (Figure 2.2c), resulting from the sum of sensible, latent and long-wave fluxes, reflects the pattern of wind speed and of air-sea temperature difference. We observe the greatest heat loss at 10°N, where the water temperature is most similar to that of air and the wind speed is largest. The lowest values occur where the air temperature is much larger than the SST (0°, 2°N, 10°S). The pattern of  $J_{b+}$  (Figure 2.2d), estimated from the heat loss, is the same.

### 2.3.2 Hydrographic patterns

#### Temperature, salinity and relative velocity

The contour plot of temperature along the meridional transect (Figure 2.3a) is similar to the ridge-trough system described by Wyrтки and Kilonsky [1984] as well as the climatological average presented by Bryden and Brady [1985]. Two pools of warm water are separated by the cold water of the equatorial divergence; this trend is reflected in the air temperature as well (Figure 2.2a). The 25° to 11°C isotherms dome at around 10°N, deepen at 5°N to shoal again at the equator, an effect of the upwelling associated with the EUC. They deepen again beyond 2°S. The warmest water (>29°C) is found in the top 75 m south of 7.5°S. The salinity structure (Figure 2.3b) is markedly asymmetric around the equator, with fresher water to the north. A front, marked by the 35 psu isoline, intersects the surface at 0° and extends to about 330 m at 15°S. This clear polarity north-south/ high-low salinity is attributed to the excess precipitation over evaporation in the Intertropical Convergence Zone (5-10°N) [Bryden and Brady, 1985]. A subsurface salinity maximum (>36 psu) is found south of 5°S between 100 to 200 m depth. This high salinity water is presumably formed in the subtropical gyre where evaporation is very high.

The clearest feature of the eastward velocity relative to the 15 m bin (Figure 2.4a) is the EUC. Maximum relative velocity is found at the equator at a depth of 78 m. This is typical for spring [McPhaden and Taft, 1988, Wilson and Leetma, 1988]. The NECC, found north of 8°N and below 50 m, also flows to the east. South of 5°N, the

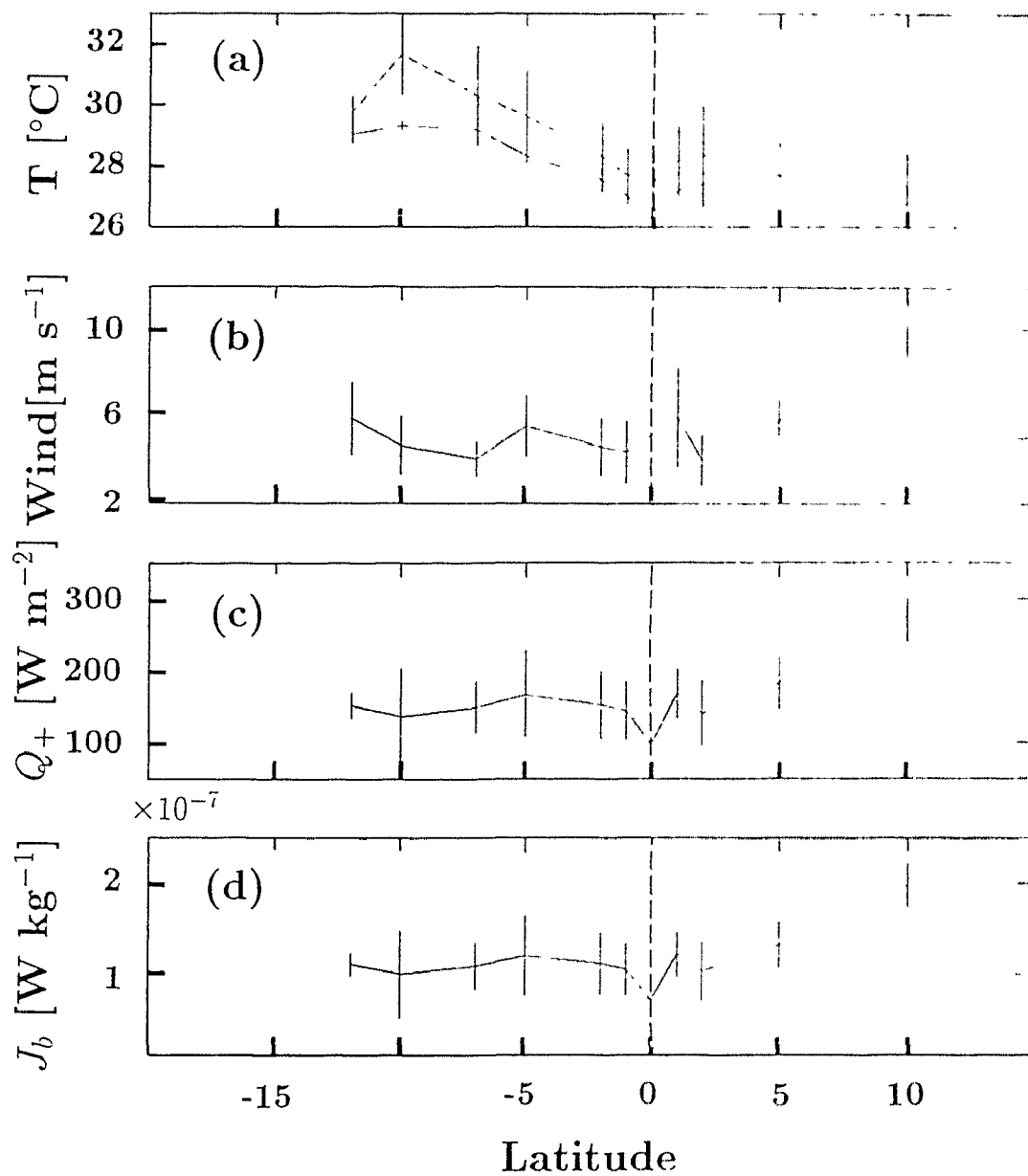


Figure 2.2: Meteorological conditions along the meridional transect. Air (dashed line) and sea surface temperature (solid line) (a); wind speed (b); surface heat loss, calculated as the sum of the sensible, latent and long wave flux terms (c); surface buoyancy flux (d). The error bars are the 95% confidence intervals of the latitude means.

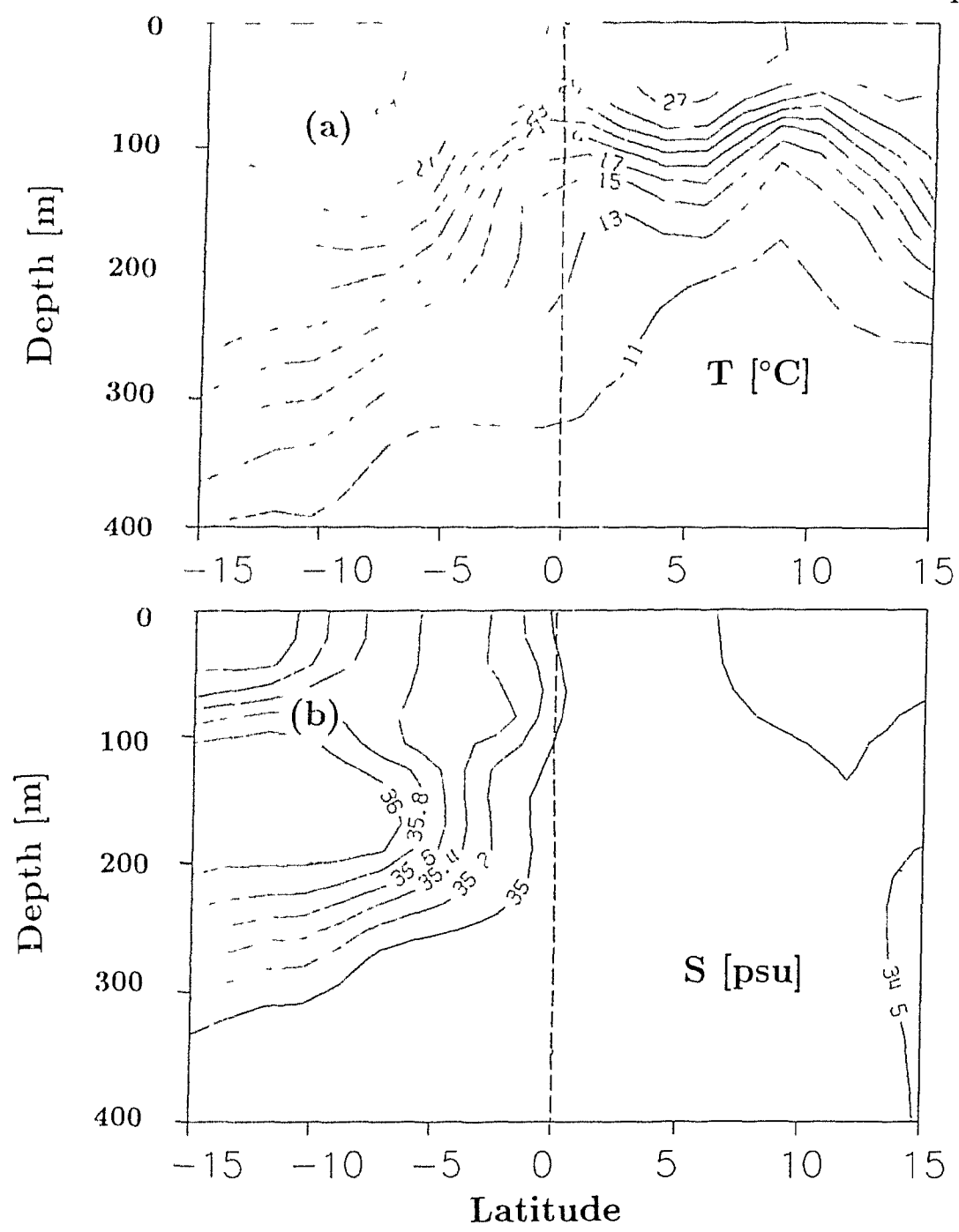


Figure 2.3: Contour plots of temperature (a) and salinity (b) along the meridional transect.

predominant flow is the westward SEC, which attains maximum values relative to 15 m at 50 m and deeper, between 8°S and 15°S. The high relative velocities associated with the EUC extend to 2°S and to 1°N (1 m s<sup>-1</sup> isoline).

The meridional velocity relative to 15 m (Figure 2.4b) is of small magnitude ( $O(0.1 \text{ m s}^{-1})$ ). Above the core of the EUC (20–75 m), the meridional flow diverges (Ekman divergence of the upwelled water) while at and below the core (75–150 m) there is a convergence (Figure 2.4c). The relative southward velocity is stronger than the relative northward velocity in both the divergence and the deeper convergence (Figure 2.4b). The divergence and convergence associated with this reference level are centered slightly to the north of the equator. This flow pattern is the result of assuming that the level of no motion was at 14 m. It is unlikely that the 14 m velocity be zero throughout the transect. The relative velocities are portrayed here for illustrative purposes.

The observed meridional velocities relative to the ship were very small and further analyses with a different level of no motion revealed a similar picture (see Chapter 4) which was comparable to the classical circulation pattern. A possible explanation for our observations is that, as will be seen later, we sampled the shift between southward and northward flow at 0°. This sign change during our sampling period may have allowed us to distinguish the meridional cell by averaging out the short-term variability.

## Nutrients and chlorophyll

The concentrations of nitrate, silicate and nitrite are shown in Figure 2.5, and the chlorophyll concentration in Figure 2.6. The meridional patterns of NO<sub>3</sub>, and SiO<sub>4</sub>, chemical substrates for photosynthetic production, follow that of temperature. There are low surface values, a region of high concentration gradient (nutricline) and high concentrations at depth. In the surface waters of the equatorial region, the concentrations are comparable to those of the upper thermocline. The highest concentrations observed are found below the shallow nutricline from 6°N to 15°N and the lowest are

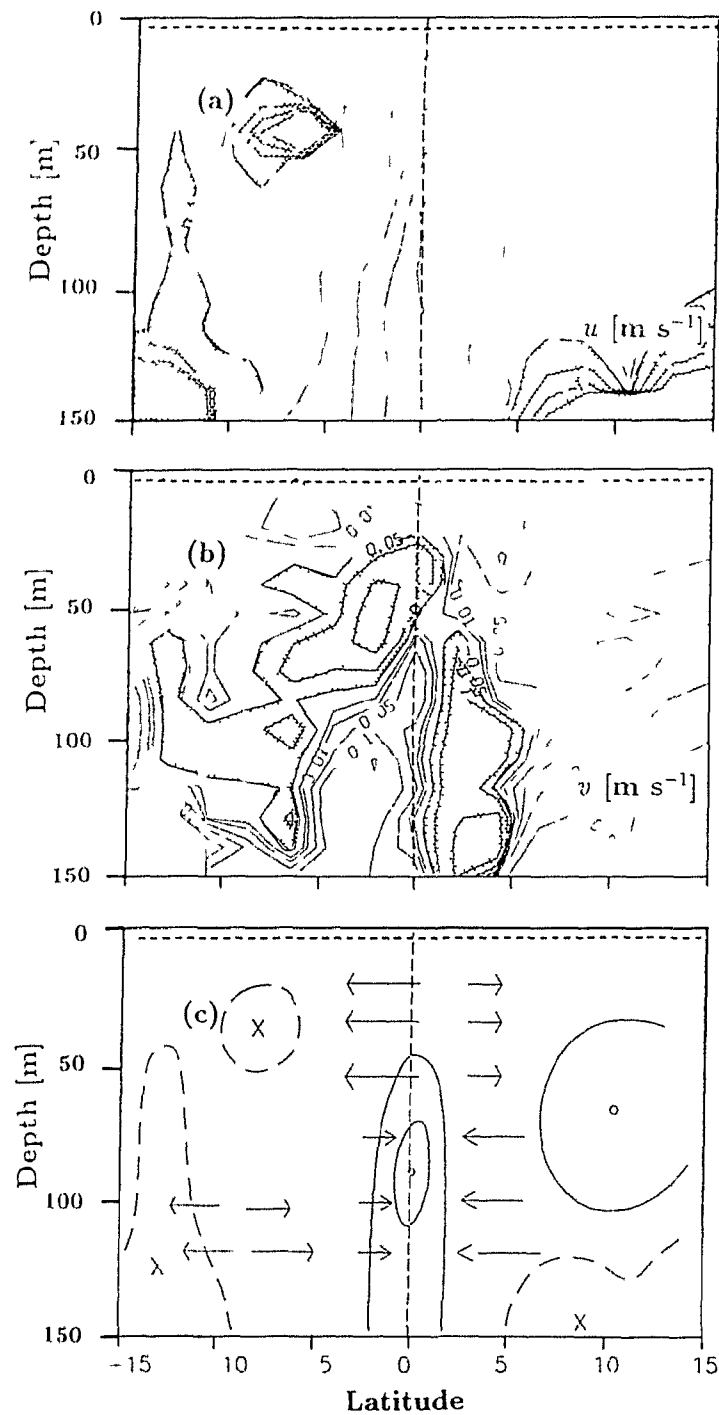


Figure 2 1: Contour plots of relative east-west velocity (a) and relative north-south velocity (b). The shaded areas are westward velocity in (a) and southward velocity in (b). Cartoon illustrating the flow pattern during the meridional transect (c), the contours represent east-west velocity (out of and into the page respectively) and the arrows meridional, flow. The dashed horizontal line is the reference level of no motion.

those of the mixed layer south of 5-10°S. In this region, the nutricline is found below the maximum temperature gradient. This results from the presence of low nutrient, high salinity water in the upper thermocline. Nitrite, indicative of subtropical water [Wyrski and Kilonsky, 1984] presents maxima up to 2  $\mu\text{mol l}^{-1}$  along the thermocline south of the equator. In the present transect, the nitrite values are less than 0.5  $\mu\text{mol l}^{-1}$  at and north of the equator. North of the equator, the silicate concentration in the upper 100 m generally exceeds the nitrate concentration. The situation is reversed between the equator and 7.5°S. Silicate is needed by diatoms to build their cell walls and the geographical distribution of relative nutrient concentrations may have consequences for the phytoplankton community type. In regions where the silicate concentration is less than nitrate, the balance is likely to shift more toward non-diatom species or toward diatoms with relatively low silicon requirements. Chavez [1989] observed that on the equator between 90° and 150°W, most of the chlorophyll was contained in the size fraction smaller than 1  $\mu\text{m}$  in diameter, *i.e.* the picoplankton. Likewise, Peña et al. [1990] found that cells smaller than 10  $\mu\text{m}$  made up 90% of the population at 135°W. This is consistent with the idea that large diatoms are much less important here than in coastal upwelling regions where nitrate concentrations are comparable. The chlorophyll concentration (Figure 2.6) presents the typical tropical structure with a deep chlorophyll maximum, ranging from 150 m at around 5°N to 60 m at the equator.

### Stability, shear and Richardson number

The meridional transects of stability,  $N^2$ , shear,  $U_z^2$ , and  $Ri$  are shown in Figure 2.7. There is a maximum in  $N^2$  from 0° to 1°N between 10 and 30 m. For the 35-55 m depth intervals, this peak becomes more pronounced and wider, extending latitudinally from 1°N to 1°S. The high values found close to 0° are related to the equatorial divergence where the mixed layer is shallow and the thermocline is close to the surface as a result of upwelling. The low  $N^2$  for the surface bin at 10°N may be related to the maximum in wind stress and buoyancy flux observed there (see

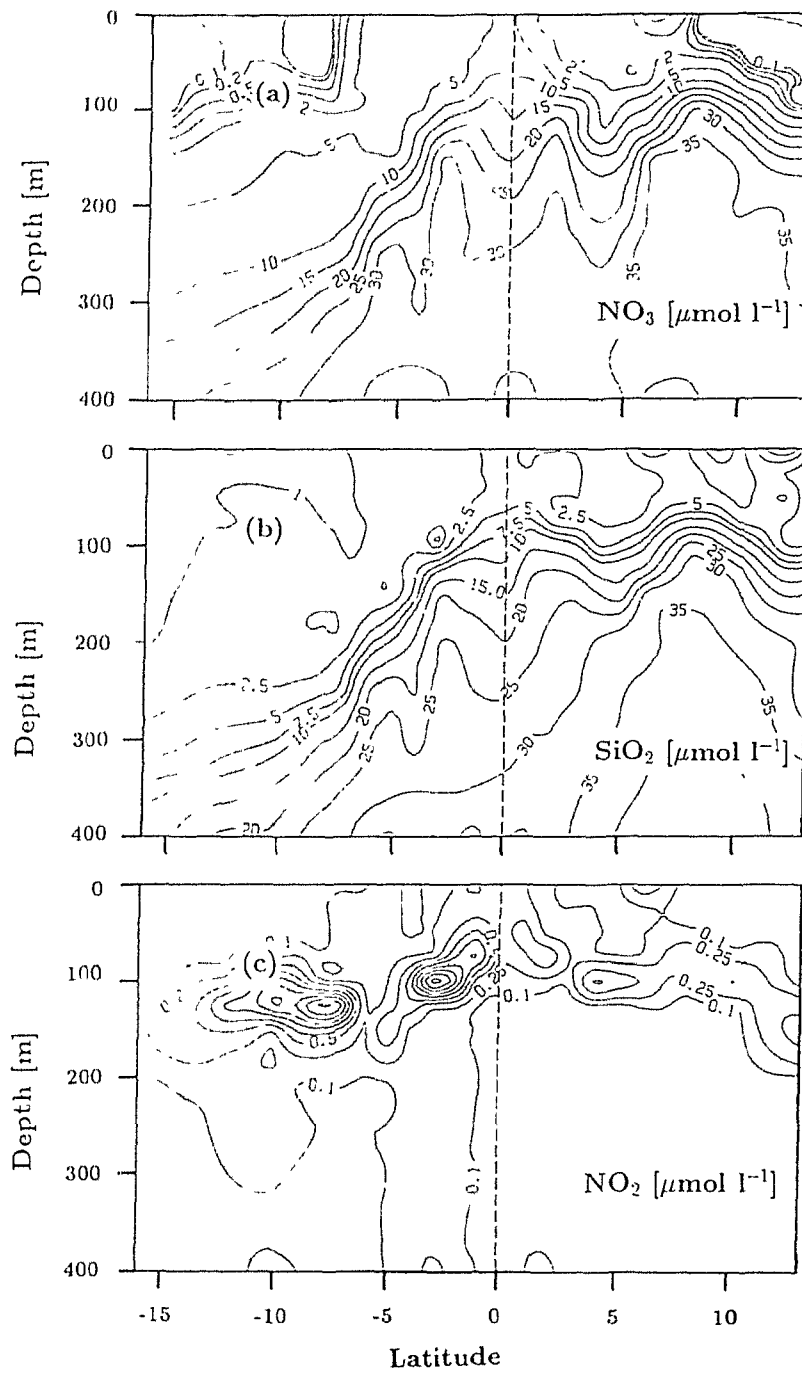


Figure 2.5: Contour plot of concentration of nitrate (a), silicate (b) and nitrite (c) in the meridional transect.

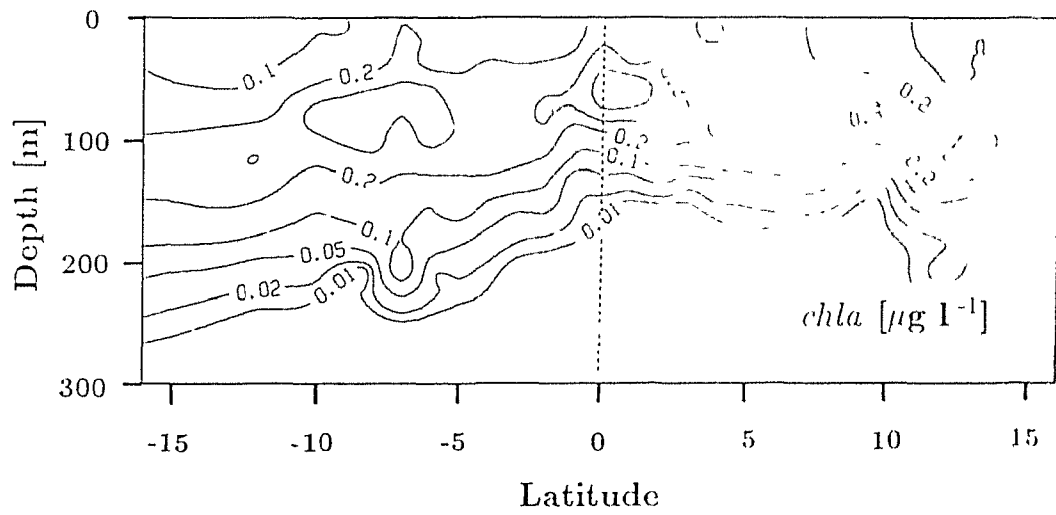


Figure 2.6: Contour plot of chlorophyll concentration in the meridional transect.

Figure 2.2). In Figure 2.7b the meridional, zonal and the total shear squared are shown. The value of total shear squared is below  $10^{-4} \text{ s}^{-2}$  except for the equatorial region from  $2^\circ\text{N}$  to  $2^\circ\text{S}$  between 20 and 50 m; the 55 and 65 m depth bins reveal high shear values at  $5^\circ\text{N}$  as well. The high equatorial  $U_z^2$  signal is a consequence of the EUC as is revealed in the zonal component. South of  $2\text{--}5^\circ\text{S}$  the meridional component of shear is predominant. Although the zonal component is largest around  $0^\circ$ , the meridional shear can be decisive in raising the total value.

The Richardson number ( $Ri$ ) was obtained by merging the  $N^2$  from the CTD and the shear data from the ADCP; the 10-m values of  $U_z^2$  and  $N^2$  provided the 10-m values of  $Ri$  for each station, and these are averaged to provide the latitude and depth interval means shown in Figure 2.7c. It is through  $Ri$  that we can try to provide a link between the fine-scale (CTD and ADCP) and the microstructure measurements (ELITESONDE). The  $Ri < 1/4$  threshold criterion for shear-flow instability [Miles, 1961] allows us to anticipate the regions where turbulent mixing is to be expected. The  $Ri$  number has also been used in to parameterize the mixing coefficient in models of equatorial dynamics [Pacanowski and Philander, 1981].

The Richardson number is less than  $1/4$  from  $1^\circ\text{S}$  to  $1^\circ\text{N}$  at 25 m; at 35 m between  $2^\circ\text{S}$  and  $1^\circ\text{N}$  and at 45 m from  $1^\circ\text{S}$  to  $0^\circ$ . Below 50 m there are no values below  $1/4$  although at the equator  $Ri$  is approximately  $1/4$ .  $Ri \leq 1/4$  are found from 10 to 50 m only between  $2^\circ\text{S}$  to  $1^\circ\text{N}$ . The equatorial minimum in  $Ri$ , in spite of large  $N^2$ , is a result of high shear at  $0^\circ$ . In addition to the EUC, spatial and temporal variability in the meridional shear component is also important [Toole *et al.*, 1987]. The southward displacement of the equatorial  $Ri$  minimum between 40 and 50 m is not due to the  $N^2$  values, as similar high values are found at  $1^\circ\text{N}$  and  $1^\circ\text{S}$ . Likewise at that depth the EUC is symmetrical around  $0^\circ$ . The meridional component of shear (see Figures 2.7b and 2.4b) is responsible for the low  $Ri$  to the south; this is similar to observations made by Toole *et al.* [1987] during an equatorial time series.

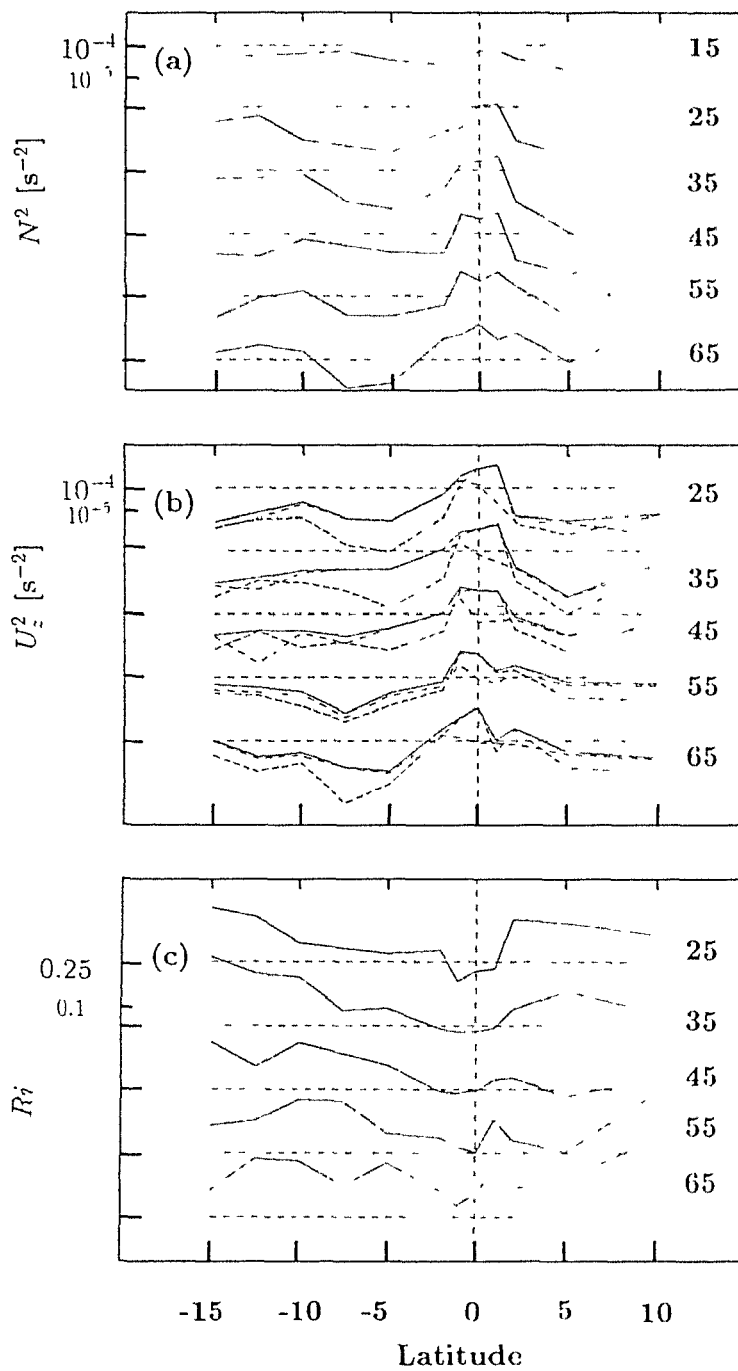


Figure 2.7: The  $N^2$  (a),  $U_z^2$  (b) and  $Ri$  (c) for each bin interval of the microstructure stations in the meridional transect. The solid line in (b) is the total shear,  $U_z^2$ , the dashed line is the zonal component,  $u_z^2$ , and the dotted line is the meridional component,  $v_z^2$ . The latitude average for each 10 m interval is labelled with the center depth: 15, 25, 35, 45, 55 and 65 m.

### 2.3.3 Meridional transect of dissipation and vertical mixing

The question addressed in this section is whether dissipation of turbulent kinetic energy peaks in the vicinity of the EUC. The existence of an equatorial maximum in dissipation has been proposed because of the low  $Ri$  characteristic of the high shear zone above the EUC core (see subsection 2.3.2, Figure 2.7c).

The usual space-time limitations of shipboard sampling are compounded in our data set by the considerable length of the transect ( $30^\circ$ ). On the other extreme of the temporal variability, we do not sample continuously with the microstructure profiler, but in discrete stations every four hours at best. We tried to sample throughout the diurnal cycle at most latitudes and there are day and night stations at  $1^\circ$ ,  $2^\circ$  and  $5^\circ$  (N and S) as well as at  $0^\circ$ . As in other studies [Peters *et al.*, 1988, Moum *et al.*, 1989, Peters *et al.*, 1989], a bootstrap procedure [Efron and Gong, 1983] was used to obtain an estimate of the uncertainty associated with the sampling.

Following Peters *et al.* [1989], a null hypothesis of constant dissipation along the meridional section is proposed. The latitude average for each depth interval is shown in Figure 2.8a. The latitude mean dissipation is maximum at all depths between  $1^\circ$ S and  $0^\circ$ .

To address the limitations of the sampling, the bootstrap procedure [Efron and Gong, 1983], in which the observed data set is subsampled repeatedly and randomly, was used to provide the confidence intervals for the latitude mean. The difference between the dissipation value at each station at a given latitude and the latitude average, or residual, was estimated for all stations along the transect. The F-test of homogeneity of variance showed that the variance of the residuals for the subset of off-equatorial stations and that of equatorial stations was the same within 95%. It is thus assumed that the intermittency was the same along the transect and the residuals for all stations were pooled together to form the transect ensemble. This ensemble of residuals was then subsampled with replacement  $n$  times (where  $n$  is the number of stations at each latitude); the  $n$  values are averaged and the process is iterated 500 times to provide a ‘bootstrap’ population for each depth interval and at each

latitude. This population is ordered and the 95% confidence limits of the latitude (and depth interval) mean are found by adding the top and bottom 2.5 percentile values of the residuals to that mean.

The meridional pattern of turbulent kinetic energy dissipation,  $\epsilon$ , is seen in Figure 2.8a. Each line is the mean value observed at each latitude for the specified 10 m intervals centered at 15 m, 25 m, 35 m, 45 m, 55 m and 65 m. The dotted lines are the 95% confidence limits. At three latitudes (10°N, 7.5°S and 12.5°S) there was only one station (2–6 vertical profiles). At these latitudes, the confidence intervals are the same order of magnitude as the range of the residuals of the entire transect at that depth: from two to three decades. The highest individual station values of  $\epsilon$  observed are greater than  $10^{-6} \text{ W kg}^{-1}$  at the equator (see Figure 2.16a). The lowest values were observed south of 5°S.

The observed meridional pattern is similar at all depths: a maximum in the equatorial region (0°–1°S) and minima at 2°N and 5°S. Poleward of the minima it either levels off or increases. Except for 10°N at 15 m, the mean is always less than  $10^{-8} \text{ W kg}^{-1}$  outside of the equatorial region. The southward bias of the equatorial maximum below 40 m is a consequence of the bias observed in  $Ri$  (Figure 2.7c). This results from the larger shear south of the equator in the meridional divergence between 30–55 m (Figure 2.4b and Figure 2.7b). The large surface values of  $\epsilon$  at 10°N correspond to the largest observed values of buoyancy flux and wind stress (Figures 2.3b, 2.3c).

The equatorial maximum in dissipation (between 0° and 1°S) is significant to 95% between 40 and 70 m depth. The null hypothesis of constant dissipation along the transect is rejected. The dissipation values north of 1°N are significantly distinct with respect to the equatorial region at all depths. The fact that the equatorial maximum is located at depth is consistent with the results of Peters *et al.* [1989] and Hebert *et al.* [1991a] of maxima in equatorial dissipation in the thermocline. A detailed analysis of the meridional pattern, testing the biases of sampling frequency and of the diurnal cycle, is done in the next chapter.

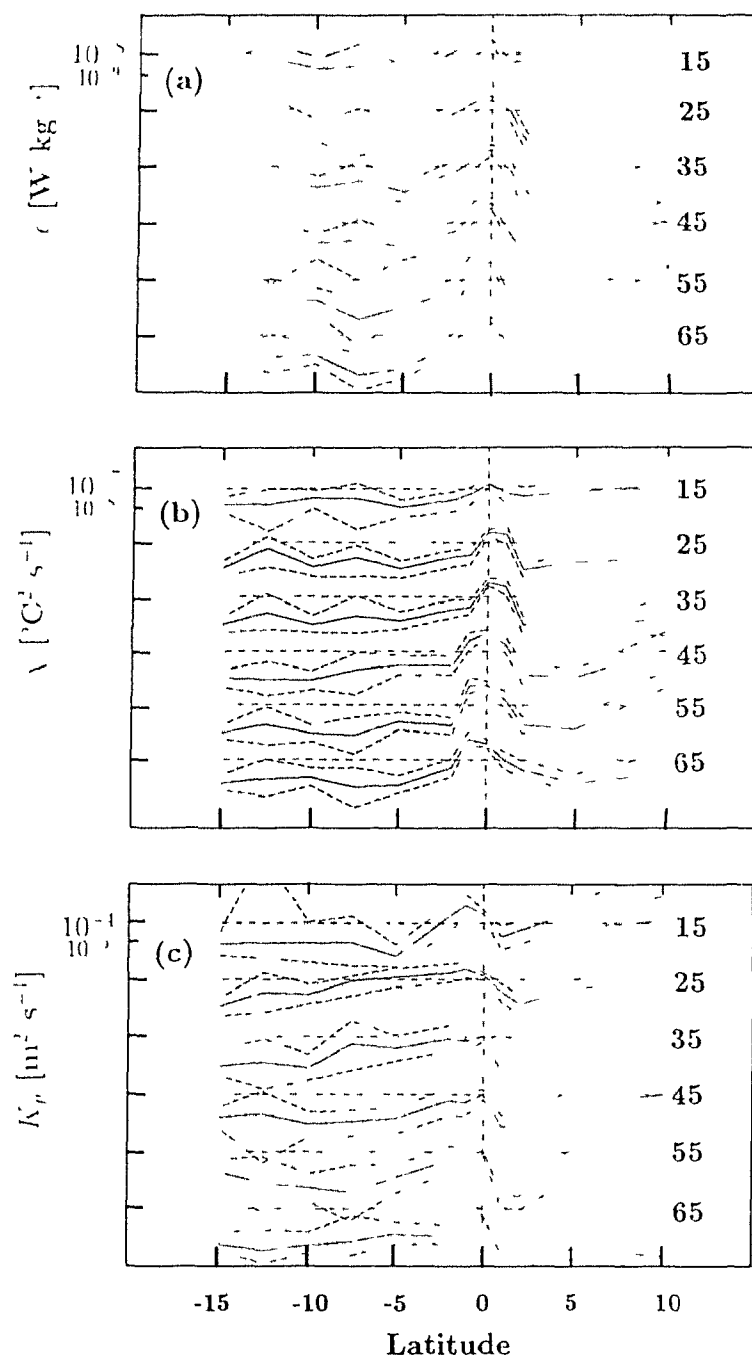


Figure 2.8: Turbulent kinetic energy dissipation,  $\epsilon$  (a), dissipation of thermal variance,  $\chi$  (b) and the vertical eddy diffusivity,  $K_{\rho}$  (c) along the meridional transect. The solid line is the mean for each depth interval at that latitude and the dashed lines are the 95% confidence intervals from a bootstrap method.

The rate of dissipation of thermal variance,  $\chi$ , is presented in Figure 2.8b. The equatorial maximum seems to be somewhat more confined latitudinally. The highest individual station values are observed at the equator (see Figure 2.16b) from 30–50 m (almost  $10^{-4} \text{ }^\circ\text{C}^2 \text{ s}^{-1}$ ). Latitude averages of order  $10^{-7} \text{ }^\circ\text{C}^2 \text{ s}^{-1}$  are only reached in the equatorial region, and at the surface at  $10^\circ\text{N}$ . The general pattern is similar to that observed for dissipation. The bootstrap procedure was applied as described above to determine the 95% confidence intervals. The equatorial maximum is statistically significant between  $0^\circ$  to  $1^\circ\text{N}$  at the 25 and 35 m depths; between  $1^\circ\text{N}$  and  $1^\circ\text{S}$  at 45 m and between  $0^\circ$  and  $1^\circ\text{S}$  for 50–60 m, reflecting, as in  $\epsilon$ , the larger meridional shear south of the equator (Figures 2.7b and 2.4b). The low values for  $1^\circ\text{N}$  below 50 m, as in dissipation, correspond to the peak in  $Ri$  (see Figure 2.7c).

The eddy diffusivity for mass,  $K_\rho$ , calculated using Eq. (2.7), is plotted in Figure 2.8c. This parameterization assumes that a constant fraction of the energy available for mixing is converted into buoyancy flux. The value used here for  $\Gamma$  is 0.25. In well-mixed layers, such as found around  $5^\circ\text{N}$  and between  $5^\circ\text{S}$  and  $10^\circ\text{S}$ , high dissipation does not imply a corresponding amount of buoyancy flux. If the density gradient is very weak, the upward transport of water only effects a small change in the potential energy of the water column. Consequently, for low  $N^2$ ,  $K_\rho$  overestimates the true mixing rate. Likewise, the determination of  $N^2$  is difficult in such cases. The meridional transect shows a maximum in  $K_\rho$  in the equatorial region for all depth bins although there are high values found at other latitudes as well (*e.g.*  $10^\circ\text{N}$ ). Large values of  $N^2$  are found at  $0^\circ$  (Figure 2.7a), which explains the displacement of the maximum in diffusivity to  $1^\circ\text{S}$  at 15 and 25 m.

The confidence intervals for the latitude mean of  $K_\rho$ , obtained using the bootstrap method, indicate that the equatorial maximum is statistically distinct from the values found to the south only at 15 and 65 m. The near-equatorial region to the north ( $1^\circ\text{N}$ – $2^\circ\text{N}$ ) presents a significant minimum with respect to the equatorial high at all depths, and corresponds to high  $N^2$  (Figure 2.7a) and low  $\epsilon$  values (Figure 2.8). The highest values observed are those of the top 30 m, where mean values greater than  $10^{-4} \text{ m}^2$

$s^{-1}$  are found.

## 2.4 Time series at the equator

### 2.4.1 Meteorological conditions

Time series measurements were made at the equator for 2–7 March 1988. The meteorological conditions are shown in Figure 2.9. During the study period, air temperatures (mean of  $27.4^{\circ}\text{C}$ ) were high, and the SST (mean of  $26.2^{\circ}\text{C}$ ) were lower than usual for March. Since the air is warmer than the water throughout the entire period, even at night, the latent heat losses are low and the sensible heat flux is into the ocean. An interesting feature is the drop in SST at year day 64 (see also Figure 2.10). This is the surface signature of large changes in the oceanographic conditions. The drop in SST is accompanied by slightly decreased air temperatures during the day. The average wind speed during the time series was low,  $5\text{ m s}^{-1}$ , in agreement with the seasonal average at  $140^{\circ}\text{W}$  [McPhaden and Hayes, 1990]. The proximity to the spring equinox explains the large incoming irradiance value (with maxima at noon of  $1000\text{ W m}^{-2}$ ). The surface heat losses are never greater than  $150\text{ W m}^{-2}$  and they decrease gradually during the study period to  $100\text{ W m}^{-2}$  as the SST decreases. The buoyancy flux is strongly negative during the day (heat going into the ocean) and positive at night with maximum values of  $10^{-7}\text{ W kg}^{-1}$ . The observed nocturnal heat loss and buoyancy flux are markedly less than the Tropic Heat 1 values ( $150\text{--}200\text{ W m}^{-2}$  and  $2 \cdot 10^{-7}\text{ W kg}^{-1}$  [Moum *et al.*, 1989]).

### 2.4.2 Hydrographic patterns

#### Temperature, nutrients and relative velocity

The temperature evolution of the equatorial surface layer is shown in Figure 2.10. The temperature at 3 m cools approximately  $0.6^{\circ}\text{C}$  between year date 63 and 65. Progressive thermal stratification of the top 20 m after day 64 is also quite clear. The

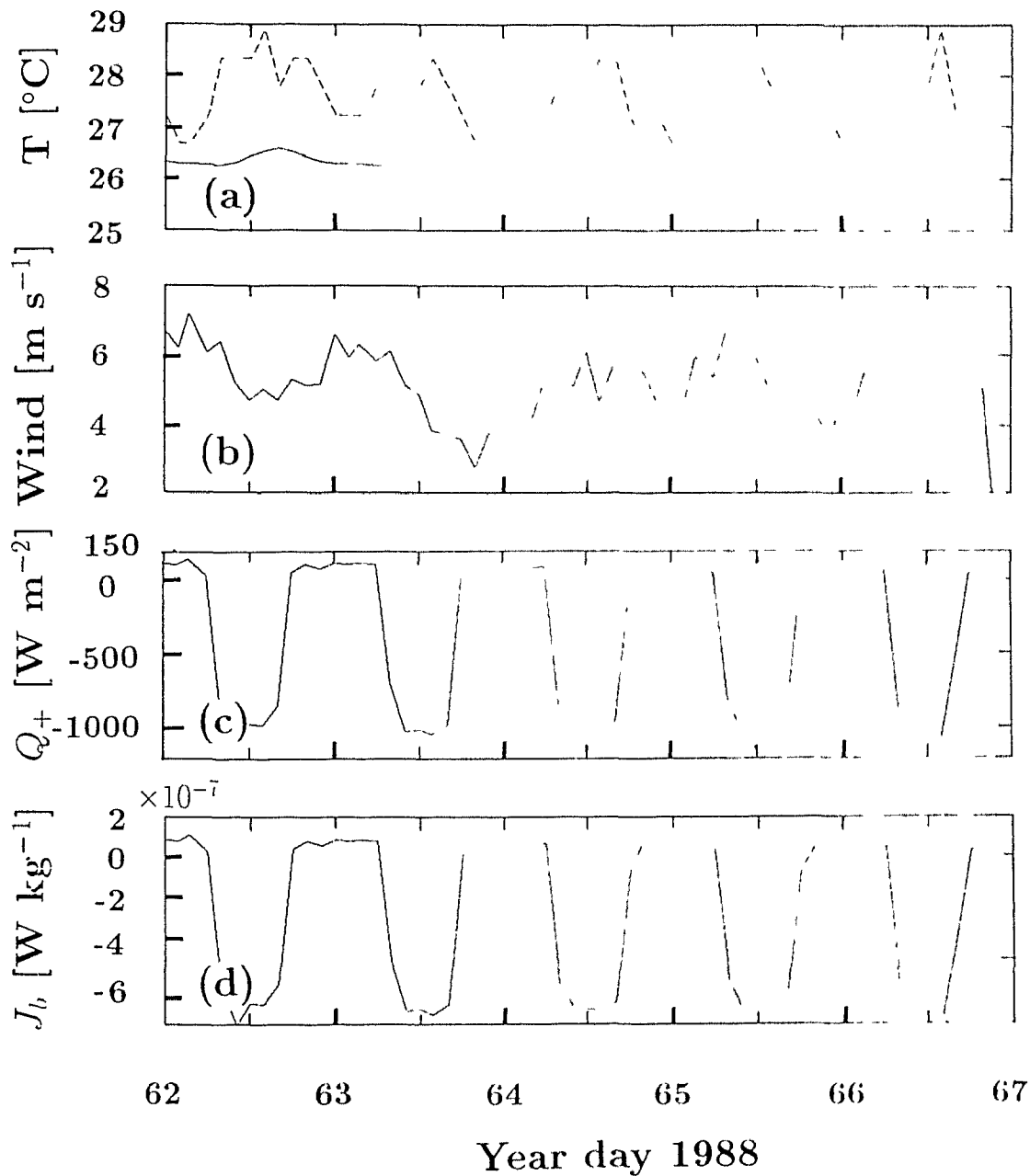


Figure 2.9: Meteorological conditions at the equator: Air (dashed line) and sea surface temperature (solid line) (a); wind speed (b); total surface heat flux, calculated as the sum of short-wave, sensible, latent and long-wave fluxes (c) (a negative flux is heat into the ocean); buoyancy flux (d).

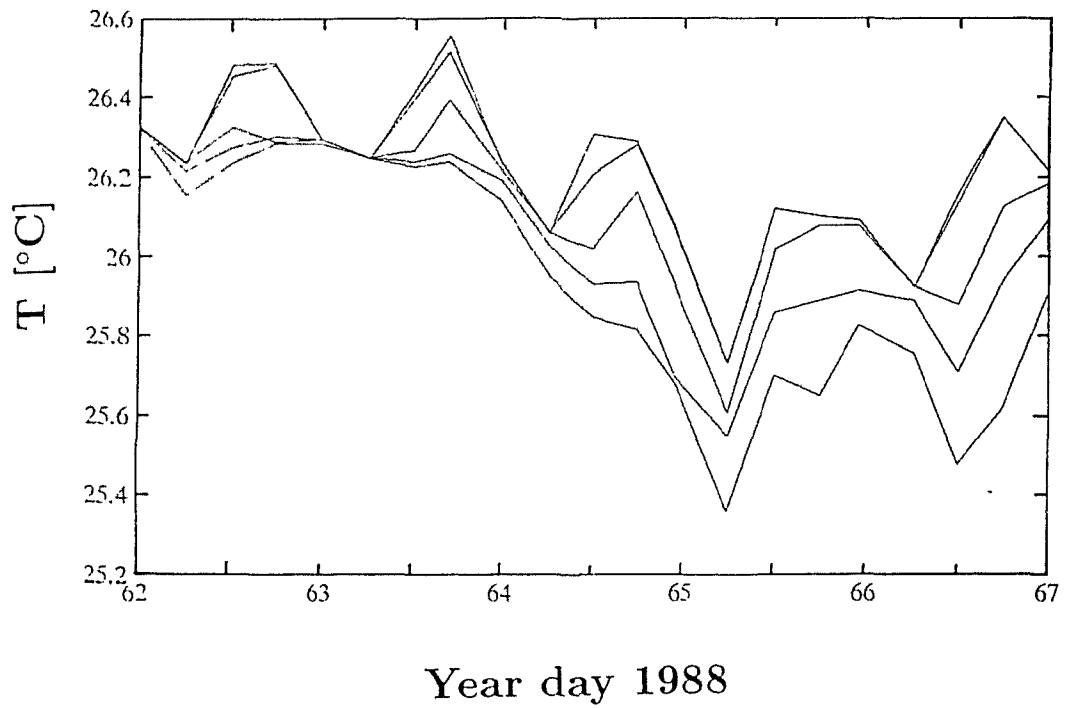


Figure 2.10: Temperature in the upper layer at the equator. The lines mark the time evolution at 3, 5, 10, 15 and 20 m depth.

diurnal signal between 5 and 10 m goes from approximate values of  $0.3^{\circ}\text{C}$  on day 63 to  $0.45^{\circ}\text{C}$  on day 64. This stratification persists throughout the night. Interestingly, as the temperature drops, the water column is stratifying. If the cooling were the result of surface forcing, it would be accompanied by convection (diminished stratification). The temperature contour plot (Figure 2.11a) also shows the cooling trend after day 64, as surface temperatures cool to values previously found around 35 m ( $26^{\circ}\text{C}$  isoline). Below 50 m, there is no apparent cooling parallel to that observed at the surface except after day 65 at and below 100 m. The separation of the  $16^{\circ}\text{C}$  and  $18^{\circ}\text{C}$  isotherms (at around 100 m) coincides with intensification of the EUC on day 67 (Figure 2.12a). The salinity (Figure 2.11b) of the upper 50 m increases from less than 35.1 on day 64 to 35.25 psu late in day 66. Vertically, there is a salinity maximum centered at 60 m at the start of the time series, which is gradually smoothed and by day 66, the salinity of the top 70 m is uniform and of the same value found originally at the maximum.

The contour plots of relative east-west velocity (Figure 2.12a) show intensification of the EUC starting on day 63, reaching a maximum during day 64 and another in the morning of day 67. The meridional velocity (Figure 2.12b) below 40 m changes from weak southward to northward flow early in year day 64 coinciding with the increase in salinity in the same depth range.

Nutrient and chlorophyll concentrations (Figures 2.13a and 2.13c) increase together (with no lag) at the surface after day 64, implying that the surface chlorophyll increase does not reflect growth in response to the enhanced nutrients, but that chlorophyll is acting as a passive tracer of the water motion. Nitrate goes from 4–5 to  $6\ \mu\text{mol l}^{-1}$ ; chlorophyll increases from  $< 0.3\ \mu\text{g l}^{-1}$  to  $> 0.3\ \mu\text{g l}^{-1}$ . Nitrite (Figure 2.13b) increases from values ranging from  $0.2\text{--}0.3\ \mu\text{mol l}^{-1}$  to  $0.3\text{--}0.45\ \mu\text{mol l}^{-1}$  after day 64 in the upper 60 m.

### **Temporal variability**

The observed changes in the upper water column after year day 64 (increased salinity and nutrient concentrations and decreased temperature) may result from the changes

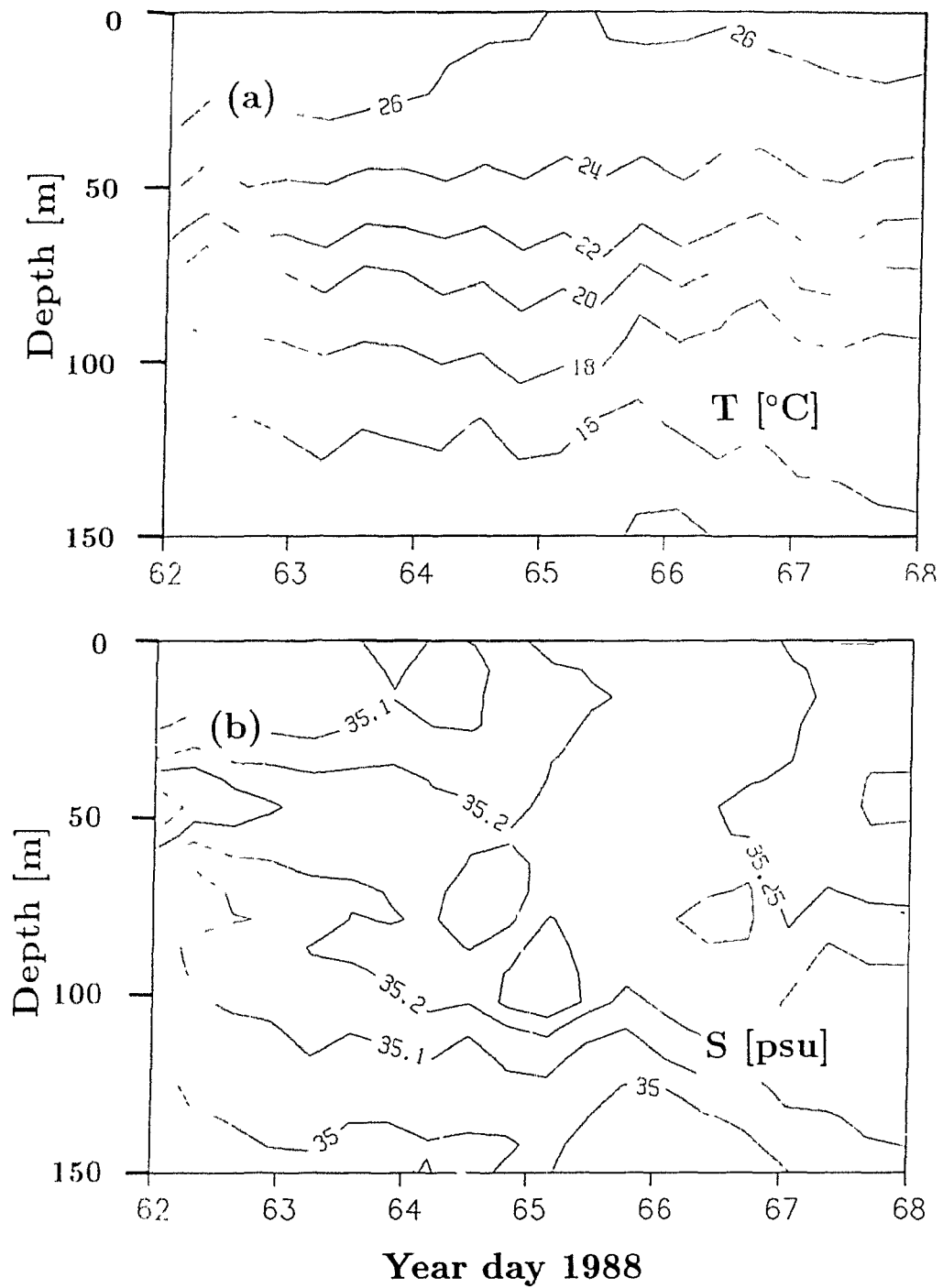


Figure 2.11: Contour plots of temperature (a) and salinity (b) for the time series at the equator.

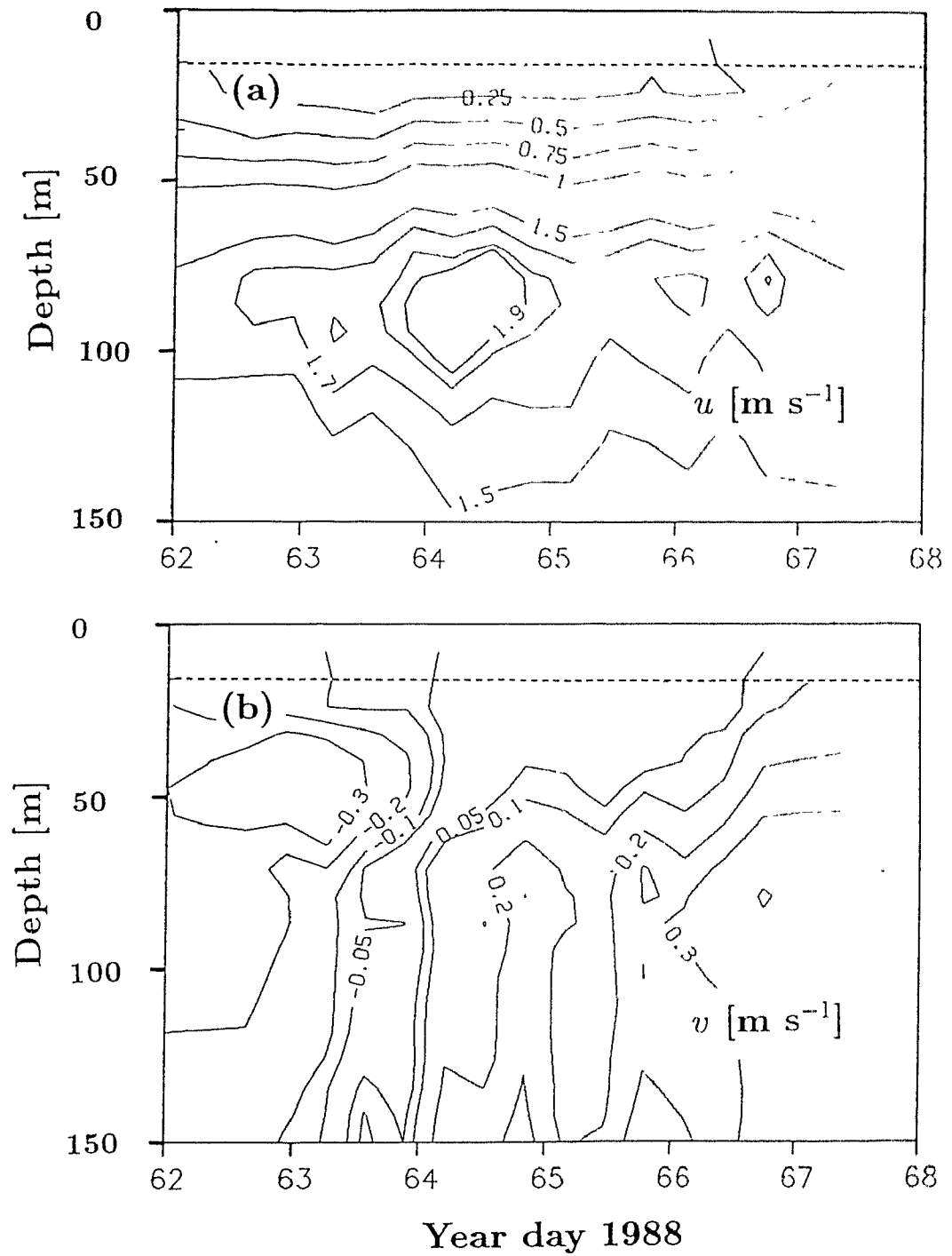


Figure 2.12: Contour plots of east-west velocity (a) and north-south velocity (b) for the time series at the equator. The dashed horizontal line is the reference level of no motion.

observed in the relative flow patterns. The increased nitrite concentrations (Figure 2.13b) ( $> 0.30 \mu\text{mol l}^{-1}$ ) are consistent with the change in sign of meridional velocity. Northward transport of water from south of  $0^\circ$  would explain the increase, as these values were not present at any depth at  $0^\circ$  prior to day 64, or to the north (see Figure 2.5d for meridional transect). It is possible that the EUC was not centered at the equator when we arrived and as a result of the northward velocity the zonal current system returned to  $0^\circ$  in the morning of year date 64. This would explain the intensification of the EUC at that time as well as the presence of cold, high nutrient water, observed in association with the EUC system.

An alternative explanation is that the observed increase in relative velocity of the EUC during our time series may be part of a large-scale increase in eastward transport. McPhaden and Hayes [1990] observed a sharp increase in EUC velocity at  $140^\circ\text{W}$  commencing in early March. This led to enhanced eastward mass convergence and increased upwelling in the region between  $140^\circ\text{W}$  and  $110^\circ\text{W}$ . The cooling of the surface waters associated with the 1988 La Niña are attributed by these authors to this increased zonal convergence and upwelling.

A third possible explanation is enhanced westward transport by the SEC. We have no reliable velocity data at such shallow depths, so inference must be made from the known conditions of the large-scale flow patterns. The westward flowing SEC is weak at this time of the year, and usually undergoes a springtime reversal (to flow east). In 1988, the usual reversal at  $140^\circ\text{W}$  started late, but did take place in March [McPhaden and Hayes, 1990]. If the spring reversal occurred at  $150^\circ\text{W}$  before or around our study period (year days 61–67), the zonal transport at the surface would have the effect of warming rather than cooling. If, however, the reversal took place after day 67, the SEC could be responsible for the cooling trend. The 10 m zonal velocity at  $140^\circ\text{W}$  intensifies towards the west before the reversal, which appears to take place at the second half of March [McPhaden and Hayes, 1990]. We do not know if this is similar to what occurred at our sampling site 1000 km away. Enhanced westward SEC velocities would bring colder, higher nutrient water to our sampling

site.

The changes in upper water column characteristics take place rapidly; this implies that the source water be relatively near. If the changes come about as a result of the meridional transport of the shifted zonal current system to  $0^\circ$ , the colder water would have had to be only slightly displaced. If the changes are a consequence of enhanced upwelling, the deep water with the appropriate characteristics is only tens of meters away. Meridional transport in the absence of a prior displacement of the current system from  $0^\circ$ , would lead to warming rather than cooling and lesser nutrient concentrations rather than an increase. The event after year day 64 could be associated with westward transport. The nutrient concentrations and temperature gradients are consistent with the observed changes but the distances involved would lead to a gradual change rather than an abrupt one.

There is no available information close to  $150^\circ\text{W}$  during our sampling period to confirm an increase in upwelling velocity. The enhanced eastward mass transport observed at  $140^\circ\text{W}$  [McPhaden and Hayes, 1990] is 1000 km away. The increase in nitrite concentration after day 64 supports a southern origin for the colder water observed at  $0^\circ$  thereafter. In conclusion, it appears that the observed changes result from the return of the 'displaced' zonal current system to  $0^\circ$  resulting from meridional transport.

The diurnal cycle in temperature is clearly visible in the surface layer (see Figures 2.10, 2.11 and 2.14), but not below 20 m. There is no apparent diurnal signal in salinity. Nitrate concentrations peak in the mixed layer during the late afternoon-night (see 5 and  $6 \mu\text{mol l}^{-1}$  isolines in Figure 2.13a). The chlorophyll time series shows a diurnal maximum (see the 0.3 and the shallow  $0.4 \mu\text{g l}^{-1}$  isolines in Figure 2.13c) at around 1800 hours, the signal of production during the day. This peak is no longer visible by morning, indicating a close coupling in time and space between the production and loss processes, *i.e.* the grazers respond rapidly. The diurnal cycle in chlorophyll standing stock and primary production is studied by Cullen *et al.* [1991]. Since the diurnal signals of nitrate and chlorophyll covary (both increase in

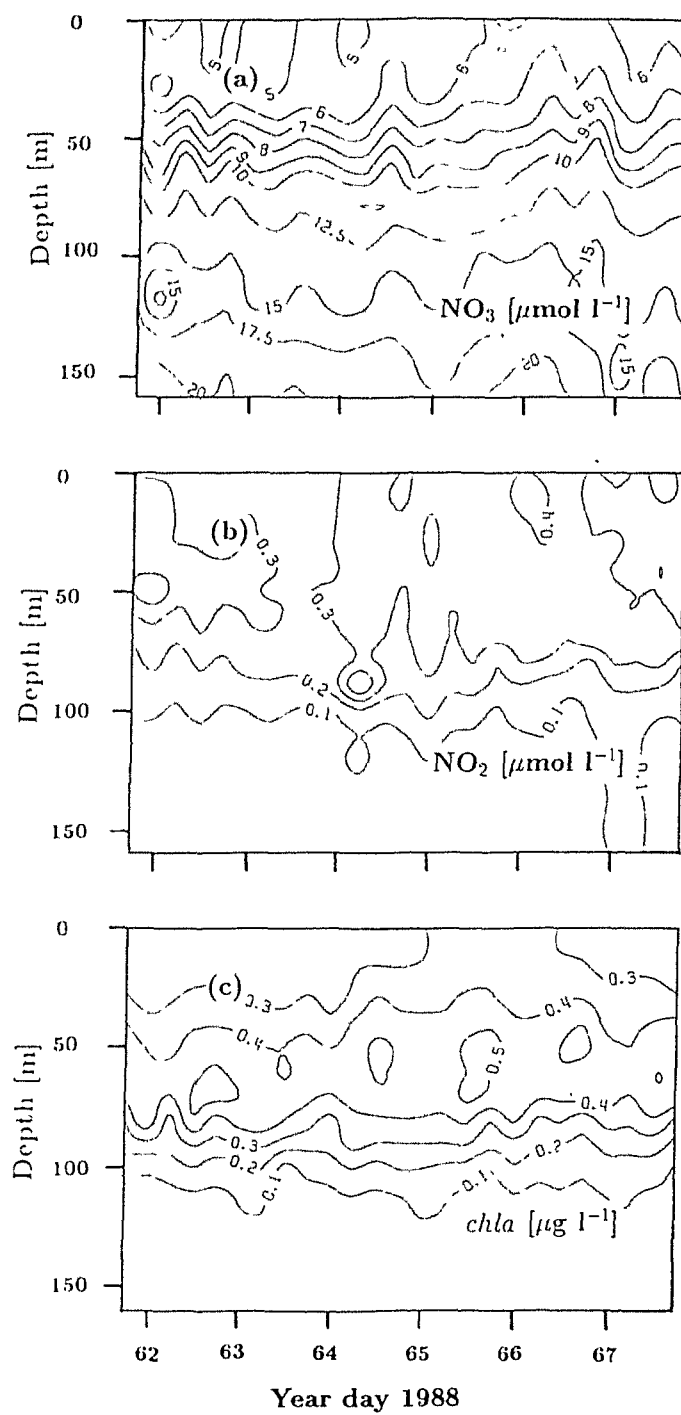


Figure 2.13: Contour plots of nitrate concentration (a), nitrite concentration (b) and chlorophyll concentration (c) at the equator.

the afternoon), this indicates that the variability in  $\text{NO}_3$  concentration is relatively uncoupled from the phytoplankton growth. A daily change of 0.2 to 0.3  $\mu\text{g l}^{-1}$  of chlorophyll is likely to result in an uptake of approximately 0.2 to 0.3  $\mu\text{mol l}^{-1}$  of inorganic nitrogen per day [B. Jones, pers. comm., 1990]. The increase in chlorophyll concentration is not accompanied by a corresponding decrease in nitrate concentration and at no point does nitrate fall to low levels. This confirms that nitrate is not limiting for phytoplankton growth.

### Stability, shear and Richardson number

The time series of  $N^2$ ,  $U_z^2$  and  $Ri$  (Figure 2.15) show that the major features in  $Ri$  reflect variability in  $N^2$ . Superimposed on the clear diurnal cycle of  $N^2$  at 15 m is an increase after day 64, reflecting the growing stratification (Figure 2.10). This increase is also observable at 25 m. Concurrently,  $N^2$  decreases at depth (especially evident at 45 m). The structure of the water column has changed by day 64.5: the well-mixed layer has been replaced by the upper pycnocline while the sharp gradient found at intermediate depths (40–70 m) at the start of the time series has become more gradually sloped.

The largest shear is observed between 40 and 60 m and is quite homogenous in that region ( $4 \cdot 10^{-3} \text{ s}^{-2}$ ). Below the core of the EUC the shears are also large but ELITESONDE was not able to penetrate to that depth so they have not been plotted here. The relative minimum late in day 65 corresponds to the weakening of both the EUC and the meridional flow at that time (Figure 2.4).  $Ri$  is less than 1/4 after day 64 from 40–60 m, and above 40 m (low  $N^2$ ) throughout the time series.

### 2.4.3 Temporal variability of dissipation and vertical mixing

The time series of  $\epsilon$  and  $\chi$  are plotted in Figure 2.16. The 95% confidence intervals of the mean value for the stations were calculated assuming a lognormal distribution [Baker and Gibson, 1987] and representative values are shown. We do not see the

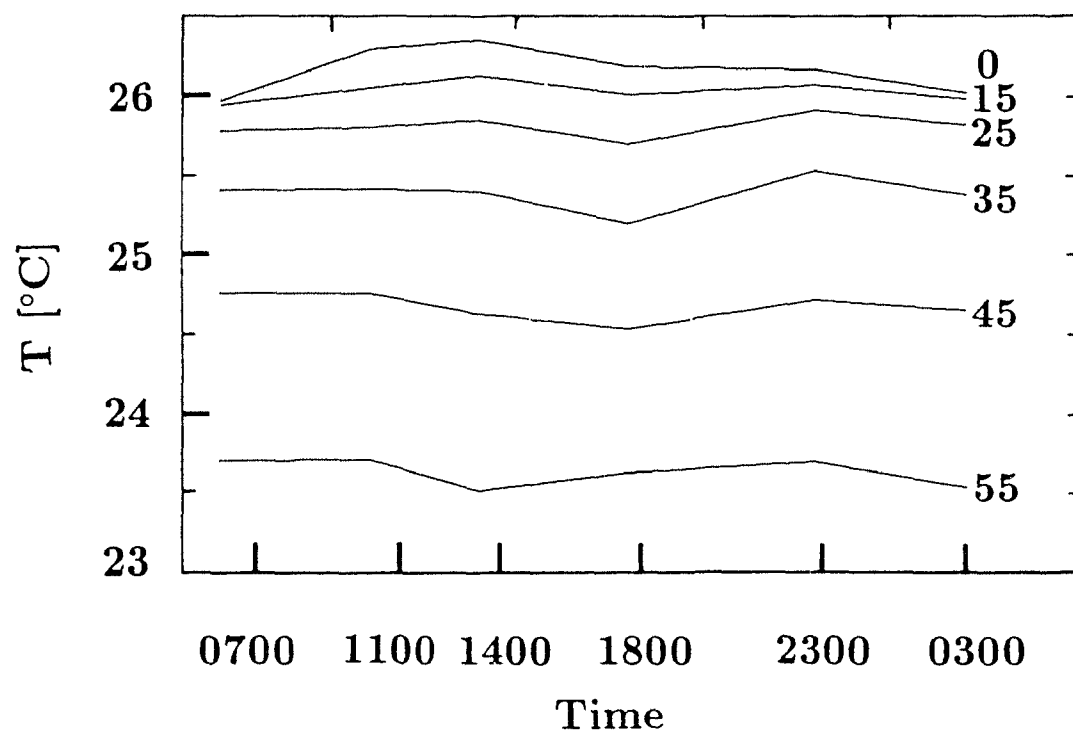


Figure 2.14: Canonical day in temperature at 0° at 0, 15, 25, 35, 45 and 55 m.

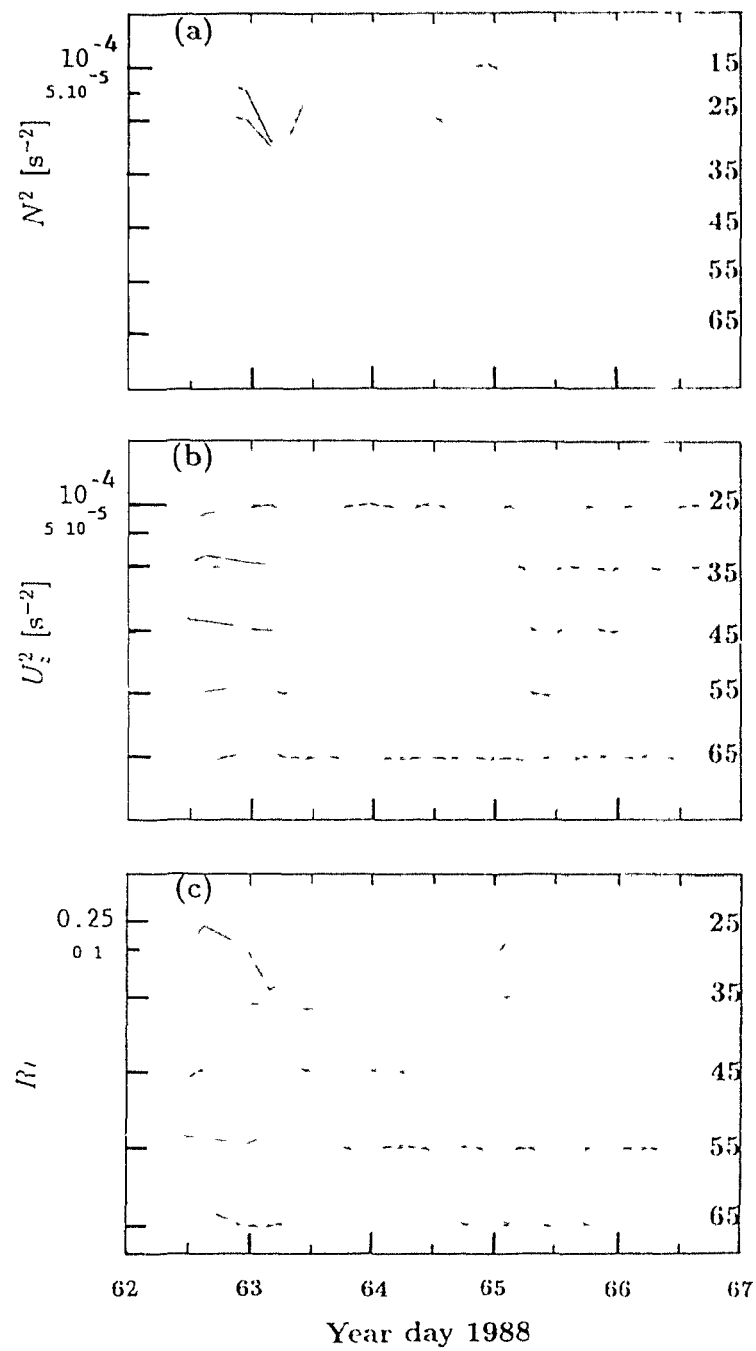


Figure 2.15: The  $N^2$  (a),  $U_z^2$  (b) and  $Ri$  (c) at  $0^\circ$ .

clear diurnal signal reported for the Tropic Heat 1 experiments [Gregg *et al.*, 1985, Moum *et al.*, 1989], with high values of  $\epsilon$  occurring at night and to great depth (100 m) and low values during the day as turbulent motion is suppressed by stratification.

In both  $\epsilon$  and  $\chi$ , the 15 m depth interval seems to be independent of the general features observed from 20 to 60 m. The 15 m depth interval shows some semblance of diurnal cycling with maximum values occurring during the night or late in the day and minima around noon. There is a conspicuous minimum on year day 63 in both  $\epsilon$  and  $\chi$ . This minimum coincides with a peak in  $N^2$  following the extreme low in the early hours of day 63. After year day 63.5 the values for  $\epsilon$  and  $\chi$  become larger. This increase occurs first in the deepest bin (50–60 m) and then moves towards the surface within a few hours. It is largest at 55 m (as well as the largest values of  $\epsilon$  and  $\chi$ ) and becomes smaller as it progresses upward. The steady increase in  $\epsilon$  and  $\chi$  corresponds to decreasing  $Ri$  (to close to 1/4) below 30 m after day 64 and with an increase of the already critical values at 25 m at the same time (Figure 2.15c). Insufficient information about the upper 20 m makes it difficult to reach any conclusion as to whether the 15 m bin is coupled to the deeper forcing or whether it is independent.

The observation of high  $\epsilon$  and  $\chi$  values at depth preceding the ones in shallower water is consistent with the observed intensification of the EUC (due to either to temporal variability or to its ‘arrival’ at the sampling site). Intense zonal velocities and upwelling modify the structure of the water column, converting the entirety of the sampled region into a weakly stratified thermocline.

### Diurnal cycling of $\epsilon$

The difference in the diurnal pattern of dissipation between the present data set and Tropic Heat 1 is especially clear when the data from the four and a half days are averaged by time of sampling to obtain the canonical day (Figure 2.17). The average dissipation between 10 and 70 m (Figure 2.17a) is greatest during the day, at 1100 and 1400 local time, and lowest at night, at 0300 and 0700. This diurnal progression results from very large dissipation values below 30 m at 1100 and 1400 ( $> 10^{-7}$  W kg $^{-1}$ )

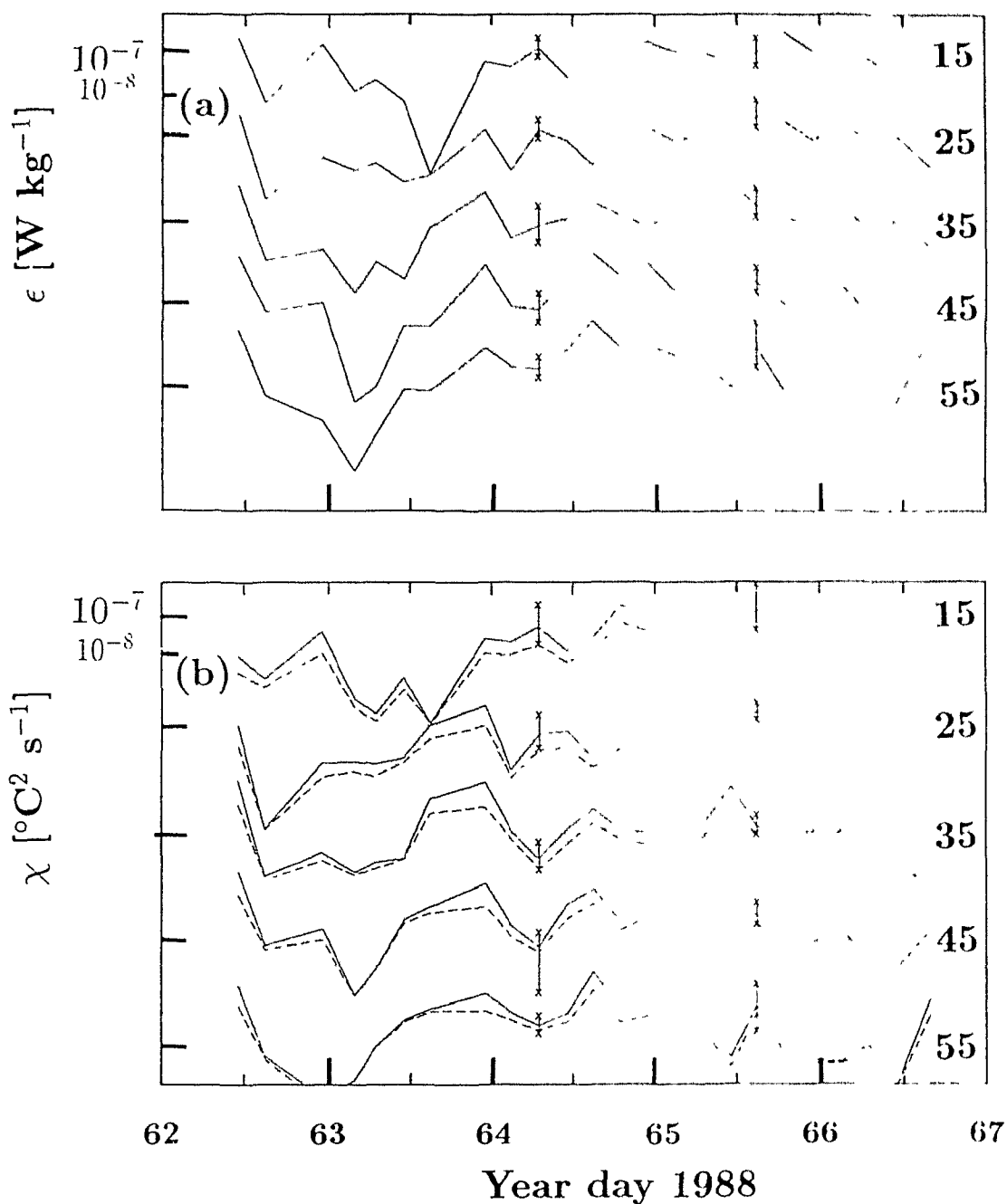


Figure 2.16: Time series of turbulent kinetic energy dissipation,  $\epsilon$  (a) and of dissipation of thermal variance,  $\chi$  (b) at the equator. The dashed line in (b) is the measured thermal variance and the solid line is the corrected value. The 95% confidence intervals for the stations have been calculated assuming a lognormal distribution and representative values are depicted.

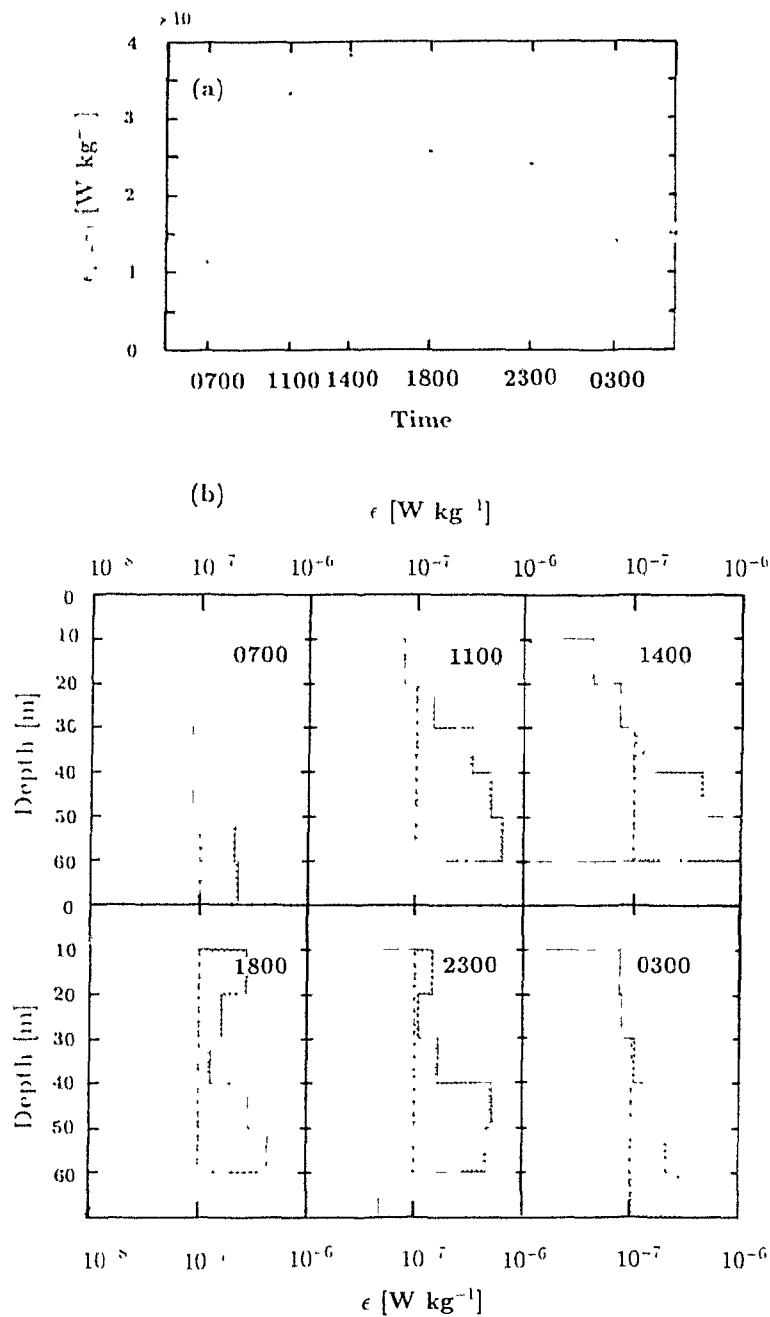


Figure 2.17: Canonical day in dissipation at 0°. The variation along the canonical day of the average dissipation between 10 and 70 m (a). The average dissipation for the Tropic Heat 1 canonical day [Moum *et al.*, 1989] is given by the empty circles. The depth structure of dissipation for each sampling time for the canonical day (b). The shaded area is greater than  $10^{-7}$  W kg<sup>-1</sup>.

(see Figure 2.17b). The dissipation between 10 and 30 m is greatest at night, from 1800 and 0700 and lowest at 1400. The diurnal cycle in dissipation is limited to the upper layer (30 m). The largest dissipation rates are observed below 40 m for all time periods and during the day. The high dissipation rates below the 'surface' layer mask the diurnal cycling of that layer, leading to a diurnal progression completely opposite that of the Tropic Heat 1 canonical day [Peters *et al.*, 1988, Moum *et al.*, 1989].

In Tropic Heat 1, the highest dissipation rates were observed after sunset. The surface values were largest then and the depth range of  $\epsilon$  greater than  $> 10^{-7} \text{ W kg}^{-1}$  extended downward as the night progressed. The average dissipation for the top 100 m (given in Figure 2.17a) shows a clear trend of larger dissipation values throughout the water column at night than in the day-time.

The atmospheric conditions of our study period (low wind speed, high incoming irradiance and low sea-surface temperatures) differ notably from those of Tropic Heat 1, where wind speeds were high (mean of  $9 \text{ m s}^{-1}$ ) and the air sea temperature difference was reversed at night [Moum *et al.*, 1989] leading to large surface heat losses ( $150\text{--}200 \text{ W m}^{-2}$ ). Deep night-time convection, accompanied by large rates of dissipation throughout large parts of the water column [Lombardo and Gregg, 1989], is not as likely to occur during our study period. Likewise, at low wind speeds, the downward propagation of heat absorbed at the surface is impeded, thus limiting the vertical extent of a strongly stratified diurnal layer [Hebert *et al.*, 1991b]. Another consequence of sampling in spring is the depth of the EUC. The EUC core was found at 78 m, much shallower than in the Tropic Heat measurements (125 m at  $140^\circ\text{W}$ ) [Peters *et al.*, 1988, Moum *et al.*, 1989]. This means that the associated region of high stratification is much closer to the surface and surface-driven mixing will be inhibited by stability at shallow depths.

The maximum value of dissipation is observed at depth and during the day. This corresponds to maximum values of shear (Figure 2.15) at this depth and time. The work of Chereskin *et al.* [1986] in Tropic Heat 1 revealed a strong diurnal signal of the shear associated with the diurnal tide in the upper 40 m. This was accompanied

by a strong cycle of buoyancy frequency with the same relative magnitude and phase. Consequently, the Richardson number did not cycle diurnally. In the present data, the diurnal signal of  $N^2$  was not as deep nor as strong as that of shear (because of the low wind speeds and large surface heating) and this led to a diurnal cycle in the Richardson number at depth. Thus, the diurnal progression in dissipation appears to be associated with the diurnal tide and is revealed as a consequence of the weak atmospheric forcing.

### Vertical diffusivity, $\Gamma$ and heat flux

The eddy diffusivity coefficients are given in Figure 2.18. The 15 m depth interval exhibits a diurnal cycle in  $K_\rho$  and  $K_T$ . Below 30 m, the patterns for the remaining depth bins are similar and seemingly independent of the surface forcing (Figure 2.9). The increase after year day 63 is noticeable for the 35, 45 and 55 m bins but is not for the two surface ones. The three coefficients present a very similar pattern, especially  $K_\rho$  and  $K_m$  below 30 m. The largest values are observed in the 15 m depth interval ( $K_T$  and  $K_\rho$ ) and from 40–60 m.  $K_T$  values were generally larger than  $K_\rho$ , especially at the surface. Conversely, in the Peters *et al.* [1988] study  $K_\rho$  was approximately 3 times the value of  $K_T$ .

A value for  $\Gamma$  was obtained by assuming that  $K_T$  and  $K_\rho$  should be the same: from Equations (2.5) and (2.7),  $\Gamma$  is found to be:

$$\Gamma = \frac{2 \chi N^2}{\epsilon (\partial \bar{T} / \partial z)^2} \quad (2.11)$$

The mean  $\Gamma$  for the equatorial time series from 10 to 60 m was 0.399. The 95% confidence intervals of the lognormal distribution were estimated according to Baker and Gibson [1987] and are given by  $0.062 < 0.399 < 1.376$ . This is somewhat larger than the value usually cited but is within the 95% confidence intervals for the distribution calculated by Oakey [1985]. Since  $\chi$  is not independent of  $\epsilon$  ( $\epsilon$  is used to correct for the poor frequency response of the thermistor), there is an implicit uncertainty in the above comparison. On average, the thermistor resolved only 47% of the thermal

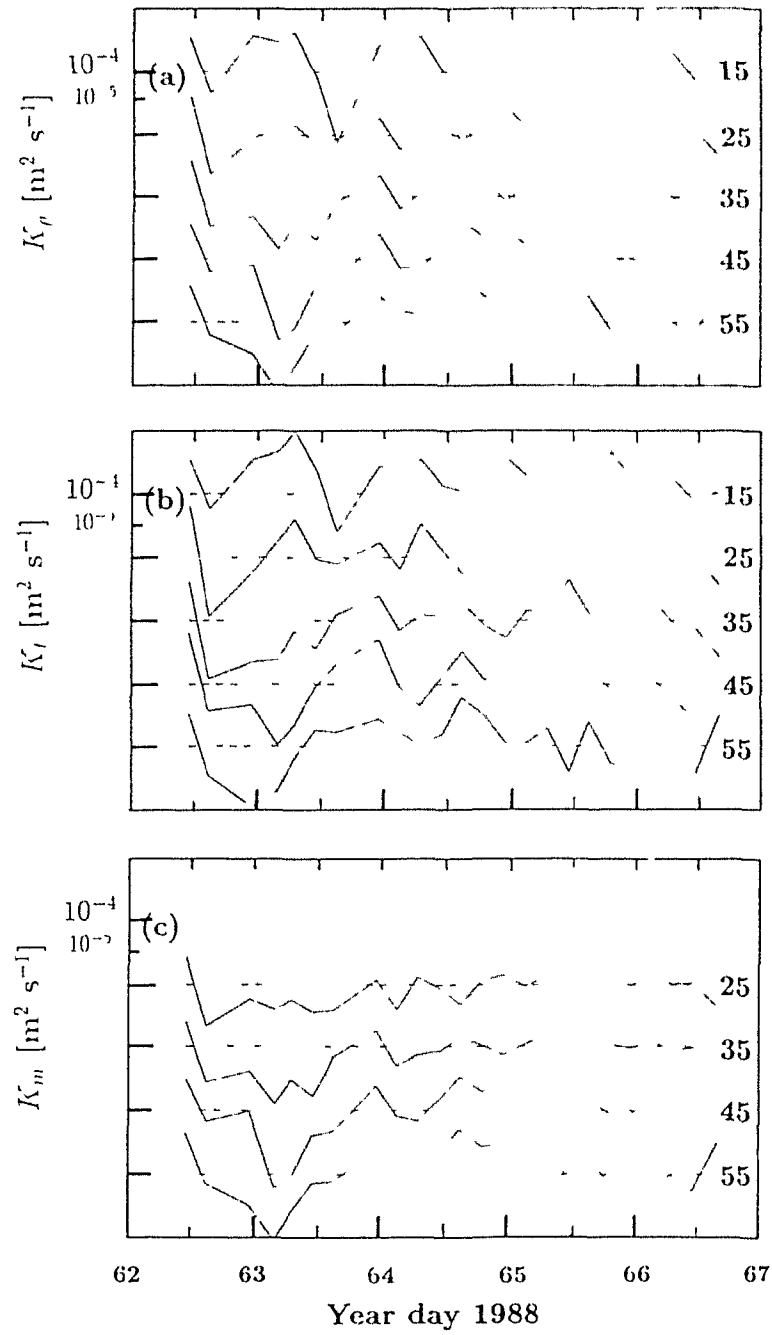


Figure 2.18: Time series of the vertical eddy diffusivity coefficient for heat,  $K_T$  (a), mass,  $K_\rho$  (b), and momentum,  $K_m$  (c) at the equator.

variance according to the theoretical Batchelor curve (see section 2.2.2) for the equatorial time series. This implies that the ‘measured’  $\Gamma$  is *ca.* 0.2. The fact that both the ‘measured’ and corrected values of the mixing efficiency are larger than the value of 0.1 obtained in Tropic Heat [Peters *et al.*, 1988] (their value does fall within our confidence intervals) reflects the relative values of  $K_T$  and  $K_\rho$  and is a consequence of the strong thermal stratification observed in the upper part of the water column.  $\Gamma$  is proposed to depend on  $Ri$  [Rohr and Van Atta, 1987], being low at very small  $Ri$  (well-mixed layers, low  $N^2$ ) then increasing as  $Ri \simeq 1/4$  and falling thereafter as increased stability impedes mixing. The smallest  $\Gamma$  values (mean for the profile, 0.09) were observed coinciding with the extreme  $N^2$  and  $Ri$  minimum near the end of year day 62 (Figure 2.15).

The turbulent vertical heat flux is shown in Figure 2.19. The top bin values are high close to midnight and lower during the day as a rule, but the diurnal variability is obscured by large daytime fluxes on days 62 and 63. The mixed layer is never deeper than 25 m so the top bin represents the loss of heat to the mixed layer. The increasing trend after day 64 is a consequence of the increasing thermal stratification from 10 to 20 m rather than of enhanced mixing. The 25 m depth bin also responds to the increased temperature gradient, and the downward flux is rarely of  $O(50 \text{ W m}^{-2})$ . It is below 30 m that the heat flux is largest. At these depths, temporal variability is determined by the  $K_T$  patterns, not the gradients (which decrease). On day 64 extraordinarily large heat fluxes are observed from 40–60 m, ranging from 500 to 1000  $\text{W m}^{-2}$  in response to  $K_T$  values of  $10^{-3} \text{ m}^2 \text{ s}^{-1}$ . This vertical structure is in contrast to the Tropic Heat results where maximum heat flux values were observed in the top 30 m (mixed layer) [Peters *et al.*, 1988, Moum *et al.*, 1989].

## 2.5 Parameterization of mixing

One of the goals of experiments such as Tropic Heat [Eriksen, 1985] has been to find a parameterization of mixing for the equatorial region using large-scale variables that

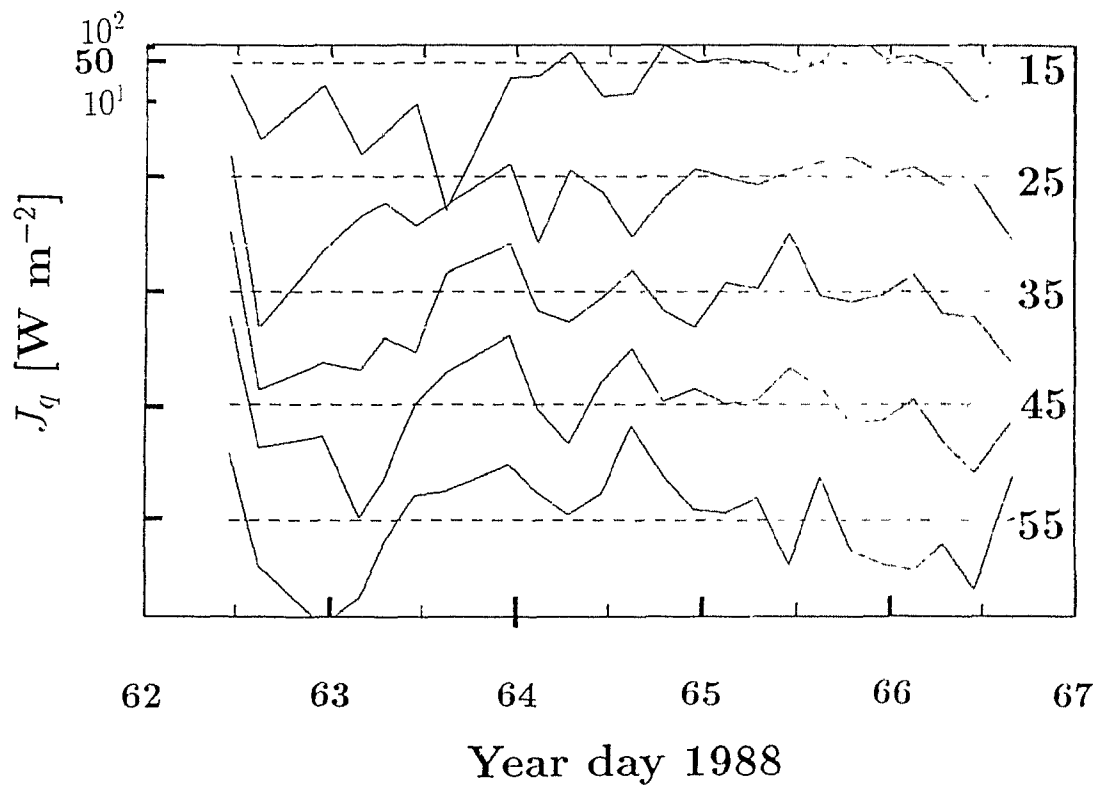


Figure 2.19: Time series of turbulent heat flux,  $J_q$ , at the equator.

are more easily obtained. Comparison has been made throughout our study between the fine-scale measurements made with the CTD and ADCP, which are gathered routinely on ships, and the microscale measurements. An estimate of mixing is obtained when we merge the microstructure parameters,  $\epsilon$  and  $\chi$ , with the large-scale observations such as the temperature gradient (for  $K_T$ ),  $N^2$  (for  $K_\rho$ ) and the velocity gradient (for  $K_m$ ). The variability in  $Ri$  has helped to understand the meridional and temporal patterns of  $\epsilon$  and  $\chi$  in the previous sections, as it determines the regions that are susceptible to turbulent mixing.

Modelling of equatorial dynamics has received new impetus as the global consequences of the interannual variability (ENSO) become increasingly evident [Philander, 1990]. As in all circulation models, there is an ongoing debate about a proper choice for diffusivity parameterization. Since the equatorial region is characterized by high stratification and a large mean steady shear, attempts have been made to find a parameterization based on the Richardson number [Pacanowski and Philander, 1981]. This is not straightforward because  $Ri$  provides a threshold criterion for turbulent mixing and there is not necessarily any proportionality between the value of  $Ri$  and the intensity of the mixing, which will depend instead on the forcing terms.

In the Pacanowski and Philander [1981] scheme,  $K(Ri)$  increases gradually as  $Ri$  becomes smaller. Comparison with actual data [Peters *et al.*, 1988] indicates that this parameterization is not appropriate for the low  $Ri$  found in the high shear zone of the EUC, where the mixing coefficient increased much more than predicted. Peters *et al.* [1988] suggested a parameterization with two separate expressions, a power function for the high shear zone and a second fit, with a functional form similar to that of Pacanowski and Philander [1981], for the high  $Ri$  values found in the core of the undercurrent.

Another approach was given by Moum *et al.* [1989]. They found that the distribution of  $Ri$  versus  $\epsilon$  also suggested a two-state process, with two distinct ‘populations’ of  $\epsilon$  for small and large  $Ri$ . They concluded that  $\epsilon$  was not a function of  $Ri$  and

proposed instead a cutoff value of  $Ri = 0.7$  which represents a boundary between the two regimes. If the measured  $Ri$  value falls above or below the cutoff, a mean  $\epsilon$  would be assigned accordingly from the ‘population’ of each regime.

Our data is more limited than that of Tropic Heat [Peters *et al.*, 1988, Moum *et al.*, 1989] as we were not able to penetrate the core of the EUC and therefore we do not have any data with high  $Ri$ . The effects of night-time convection did not penetrate below 20 m so the  $Ri$  link to  $\epsilon$  is not obscured by diurnal cycling.  $K_T$  is shown as a function of  $Ri$  in Figure 2.20. The gradually sloping Pacanowski and Philander parameterization does not apply to our observations, which resemble those of Peters *et al.* [1988] and Moum *et al.* [1989] for the high shear zone over the EUC. A linear least-squares fit of the diffusivity coefficient  $K_T$  to a power law of  $Ri$  was made and the relationship found was:

$$K_T = 3.91 \cdot 10^{-11} Ri^{-8.48 \pm 40} \quad [\text{m}^2 \text{ s}^{-1}] \quad (2.12)$$

This power law is comparable to those of Peters *et al.* [1988] for the upper shear zone, with low  $Ri$ . Although diffusivity decreases exponentially with increasing  $Ri$ , the scatter is considerable. This degree of uncertainty is not surprising since the highest dissipation values were found in the high shear zone below 40 m, while the lowest  $Ri$  were those of the upper 40 m (Figures 2.15 and 2.16). Our results confirm a lack of correlation between  $Ri$  and mixing intensity once critical values are approached.

In a recent paper by Schudlich and Price [1991] the equatorial diurnal cycle is modelled using the forcing measured during Tropic Heat and a diurnal upper ocean model. Mixing occurs due to shear flow instability such that the Richardson number does not fall below 1/4. Dissipation is estimated using the flux and shear profiles. Although the overall value of  $\epsilon$ , as well as the intermittent nature of dissipation are well simulated in the model, there is no correlation of the time series distribution to either the observations nor to the surface forcing. This is attributed to the presence of internal waves as triggers initiating instabilities in the real ocean.

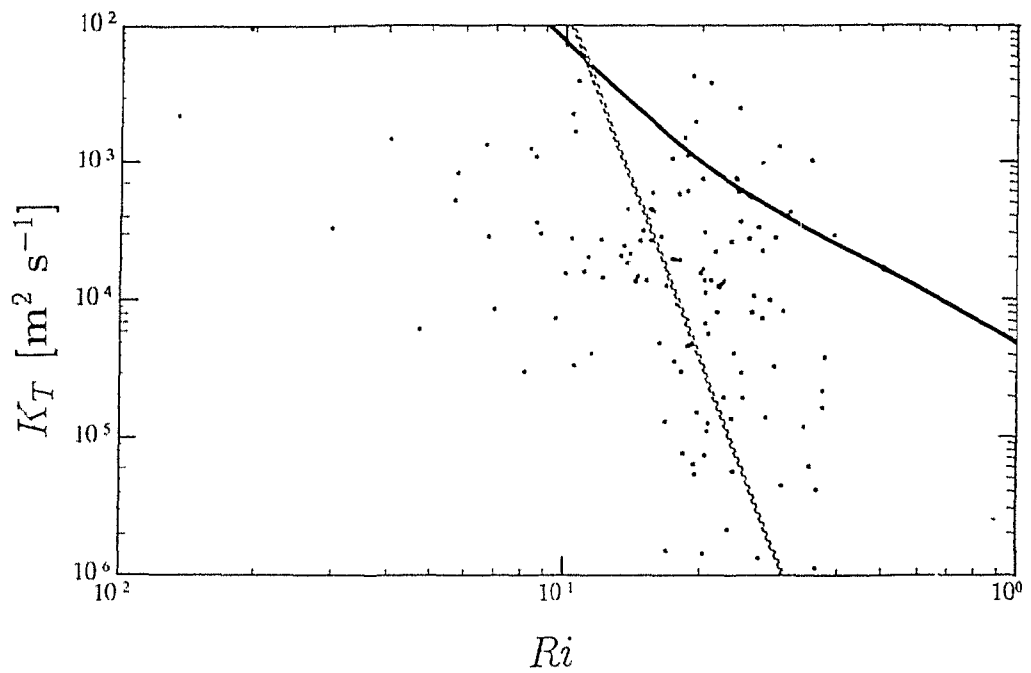


Figure 2.20: The eddy diffusivity coefficient as a function of the Richardson number:  $K_T$  versus  $Ri$ . The dashed line is the linear least-square power law that fits the data and the solid line is the parameterization of Pacanowski and Philander [1991].

## 2.6 Summary

1. The observed large-scale patterns of temperature, salinity, nutrients and chlorophyll were typical for boreal spring in the central equatorial Pacific. The flow pattern relative to 14 m corresponded to the classical circulation cell. The EUC was centered at 78 m, a typical depth for boreal spring.
2. There was a maximum in  $\epsilon$  and  $\chi$  in the equatorial region (between  $0^\circ$  and  $1^\circ\text{S}$ ) between 40 and 70 m. This maximum was significant to 95% confidence intervals obtained using the bootstrap method.
3. The  $Ri$ , estimated using measurements made with the CTD and ADCP, was useful in predicting the regions susceptible to turbulent mixing for the meridional transect. However, for the equatorial time series,  $Ri$  was not a good predictor of mixing. All  $Ri$  were lower than 0.45, as we were not able to sample the high  $Ri$  region of the EUC core. The lowest  $Ri$  were observed at the surface (lowest  $N^2$ ), while the largest  $\epsilon$  and diffusivities were found at 55 m.
4. In the equatorial time series, a change from southward to northward velocity was observed on year day 64. This was followed by intensification of the EUC. It is proposed that the change in meridional velocity returned the displaced EUC to  $0^\circ$ .
5. After year day 64, water temperature was lower and stratification, salinity, nutrient and chlorophyll concentrations were greater in the upper water column. Likewise,  $\epsilon$ ,  $\chi$  and vertical diffusivity values increased at that point.
6. At  $0^\circ$ , nitrate and chlorophyll concentrations increased together throughout the day-time period. This indicates that nitrate was not limiting for phytoplankton growth.
7. The expected diurnal cycle of  $\epsilon$  and  $\chi$ , with suppressed dissipation values during the day and large values at night, was limited to the top 20 m and was not very

pronounced. Maximum values of  $\epsilon$  and  $\chi$  were observed at depth (55 m) in the high shear zone above the EUC core. The three vertical diffusivity coefficients calculated, for heat ( $K_T$ ), mass ( $K_\rho$ ) and momentum ( $K_m$ ), revealed a stronger diurnal cycle but also limited to the upper 30 m.

8. Turbulent heat flux was maximum at depth, corresponding to high  $K_T$  and temperature gradients. The turbulent heat flux at the base of the surface layer was of the same order of magnitude as the penetrative irradiance and both were much smaller than the surface heat flux.

## Chapter 3

# The spatial pattern of dissipation, its relationship to surface forcing and the role of turbulent fluxes in large scale budgets

### 3.1 Introduction

In this chapter the focus is specifically on the microstructure measurements presented in the previous chapter and an attempt is made to explain the observed spatial and temporal variability. The equatorial maximum in dissipation is further tested to account for the limitations of sampling (section 3.3.1). In section 3.3.2, the dissipation values of the upper layer are analysed in terms of the forcing terms at the sea surface (wind stress and the convective buoyancy flux), and at depth (an estimate of the shear production term). In section 3.4.1, the vertical distribution of the turbulent stress observed during the equatorial time series is presented and compared with the annual mean zonal balance of momentum. A one-dimensional heat budget for the top 15 m at  $0^\circ$  is compared with the observed diurnal changes in heat content of the

layer (section 3.4.2).

## 3.2 Experimental methods

The experimental methods specific to the analyses in this chapter are given below. The wind stress is estimated using the winds corrected to 10 m measurements (see section 2.2.) in the following formulation:

$$\tau(0) = c_D \rho_a W^2 \quad [\text{N m}^{-2}] \quad (3.1)$$

where  $\rho_a$  ( $= 1.25 \text{ kg m}^{-3}$ ) is the density of air,  $W$  is the wind speed at 10 m, and the drag coefficient,  $c_D$ , was estimated iteratively using the Charnock formula as given in Smith [1988]. The zonal component of the wind stress is denoted by  $\tau^x(0)$ . The friction velocity is given by  $u_* = \sqrt{\tau/\rho_0}$ , where  $\rho_0$  is the water density at the sea surface. The wind energy input is expressed as

$$E10 = c_D \rho_a W^3 \quad [\text{W m}^{-2}] \quad (3.2)$$

The buoyancy flux utilized for all latitudes is the full expression from section 2.2 (Eq. (2.9)).

Energy from the wind stress and buoyancy flux generate mixing in the upper part of the water column, the mixed layer. The depth of this layer was defined as the depth at which the density was  $0.01 \sigma_T$  units larger than the surface value. This criterion is the same one used by Peters *et al.* [1988], Moum *et al.* [1980], Peters *et al.* [1989] and Hebert *et al.* [1991a] for the equatorial region. Figure 3.1 shows the mixed layer depth for the transect and for the equatorial time series.

To address the vertical structure of turbulent mixing the following parameters were defined. The average mixed layer dissipation is given by

$$\overline{\epsilon}_{ml} = \frac{1}{ml - 10} \int_{10}^{ml} \epsilon(z) dz \quad (3.3)$$

The dissipation measurements above 10 m have been discarded because of noise from wave action and ship motion. The dissipation in the top 10 m is undoubtedly significant [Oakey, 1985]. However, rather than assuming a constant or model dependent

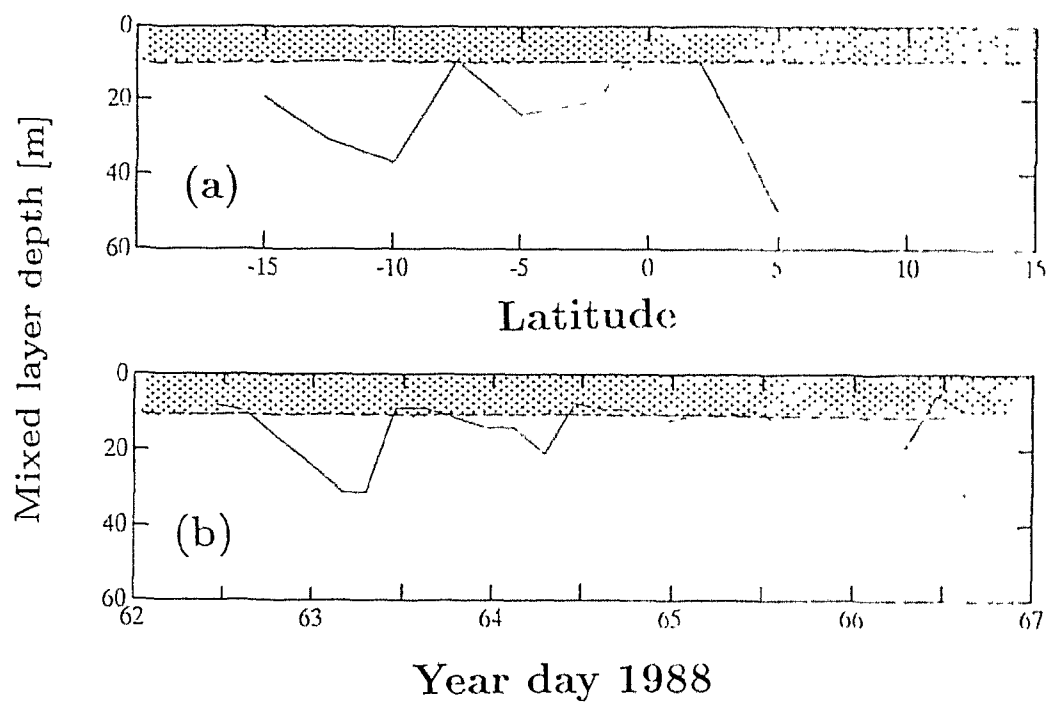


Figure 3.1: Mixed layer depth along the meridional transect (a) and during the equatorial time series (b); the microstructure data from the top 10 m are discarded because of noise from wave action and ship motion.

dissipation rate, this part of the water column was not included, thus rendering the following results directly comparable to other estimates of equatorial mixed layer dissipation [Peters *et al.*, 1989, Hebert *et al.*, 1991a]. The energy dissipated in the mixed layer is given in  $W\ m^{-2}$  by

$$E_{ml} = \rho \int_{10}^{ml} \epsilon(z) dz \quad (3.4)$$

The two surface forcing terms for turbulent dissipation: wind energy input expressed by the friction velocity,  $u_*$ , and the buoyancy flux,  $J_b$ , can be combined to provide a parameterization for mixed layer dissipation [Lombardo and Gregg, 1989, Peters *et al.*, 1989]:

$$\epsilon_{mod} = \frac{1}{ml - 10} \int_{10}^{ml} \left( 0.6J_b + \frac{u_*^3}{\kappa z} \right) dz \quad (3.5)$$

where  $\kappa$  is Von Karman's constant. This parameterization is thought to be applicable to both wind-dominated and convectively driven mixing as well as to intermediate cases [Lombardo and Gregg, 1989]. Estimates of  $\epsilon_{mod}$  have been made for each station of the meridional transect, using the concurrent wind and buoyancy flux value. When  $J_b$  was negative, it was set to zero and the wind determined the modelled dissipation rate [Peters *et al.*, 1989].

Moum *et al.* [1989] estimate the shear production term  $\langle u'w' \rangle U_z$  (where  $w'$  is the fluctuating vertical velocity) as  $u_*^2 U_z$ , where  $U_z$  is the shear between 10 and 25 m from the mooring at 140°W. We do not have mooring data, so the shear from the ADCP between 14 and 22 m has been used instead. This ADCP data is questionable because it is so close to the surface, but is presented here as proportional to the shear at the base of the mixed layer. The product of the friction velocity squared and the shear between 14 and 22 m is considered proportional to the shear production.

The relationship between the forcing terms and the energy dissipation in the water column has been studied on an individual station basis and also by averaging the stations at each latitude for the transect and in twelve-hour periods for the equatorial time series. The twelve-hour averages at 0° went between 0600 and 1800 for the day-time period and 1800 and 0600 for the night. The  $J_b$  value used was the average for

that time period at night and that of the previous night for the day-time period.

Correlation coefficients between the forcing terms and observed and modelled mixed layer dissipation rates were estimated for the latitude and twelve-hour equatorial averages using the bootstrap method [Efron and Gong, 1983] following the outline of Moum *et al.* [1989]. One hundred subsamples (of size eleven for the latitude averages and size eight for the time series) were drawn with replacement from the original population. The correlation coefficients between the different variables were estimated for each of the hundred subsamples; they are given as the mean  $\pm$  the standard deviation.

Analogously to the calculation of the turbulent heat flux (Chapter 2, Eq. (2.6)), the turbulent stress within the water column is given by the zonal shear (from ADCP) and the eddy diffusivity for momentum,  $K_m$  [Peters *et al.*, 1988, Dillon *et al.*, 1989]:

$$\tau^x(z) = -\rho K_m \frac{\partial u}{\partial z} \quad (3.6)$$

### 3.3 Vertical structure of dissipation along the meridional transect

#### 3.3.1 The equatorial maximum in turbulent dissipation

As shown in the previous chapter, the uncertainties of the data set have been addressed using the bootstrap method [Efron and Gong, 1983]. It was found in Section 2.4.3 that the equatorial maximum in dissipation is significant to 95% between 40 and 70 m depth, and the null hypothesis of constant dissipation along the transect was rejected.

However, sampling was concentrated at the equator, where there is a time series of twenty-four stations (approximately every four hours) (Figure 2.1). Within  $5^\circ$  of the equator (the region of interest for the equatorial maximum), there are only three to five stations at each latitude. It is plausible that we have introduced error in our off-equatorial estimates due to either sampling intensity, which may have been insufficient

to represent the local statistics or to sampling time, as we may have sampled the diurnal cycle inadequately. To address these uncertainties, the bootstrap procedure [Efron and Gong, 1983] and the conceptual outline of Peters *et al.* [1989] will be followed. It is proposed that the equatorial population could generate the observed meridional pattern, given insufficient sampling of the off-equatorial latitudes. The null hypothesis is that the dissipation does not vary along the meridional transect; since the most intensive sampling was at the equator, this is our basic data set. To test this hypothesis, two bootstrap tests will be performed: the first to test for the bias in sampling intensity and the second, to assess the error associated with insufficient sampling of the diurnal variability.

To test the sampling frequency, only data from the equatorial time series are used; the twenty-four residuals from the equatorial mean are subsampled  $n$  times (where  $n$  is still the number of stations at each latitude) for each latitude and depth interval. This is repeated 500 times and the 95% confidence intervals of the ‘bootstrap’ residuals are added onto the equatorial mean. In this way, an envelope of the expected values of dissipation is obtained at each latitude, assuming that the local rates were the same as at the equator, but had been sampled with only  $n$  stations. The shaded area of Figure 3.2a is thus the uncertainty associated with the null hypothesis. The observed dissipation values, even considering the large 95% confidence intervals of the latitude mean, are smaller than the 95% uncertainty associated with the null hypothesis between 40 and 70 m poleward of  $1^{\circ}\text{S}$  and  $0^{\circ}$  (Figure 3.2a). The uncertainty of the mean dissipation at  $0^{\circ}$  is larger than the confidence limits of the tested hypothesis, because the latter is derived from the equatorial population alone while the uncertainty of the mean was obtained using the variance of the entire transect.

To test the inadequate sampling of the diurnal cycle away from  $0^{\circ}$ , the samples taken during the segments of the diurnal period that are missing from each off-equatorial latitude are removed from the equatorial ensemble. The reduced ensembles each have a different mean and new populations of residuals are obtained;

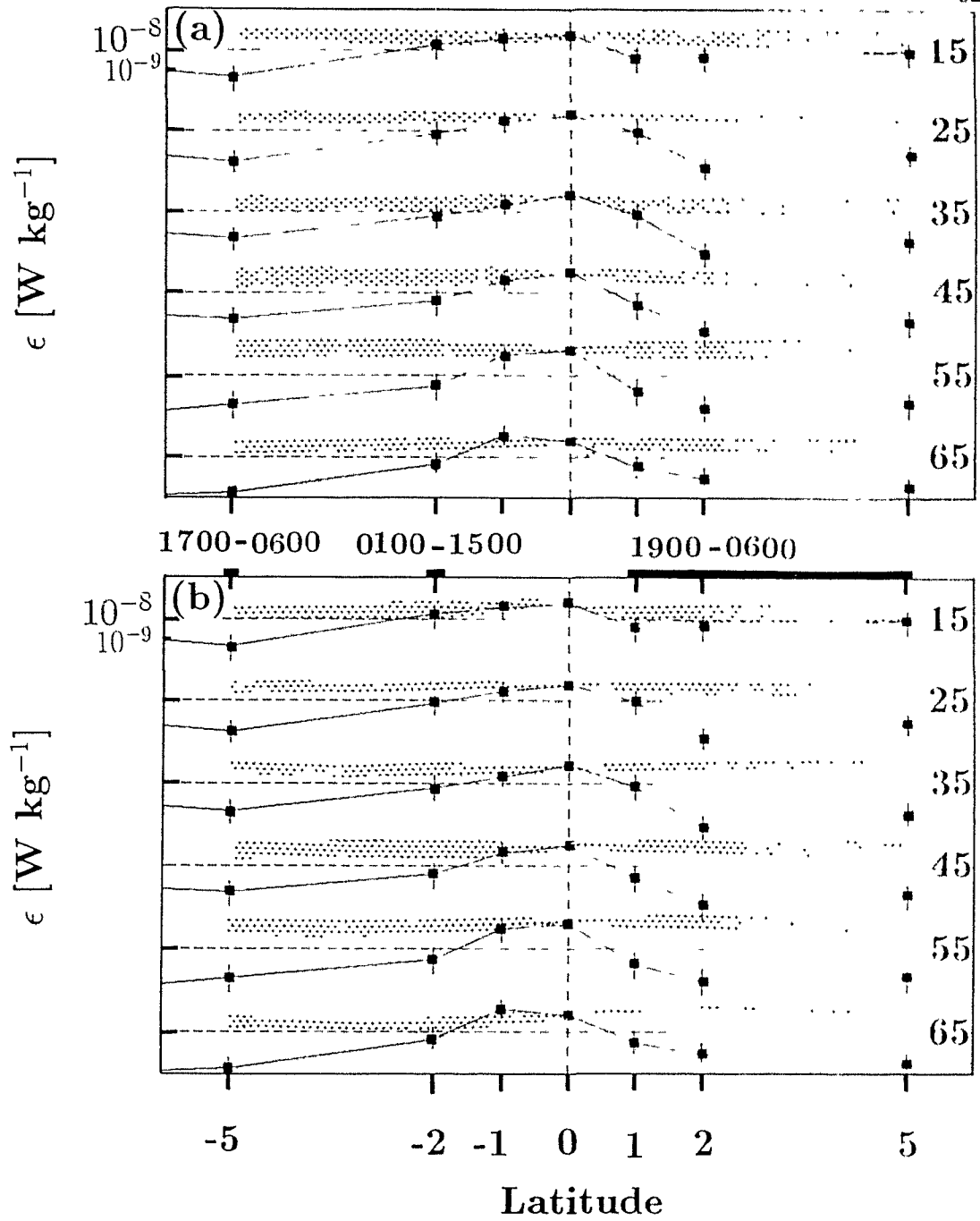


Figure 3.2: Meridional pattern of turbulent dissipation assuming the null hypothesis that the equatorial population could have generated the observed pattern given the errors introduced due to sampling frequency and time during the diurnal cycle. The shaded areas show the 95% uncertainty associated with the sampling intensity (a) and time of sampling (b) of the equatorial population at each latitude. The solid line and squares are the mean at each latitude and the error bars indicate the 95% confidence intervals of the latitude averages.

the bootstrap procedure is then applied to each. For example, at 2°S, no microstructure measurements were made between 0100 and 1500. All stations sampled during this period are removed from the equatorial ensemble; the mean is estimated and a population of residuals from the mean calculated. The reduced ensemble is then subsampled  $n = 4$  times and the  $n$  subsamples are averaged. The subsampling is repeated 500 times to obtain the ‘bootstrap’ population. The 95% confidence intervals of the new mean are then found from the ‘bootstrap’ population for each depth interval. The gaps in the diurnal cycle were between 1900 and 0600 for 1°N–5°N, 0100 to 1500 for 2°S and 1700–0600 for 5°S. There was no gap in the diurnal period at 1°S. Once again, the equatorial maximum (1°S–0°) is found to be significant to 95% below 40 m (Figure 3.2b).

In conclusion, the equatorial maximum is a statistically robust feature, as it is significant even taking into account the uncertainties of the off-equatorial sampling. The bootstrap method will underestimate the confidence intervals if the local statistics are not properly represented; it has been assumed here that the equatorial population is adequately sampled. Given the intermittent nature of turbulent mixing as revealed by continuous sampling, we may actually have undersampled even at 0°.

### 3.3.2 The depth structure of dissipation: similarity scaling

A major result of the Tropic Heat experiments carried out in 1984 was the strong diurnal cycle in turbulent dissipation [Gregg *et al.*, 1985, Peters *et al.*, 1988, Moum *et al.*, 1989]. They found that night-time and day-time levels of turbulence differed by a factor of 100 and the high night-time dissipation rates extended to great depth. The turbulent dissipation rates were also influenced by the local winds [Moum and Caldwell, 1985, Moum *et al.*, 1989, Hebert *et al.*, 1991a]. In our time series, the classical diurnal cycle in dissipation (with maximum values at night) only extended to 20 m (see Chapter 2). In this section, the relationship between the forcing terms and the observed dissipation rates is examined for the upper part of the water column.

Energy for mixing is input at the sea surface through buoyancy flux or wind stress. When the buoyancy flux,  $J_b$  (Eq. (2.10)) is positive (at night), it is a source of energy for turbulent mixing [Lombardo and Gregg, 1989]. During the day, solar heating increases the buoyancy of the upper part of the water column. This day-night variability imposed at the surface leads to a diurnal cycle in mixed layer depths and in turbulent dissipation rates [Gregg *et al.*, 1985, Moum and Caldwell, 1985, Peters *et al.*, 1988, Moum *et al.*, 1989]. An additional surface forcing term is the wind stress. The wind energy that enters the ocean is estimated to be around 2–10% of the value 10 m above the surface,  $E_{10}$  [Richman and Garrett, 1977]. Only 0.1% of  $E_{10}$  goes into deepening the surface mixed layer [Denman and Miyake, 1973]. A much larger portion is dissipated by small-scale mixing: Oakey and Elliott [1982] and Oakey [1985] found that the rate of energy dissipated within the mixed layer was 1% of the wind energy at 10 m. This means that between 10 and 50% of the energy penetrating the air-ocean interface is dissipated by turbulent mixing. Similar results were observed at the equator, where Moum *et al.* [1985] found that the integrated dissipation in the upper water column was 0.92% of  $E_{10}$ .

The average dissipation of the mixed layer,  $\overline{\epsilon_{ml}}$  (Eq. (3.3)) and the total energy dissipated,  $E_{ml}$ , were estimated for the transect data and the equatorial time series and then compared with the surface forcing terms:  $J_b$  from Eq. (2.10) and the wind energy flux at 10 m,  $E_{10}$  from Eq. (3.2). These variables have been studied on an individual station basis and also by averaging each latitude for the transect and twelve-hour periods for the equatorial time series (Table 3.2). The poor relationship observed between the dissipation values and the surface forcing terms at the equator suggests an alternative forcing process; the role of shear at the base of the mixed layer is then explored.

### Surface forcing along the transect

It was generally found that there was no relationship between the wind and the dissipation rate in the mixed layer. Comparison between the wind energy flux at

10 m and the average mixed layer dissipation (Figure 3.3) for all the stations of the transect shows that in spite of a general trend of increasing dissipation with higher wind energy, the scatter is considerable. The solid line is the relationship suggested by Oakey [1985] for the top 20 m of the North Atlantic site studied during the JASIN experiment. For the latitude averages (Figure 3.3), the relationship between wind energy and the mixed layer dissipation improved somewhat over the individual station case ( $r = 0.47 \pm 0.39$ ) (Table 3.1), but is still very weak. As found by Hebert *et al.* [1991b], for a given wind speed, the mixed layer (or thermocline) dissipation is greater in the equatorial region ( $1^\circ\text{S}-0^\circ$ ) than away from  $0^\circ$ . This can be seen for both the individual stations and the latitude averages (Figure 3.3).

The buoyancy flux is an energy source for mixing in convective conditions. The relationship between the night-time buoyancy flux and the dissipation of the upper layer is tenuous in the meridional transect. For the individual stations, the relationship between  $J_b$  of the previous night and the mixed layer dissipation is not clear. For the latitude averages, the night-time buoyancy flux and the mean dissipation were weakly correlated, but the associated uncertainty is large (Table 3.1). The relationship between the individual stations and the concurrent  $J_b$  was positive, because negative buoyancy fluxes correlate with the very small mixed layer dissipation rates during the day. The ratio between the average mixed layer dissipation and the surface buoyancy flux is usually around 0.6–0.7 [Lombardo and Gregg, 1989, Peters *et al.*, 1989]. The average ratio for all stations of the present study was 1.05, comparable to the expected value for surface-forced mixed layer turbulence.

The mixed layer dissipation was modelled using the friction velocity and the buoyancy flux with Eq. (3.5). The observed and modelled dissipation rates are shown in Figure 3.4. It was found that off the equator, the modelled dissipation rate (dashed line) was larger than the observed values, while at  $0^\circ$ , the observed mixed layer dissipation was greater. For the latitude averages, the modelled and observed mixed layer dissipation rates were positively correlated,  $r = 0.58 \pm 0.23$ .

Table 3.1: Surface forcing in the meridional transect. Correlation matrix of the latitude averages of surface forcing terms and dissipation. The correlation coefficients were estimated for each of one hundred bootstrap subsamples of the original data set and are given here as the mean  $\pm$  the standard deviation.

	$\overline{\epsilon_{ml}}$	$\epsilon_{mod}$	$J_b$	$\tau$
$\overline{\epsilon_{ml}}$	1	0.58( $\pm 0.23$ )	0.43( $\pm 0.29$ )	0.47( $\pm 0.39$ )
$\epsilon_{mod}$		1	0.83( $\pm 0.15$ )	0.59( $\pm 0.30$ )
$J_b$			1	0.78( $\pm 0.14$ )
$\tau$				1

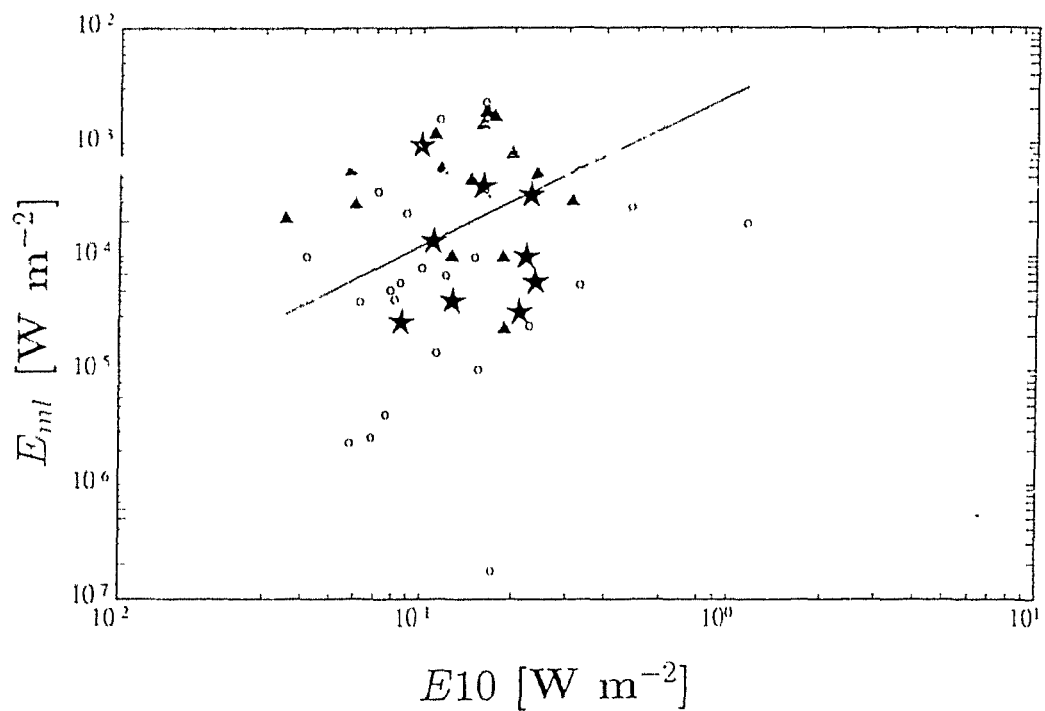


Figure 3.3: Scatter plot of the total energy dissipated in the mixed layer *versus* the wind energy flux at 10 m for the meridional transect. The equatorial stations are shown as triangles. The latitude averages are portrayed as stars. The line is the relationship from Oakey [1985].

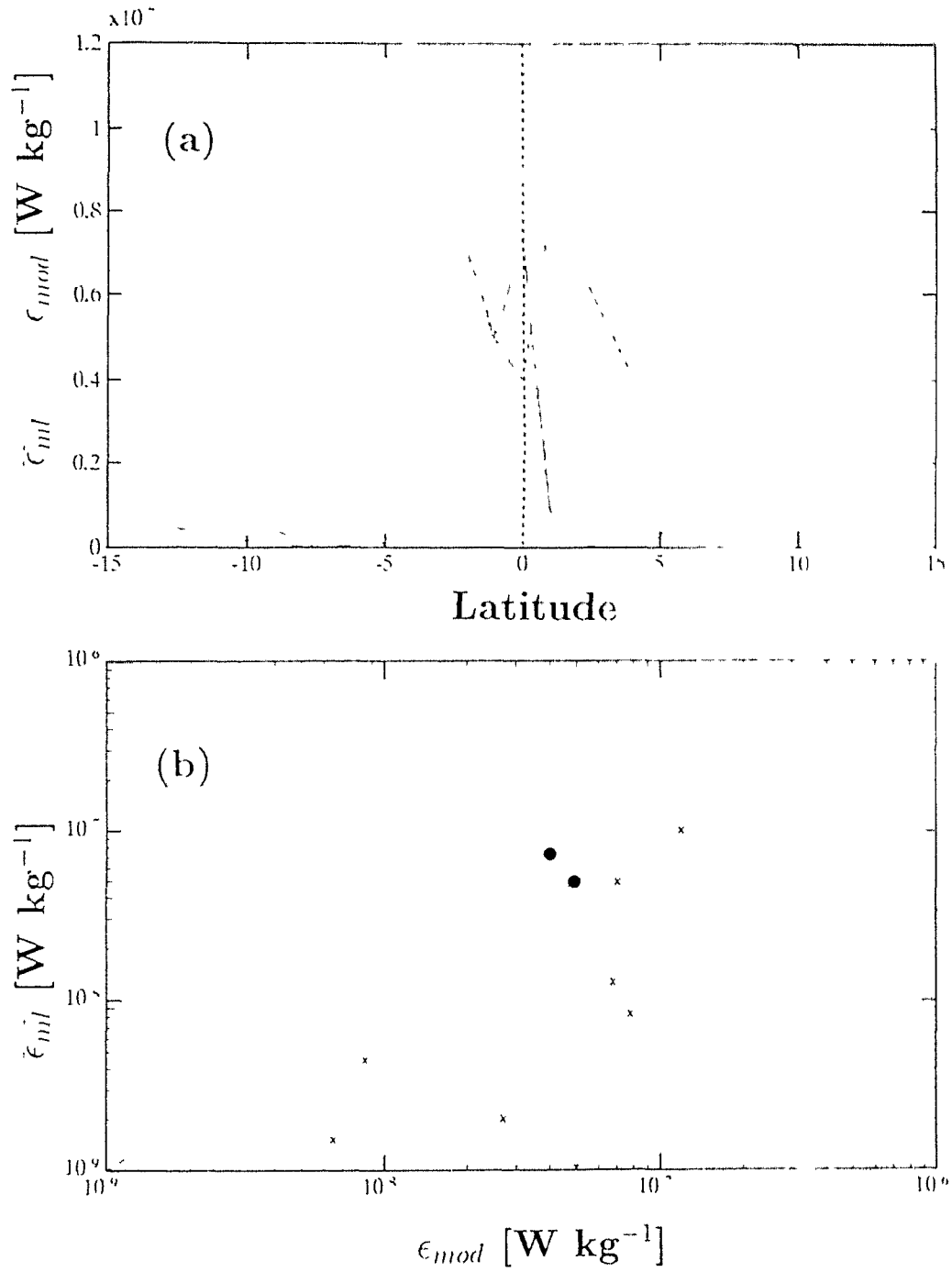


Figure 3.4: Dissipation modelled using similarity scaling (dashed line) and measured mixed layer dissipation (solid line) (a) for the latitude averages along the transect. Relationship between the modelled and observed dissipation rates for the latitude averages (b); the filled circles are the values for 0° and 1°S.

### Forcing in the equatorial time series

For the equatorial time series, comparison between the forcing at the surface and at depth and the mixed layer dissipation was made for individual stations (approximately every four hours) and for twelve-hour averages. The mixed layer dissipation (from Eq. (3.3), and  $\epsilon_{mod}$  from Eq. (3.5) together with  $J_b$ ,  $E10$ , the shear between 14 and 22 m ( $U_z$ ) and the shear production term ( $u_*^2 U_z$ ) were averaged over twelve-hour periods and are shown in Table 3.2. It is clear from Table 3.2 that the night-time mixed layer dissipation increases from year day 64 to 66. The night-time buoyancy flux,  $J_b$ , decreased after maximum values on year day 63 and then was relatively constant for the remaining three days. The wind energy flux was also almost constant, with lowest values on the night before year day 64;  $E10$  was greatest during the day-time, starting on day 64.5. The shear fell to a minimum on 63.5 and then increased gradually after day 64.5 as did the ‘shear production’ term, which is at a minimum on year day 64. The ratio between observed and modelled dissipation increased three-fold to maximum values on year day 66.

For the equatorial time series, the energy dissipated in the mixed layer,  $E_{ml}$ , was around 1% of the wind energy flux,  $E10$ , but any relationship is confounded by the frequent occurrence of shallow mixed layers coinciding with high wind speeds during the day (Figures 3.1 and 3.5); the temporal patterns of  $E_{ml}$  and  $E10$  do not match. For the twelve-hour averages of the time series, likewise, there was no relationship ( $r = -0.12 \pm 0.35$ ) between the wind energy flux and the mixed layer dissipation (Table 3.3).

The daily averages of mixed layer dissipation and the  $J_b$  of the previous night are negatively correlated as the buoyancy flux decreased and the dissipation increased with time (Tables 3.2 and 3.3). Moum *et al.* [1989] found that the ratio between  $\overline{\epsilon_{ml}}$  and  $J_b$  was 2.2 at the equator. For the present time series, the night-time mixed layer dissipation rates were 1.6 times the buoyancy flux.

As was found in Tropic Heat 1 [Peters *et al.*, 1988, Moum *et al.*, 1989, Peters *et al.*, 1989], dissipation modelled using similarity scaling was smaller than

Table 3.2: The twelve-hour average mixed layer dissipation and forcing terms for the equatorial time series. The day-time period was taken from 0600 to 1800 and the night-time goes from 1800 to 0600; they are denoted by the mid-point of each period. The day-time buoyancy flux is that of the previous night.

	$\overline{\epsilon_{ml}}$	$J_b$	$E_{10}$	$U_z$	$u_z^2 U_z$	$\overline{\epsilon_{ml}}/\epsilon_{mod}$
	W kg <sup>-1</sup>	W kg <sup>-1</sup>	W m <sup>-2</sup>	s <sup>-1</sup>	W kg <sup>-1</sup>	
<b>63</b>	$7.91 \cdot 10^{-8}$	$7.66 \cdot 10^{-8}$	$2.37 \cdot 10^{-1}$	$2.15 \cdot 10^{-2}$	$8.36 \cdot 10^{-7}$	0.89
<b>63.5</b>	$7.80 \cdot 10^{-9}$	$7.66 \cdot 10^{-8}$	$1.54 \cdot 10^{-1}$	$1.67 \cdot 10^{-2}$	$4.68 \cdot 10^{-7}$	0.24
<b>64</b>	$5.93 \cdot 10^{-8}$	$5.84 \cdot 10^{-8}$	$4.77 \cdot 10^{-2}$	$1.86 \cdot 10^{-2}$	$2.44 \cdot 10^{-7}$	0.79
<b>64.5</b>	$4.99 \cdot 10^{-8}$	$5.84 \cdot 10^{-8}$	$1.49 \cdot 10^{-1}$	$2.25 \cdot 10^{-2}$	$6.47 \cdot 10^{-7}$	1.82
<b>65</b>	$1.11 \cdot 10^{-7}$	$6.15 \cdot 10^{-8}$	$1.47 \cdot 10^{-1}$	$2.22 \cdot 10^{-2}$	$6.26 \cdot 10^{-7}$	2.3
<b>65.5</b>	$7.65 \cdot 10^{-8}$	$6.15 \cdot 10^{-8}$	$2.19 \cdot 10^{-1}$	$2.42 \cdot 10^{-2}$	$8.91 \cdot 10^{-7}$	3.25
<b>66</b>	$2.06 \cdot 10^{-7}$	$6.24 \cdot 10^{-8}$	$1.09 \cdot 10^{-1}$	$2.68 \cdot 10^{-2}$	$6.03 \cdot 10^{-7}$	3.99
<b>66.5</b>	$4.55 \cdot 10^{-8}$	$6.24 \cdot 10^{-8}$	$2.14 \cdot 10^{-1}$	$2.87 \cdot 10^{-2}$	$1.06 \cdot 10^{-6}$	1.58

Table 3.3: Forcing in the equatorial time series. Correlation matrix of the twelve-hour averages of forcing terms and dissipation at  $0^\circ$ . The correlation coefficients between the different variables were estimated for each of one hundred subsamples of the original data set (Table 3.2) and are given here as the mean  $\pm$  the standard deviation.

	$\overline{\epsilon_{ml}}$	$J_b$	$E10$	$U_z$	$\overline{\epsilon_{ml}}/\epsilon_{mod}$
$\overline{\epsilon_{ml}}$	1	-0.26( $\pm 0.40$ )	-0.12( $\pm 0.35$ )	0.79( $\pm 0.17$ )	0.80( $\pm 0.15$ )
$J_b$		1	0.51( $\pm 0.25$ )	-0.36( $\pm 0.42$ )	-0.46( $\pm 0.41$ )
$E10$			1	0.17( $\pm 0.43$ )	0.04( $\pm 0.45$ )
$U_z$				1	0.94( $\pm 0.04$ )
$\overline{\epsilon_{ml}}/\epsilon_{mod}$					1

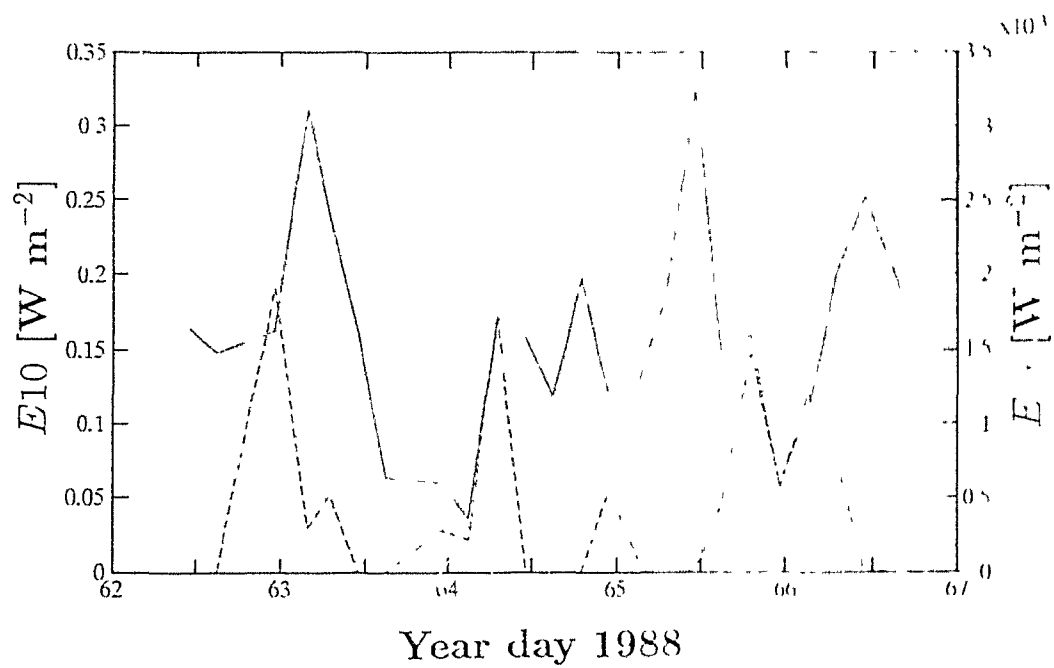


Figure 3.5: Time series of wind energy flux at 10 m (solid line and left-hand axis), and energy dissipated by turbulent mixing (dashed line and right-hand axis) in the mixed layer.

the observed mixed layer average (Figure 3.4a) at  $0^\circ$ . The relationship between observed and modelled dissipation is shown in Figure 3.6 for the equatorial time series; the two were only weakly correlated ( $r = 0.32$ ) For the twelve-hour averages, the relationship was poor as well ( $r = 0.21 \pm 0.25$ ).

The fact that the dissipation rate modelled from the surface forcing terms was smaller than the observed value indicates that there was an additional source of energy. This may be shear production at the base of the mixed layer [Lombardo and Gregg, 1989]. Peters *et al* [1989] found that changes in the shear derived from mooring data were correlated to the excess in dissipation rates over the modelled values. In the case of the individual stations of the time series, the correlation between shear and mixed layer dissipation was weakly positive ( $r = 0.25$ ); this was also the case for the ratio of observed and modelled dissipation rates and shear ( $r = 0.28$ ). For the twelve-hour averages, the  $\overline{\epsilon_{ml}}$  was well explained by the shear alone ( $r = 0.79 \pm 0.27$ ). Likewise, the ratio of observed and modelled dissipation is highly correlated to the shear between 14 and 22 m,  $r = 0.94 \pm 0.04$  (Figure 3.7 and Table 3.3). The ‘shear production’ term and the mixed layer dissipation were not correlated for the daily averages because of the poor relationship between mixed layer dissipation and wind energy flux (Table 3.3).

In conclusion, the presented results at  $0^\circ$  are similar to those of Peters *et al.* [1989] and Moum *et al.* [1989] in the following points. The change in sign of the buoyancy flux is decisive in initiating changes in depth of the mixed layer. However, surface forcing alone is insufficient to account for the observed  $\overline{\epsilon_{ml}}$ . As in the 12-day time series in Tropic Heat 1 [Moum *et al.*, 1989], the daily average of mixed layer dissipation is correlated to the shear between 14 and 22 m. The ratio between observed and modelled dissipation is also highly correlated to the shear at the base of the mixed layer, as was found by Peters *et al.* [1989].

This data set differs from Tropic Heat 1 in the lack of a relationship between dissipation and the local wind speed and in the absence of a deep diurnal cycle in dissipation. The preliminary conclusion in the previous chapter as to the reason

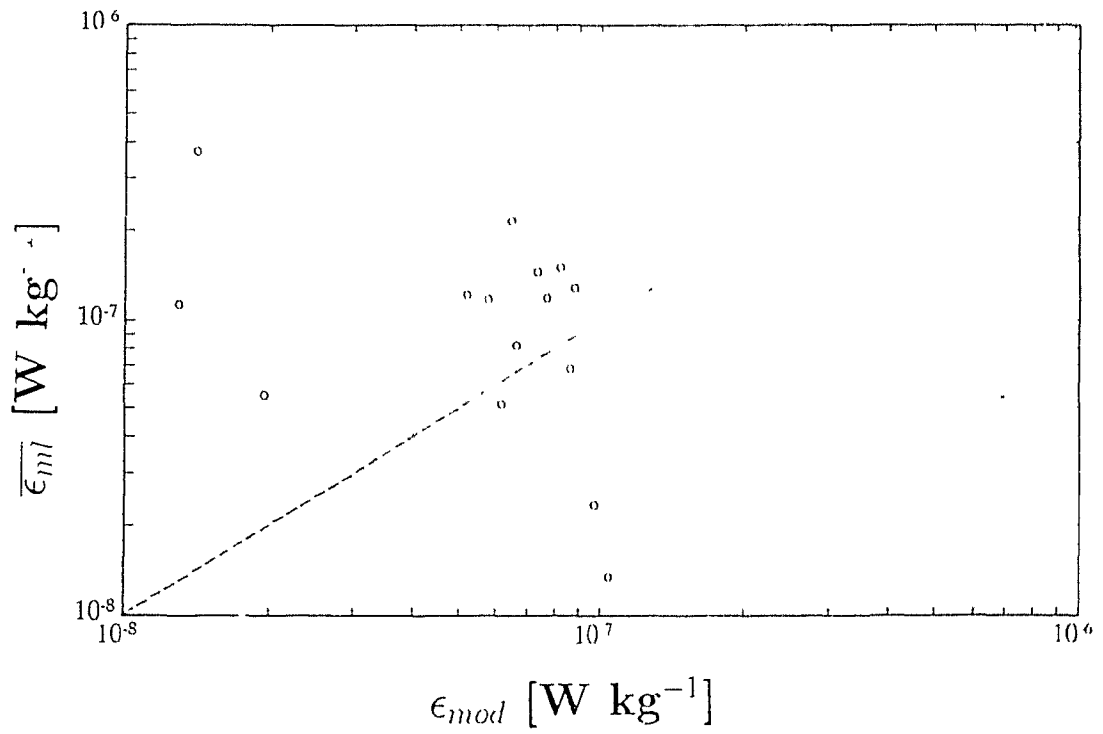


Figure 3.6: Dissipation modelled using similarity scaling and measured mixed layer dissipation at the equator.

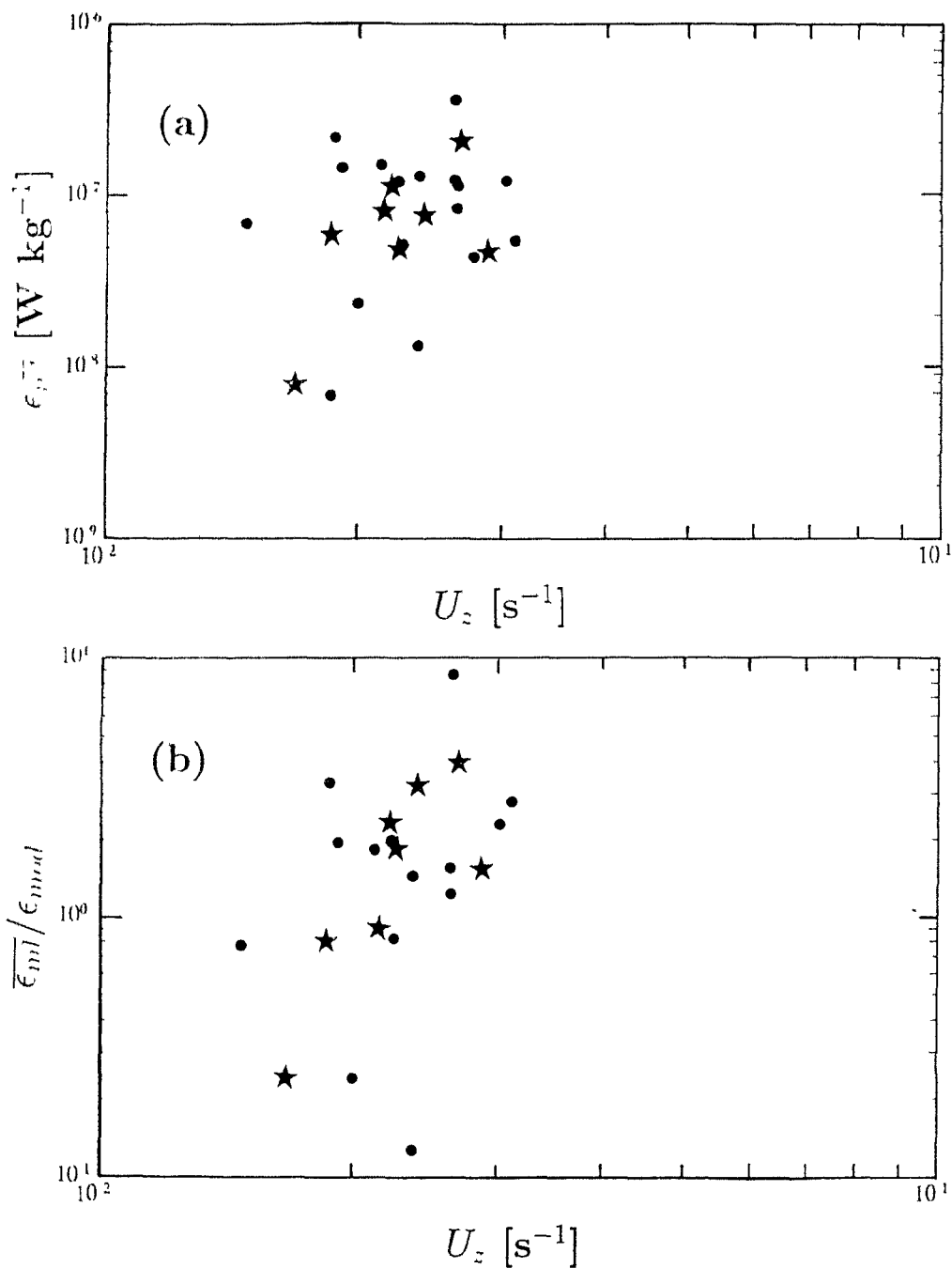


Figure 3.7: The shear,  $U_z$ , between 14 and 22 m from the ADCP *versus* (a) the mixed layer dissipation,  $\epsilon_{ml}$  and (b) the ratio between observed and modelled mixed layer dissipation,  $\epsilon_{ml}/\epsilon_{mod}$ . The station values are the dots and the twelve-hour averages are the stars.

behind the weak diurnal cycle is verified here. It is a consequence of the low winds observed during the time series and of the strong incoming heat flux. The average wind stress for the 12-day time series studied by Moum *et al.* [1989] was  $0.1 \text{ N m}^{-2}$ , while our average was  $0.03 \text{ N m}^{-2}$ . This wind speed ( $5 \text{ m s}^{-1}$ ) is on the lower end of the range in wind speeds studied by Oakey and Elliott [1982] and Oakey [1985] as well. In the Tropic Heat 2 experiment [Hebert *et al.*, 1991a], carried out in the spring of 1987, there was no diurnal cycle in dissipation when the wind speeds were low. This is consistent with a weaker coupling of the surface forcing terms and dissipation under low wind conditions. In spring of 1988, the incoming heat flux was greater than in November 1984, reducing the depth of the mixed layer to less than 10 m on a daily basis. The weaker buoyancy flux at night limited the extent of mixing as well. The shallowness of the EUC core also contributed to the greater stability of the upper water column and placed the high shear region very close to the surface. It is to be expected that the influence of shear be greater for our cruise than in Tropic Heat 1; this has been shown to be the case.

### 3.4 The role of turbulent fluxes in the large-scale balances of the equatorial Pacific

#### 3.4.1 Turbulent stress in the zonal momentum balance

Turbulent dissipation has been proposed to play a major role in the vertical distribution of momentum in the equatorial Pacific, where the Coriolis force is zero [Crawford, 1982, Bryden and Brady, 1985, Wacongne, 1989, Bryden and Brady, 1989]. However, comparison between the different terms of the momentum balance with observations of turbulent stress from microstructure measurements [Peters *et al.*, 1988, Dillon *et al.*, 1989, Hebert *et al.*, 1991b] have revealed that the balance is not simple. Consequently, Dillon *et al.* [1989] and Hebert *et al.*

[1991b] suggest that high frequency internal waves may be instrumental in the downward transport of momentum. In this section, the measurements of turbulent stress for our four and a half day equatorial time series are presented and the turbulent stress divergence is compared to the annual mean value of the other terms of the momentum balance, following Dillon *et al.* [1989]. The zonal momentum balance at the equator is given by:

$$\frac{\partial u}{\partial t} + u \frac{\partial u}{\partial x} + v \frac{\partial u}{\partial y} + w \frac{\partial u}{\partial z} + \frac{\partial \overline{U'U'}}{\partial x} + \frac{\partial \overline{U'V'}}{\partial y} + \frac{1}{\rho} \frac{\partial P}{\partial x} = \frac{1}{\rho} \frac{\partial \tau^x}{\partial z} \quad (3.7)$$

where  $P$  is the pressure and  $u$  and  $v$  are the zonal and meridional velocities, averaged over an appropriate time and length scale (many days to years, thousands of km),  $U'$  and  $V'$  are the velocity fluctuations over time and length scales shorter than the 'mean' and greater than turbulence (Reynold's decomposition). The terms on the left hand side are the local acceleration ( $\partial u/\partial t$ ), zonal ( $u \partial u/\partial x$ ), meridional ( $v \partial u/\partial y$ ) and vertical ( $w \partial u/\partial z$ ) advection, the eddy flux divergence ( $\partial \overline{U'U'}/\partial x + \partial \overline{U'V'}/\partial y$ ) and the zonal pressure gradient ( $1/\rho \partial P/\partial x$ ). On the right hand side, the turbulent stress divergence term ( $1/\rho \partial \tau^x/\partial z$ ) includes only the vertical component because the horizontal gradients are assumed to be much smaller than in the vertical [Dillon *et al.*, 1989, Hebert *et al.*, 1991b]. The vertical friction term is given by the zonal wind stress at the surface and within the water column, by the turbulent stress from Eq. (3.6). In a steady state the local acceleration term is zero; Hebert *et al.* [1991b] found that it is usually much smaller than the other terms even for time periods as small as 15 days.

According to linear theory [Sverdrup, 1947], the zonal wind stress in the equatorial region is balanced by the vertically integrated zonal pressure gradient ( $1/\rho \int \partial P/\partial x dz$ ), while the other terms serve to redistribute momentum vertically [Bryden and Brady, 1985, McPhaden and Taft, 1988]. This balance appears to hold for long-term (annual, and sometime seasonal) averages [Tsuchiya, 1979, Mangum and Hayes, 1984, McPhaden and Taft, 1988] but does not for shorter time scales, where high frequency events can obscure the long-term values [Mangum and Hayes, 1984, McPhaden and Taft, 1988, Hebert *et al.*, 1991b]. Bryden

and Brady [1985, 1989] used data from several years to quantify the different terms of the momentum balance. They computed an estimate of the turbulent stress divergence as the residual of subtracting their estimates of zonal pressure gradient and eddy flux divergence from the averaged advective accelerations. The resulting vertical friction term has a depth scale of 200 m and implies a vertical diffusivity of  $O(10^{-3})$   $\text{m}^2\text{s}^{-1}$ .

Dillon *et al.* [1989] estimated the turbulent stress divergence using the time series measurements made in November 1984 during Tropic Heat 1. They found that the turbulent stress decreased exponentially from the surface wind stress with a length scale of order 20 m. The turbulent stress was larger than needed to close the annual balance above 30 m and below that depth it was too small. The depth scale of the zonal pressure gradient is 100 to 140 m [Mangum and Hayes, 1984, McPhaden and Taft, 1988, Bryden and Brady, 1989]. This is much larger than the observed length scale of the turbulent stress term and the two terms cannot be expected to balance [Dillon *et al.*, 1989]. Dillon *et al.* [1989] discuss the uncertainties of the microstructure measurements and dissipation method and conclude that there must exist another mechanism for transporting momentum downward, such as internal waves.

The data from Tropic Heat 2 (April 1987) were also used to address the zonal momentum balance [Hebert *et al.*, 1991b]. The oceanographic conditions during this cruise were very different to those of Tropic Heat 1, as were the magnitude and vertical distribution of the turbulent stress divergence. Turbulent friction fell off linearly from the surface wind stress value and the integrated turbulent stress divergence term was much smaller than required for the annual balance. Hebert *et al.* [1991b] insist on the need for more measurements of turbulent dissipation throughout the annual cycle to provide an estimate of the long-term average. They also evaluate each of the terms of Eq. (3.7) over a variety of time scales, ranging from the long-term annual mean of Bryden and Brady [1985, 1989] to the 4- to 15-day ship-board observations during their zonal transect and concurrent mooring data. The terms of the momentum

balance were shown to vary significantly over short time and space scales, as well as to respond to longer time-scale processes (ENSO). This variability was associated with changes in the slope and intensity of the EUC. The turbulent stress divergence term appeared to depend solely on the wind stress variability. They found that high-frequency internal waves were observed only during periods of high winds.

The vertical structure of the turbulent stress term,  $\tau^x(z)$  from Eq. (3.6) during our equatorial time series (Figure 3.8) was quite different from previously published observations [Peters *et al.*, 1988, Dillon *et al.*, 1989, Hebert *et al.*, 1991b] where it falls off rapidly from the maximum value found close to the surface. For our data, the maximum value of turbulent stress within the water column is observed at 55 m. The vertical distribution of the shear (Figure 2.15) was similar to that observed during Tropic Heat 1, except that the EUC core was shallower during our experiment. However, as indicated in Chapter 2, the vertical profile of the eddy diffusivity for momentum (Figure 2.18) was different from previous measurements, with very large values at depth. The contour plot (Figure 3.9) of turbulent stress throughout the time series indicates that although the deep maximum is not always present and that its depth varies, it was observed for most of the time series (18 of the 24 equatorial stations).

The turbulent stress divergence (Figure 3.10) was obtained from the average turbulent stress profile. The effect of vertical friction is decelerating for most of the water column except for the high shear zone above the EUC core where it is positive with a maximum value of  $5 \cdot 10^{-7} \text{ m s}^{-2}$  at 50 m. This vertical structure is very different from either of the Tropic Heat experiments, nor does it conform to what is expected from large-scale balances [Bryden and Brady, 1989, Wacongne, 1989].

To place our observations in the context of the zonal momentum balance, analysis is carried out as in Dillon *et al.* [1989]. The water column is divided into two sections: from 0 to 30 m and from 30 to 60 m (since we have no data below 70 m). Eq. (3.7) is then integrated and rearranged:

$$\frac{\tau^x(a)}{\rho} - \frac{\tau^x(b)}{\rho} = \int_a^b \left\{ -\frac{1}{\rho} \frac{\partial P}{\partial x} - u \frac{\partial u}{\partial x} - w \frac{\partial u}{\partial z} - \frac{\partial \overline{U'U'}}{\partial x} - \frac{\partial \overline{U'V'}}{\partial y} \right\} dz \quad (3.8)$$

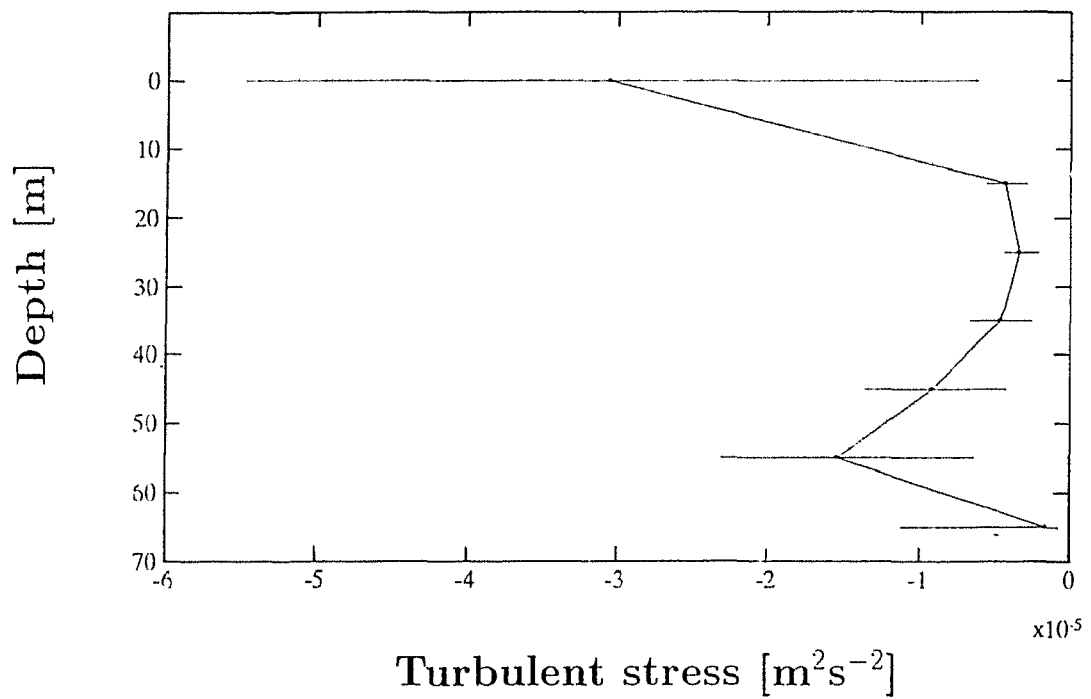


Figure 3.8: Turbulent stress at the equator. The solid line (and circles) is the mean and the error bars are the 95% confidence intervals, estimated using the bootstrap method. The surface value is the zonal wind stress.

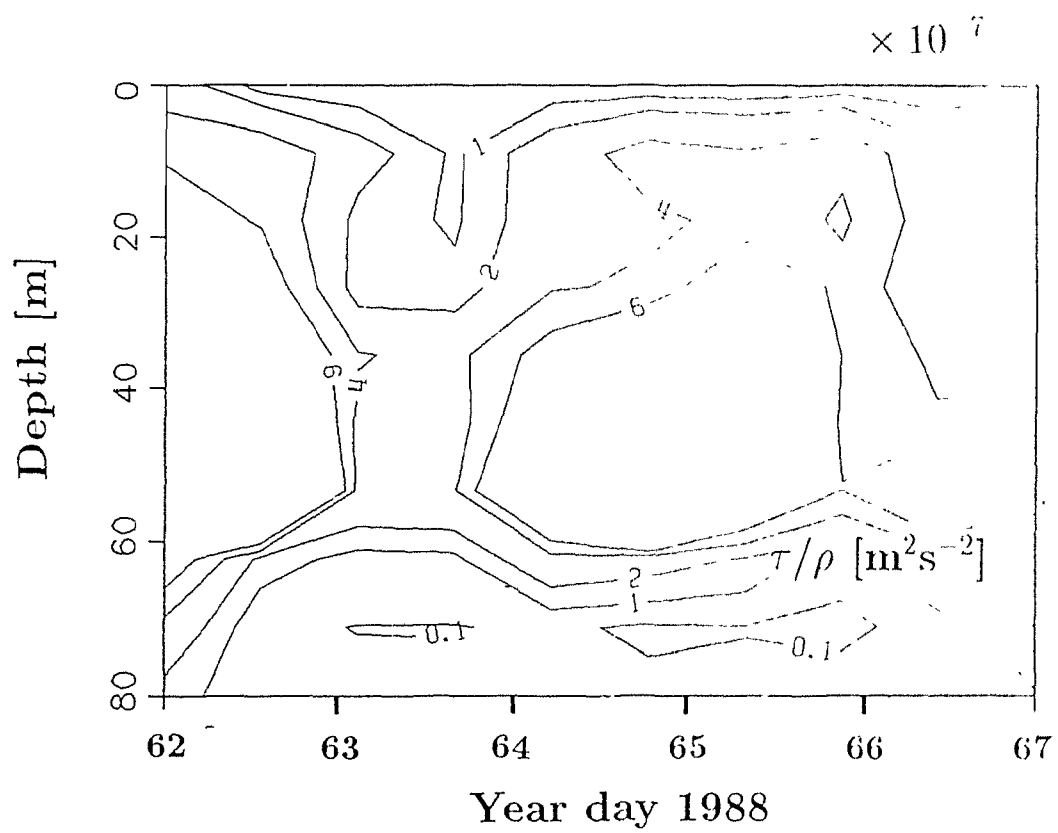


Figure 3.9: Contour plot of the time series of turbulent stress.

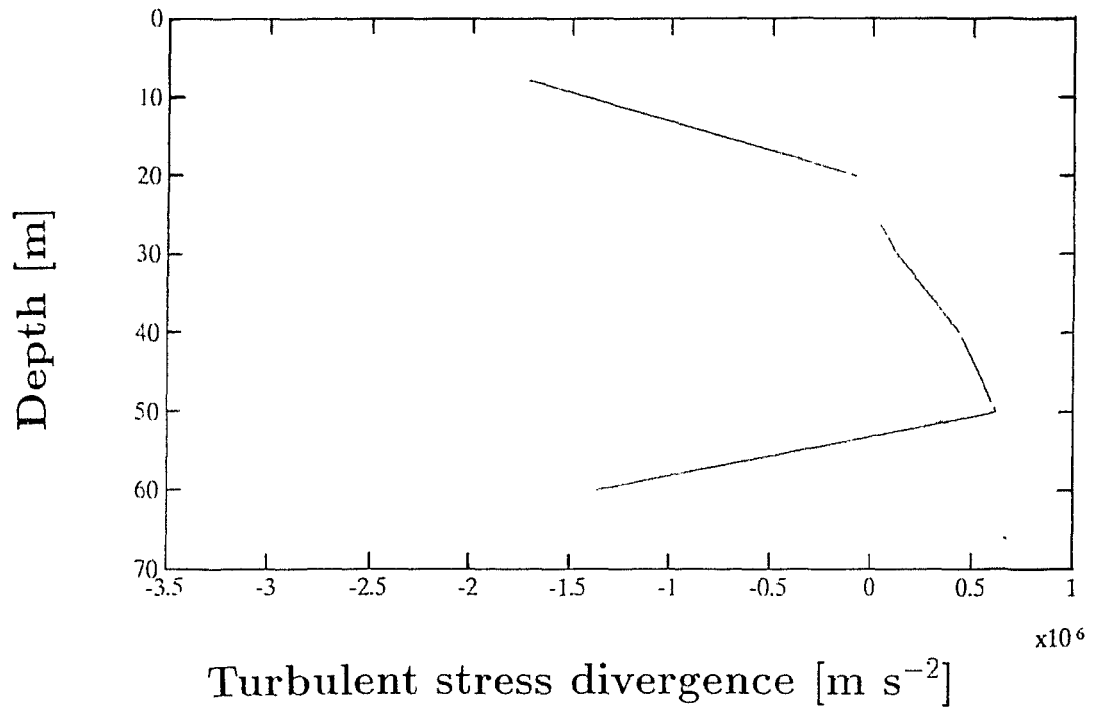


Figure 3.10: Turbulent stress divergence for the equatorial time series, obtained from the mean profile.

where  $a$  and  $b$  are the upper and lower limits of integration respectively (0 and 30, 30 and 60 and 0 and 60). The sum of all the terms on the right-hand side (the long term mean) is defined as  $LTM$  and as in Dillon *et al.* [1989], Eq. (3.8) is rearranged introducing a residual to account for the uncertainties and neglected terms:

$$LTM + \frac{\Delta\tau^x}{\rho} = R \quad (3.9)$$

where  $\Delta\tau^x/\rho$  is the difference between the turbulent stress at the top and bottom of the layer in question (the left hand side of Eq. (3.8)) and  $R$  is the residual. The annual mean values of Bryden and Brady [1985, 1989] (taken from Dillon *et al.* [1989]) are compared with our turbulent stress observations. The results are shown in Table 3.4, together with the turbulent stress values from the Tropic Heat 1 experiment.

Between 0 and 60 m, the turbulent stress term is comparable to the sum of the terms on the left hand side of Eq. (3.8). The large decelerating effect of the turbulent stress in the top 30 m is compensated in part by the positive turbulent stress divergence above the EUC core (Figure 3.10). The residual is compared with the zonal pressure gradient (ZPG), the most important term of the  $LTM$ : for the top 30 m, the residual is somewhat larger than the ZPG and opposes it. For 30 to 60 m, our residual is almost twice the size of the ZPG and of the same sign, *i.e.* opposing the wind stress and accelerating the eastward flow. For the entire range from 0 to 60 m, the residual is -19% of the zonal pressure gradient. This is very different from the results of Dillon *et al.* [1989] who found that the residual was -25% of the ZPG between 30 and 60 m but that above this depth, the turbulent stress term was excessively large (from 0 to 30 m, 514% of the ZPG). The agreement between the turbulent friction term and the  $LTM$  for the top 60 m is probably fortuitous: comparison is made between annual means and a very short time series. Likewise, the full vertical range of the zonal pressure gradient is not resolved with our data set.

It is interesting to note that the vertical distribution of turbulent stress was markedly different from previously published results. The present observations may be representative of boreal spring, and as such, contribute to the understanding of the seasonal variability. The Tropic Heat 2 data set is also from the spring, but the

Table 3.4: The momentum budget for the top 60 m. Units are  $10^{-6} \text{ m}^2 \text{ s}^{-1}$ . The terms of Eq. (3.8):  $\int -(1/\rho \partial P/\partial x)dz$ ,  $-\int (u \partial u/\partial x)dz$ ,  $-\int (w \partial w/\partial z)dz$ ,  $-\int (\partial \overline{U'U'}/\partial x) - (\partial \overline{U'V'}/\partial y)dz$  and turbulent stress from Tropic Heat 1 (TH1) taken from Dillon *et al.* [1989], data for the annual averages from Bryden and Brady [1985, 1989]. The sum of the terms on the right hand side is given by  $LTM$ , and should be comparable to the difference between the stress at the top,  $a$ , and at the bottom,  $b$  of the layer in question ( $\Delta\tau^x/\rho$ ). Our turbulent stress measurements (WEC) are on the last three lines.

	DEPTH RANGE		
	0-30	30-60	0-60
$ZPG = -\int (1/\rho \partial P/\partial x)dz$	14	12	26
$-\int (u \partial u/\partial x)dz$	-0.9	-0.6	-1.5
$-\int (w \partial w/\partial z)dz$	5	6	11
$-\int (\partial \overline{U'U'}/\partial x + \partial \overline{U'V'}/\partial y)dz$	-9	-6	-15
$LTM$	9	11	20
$(\Delta\tau^x/\rho)_{TH1}$ $(\tau^x(a)/\rho; \tau^x(b)/\rho)$	-82 (-100;-18)	-14 (-18; -4)	-96 (-100; -4)
$(\Delta\tau^x/\rho)_{WEC}$ $(\tau^x(a)/\rho; \tau^x(b)/\rho)$	-26 (-30; -4)	11 (-4;-15)	-15 (-30;-15)
<b>Residual:</b> $R = LTM + \Delta\tau^x/\rho$	-17	22	5
$R/ZPG$	-121%	183%	-19%

oceanographic conditions were atypical because it was the end of the 1986-1987 El Niño [Hebert *et al.*, 1991b]. Large-scale conditions in March 1988 were typical for the season [McPhaden and Taft, 1988] as were the cruise conditions (see Chapter 2). The discrepancy between our measurements of turbulent momentum flux and the results of Tropic Heat 1 and 2 may be due to the seasonal variability of large-scale conditions, both oceanographic and meteorological. The agreement between the annual mean of the large-scale terms of the momentum balance and the turbulent stress divergence seems to indicate that the latter may be a significant component in the zonal balance in the spring, even if not throughout the year.

### **3.4.2 Diurnal variation of sea-surface temperature: the roles of turbulent mixing and penetrative irradiance**

The turbulent diffusion of heat may also play an important role in the heat balance of the equatorial region. Niiler and Stevenson [1982] did an annual mean heat budget for the tropical Pacific warm-water pool enclosed by the 27° isotherm. By integrating throughout the volume of the pool, the advective heat flux becomes zero. They found that the net surface heating is balanced by the turbulent flux of heat into the thermocline. In a one-dimensional analysis of the mixed layer heat budget, Imawaki *et al.* [1988] were able to reproduce the time series of turbulent heat flux from the difference between the surface fluxes and the change in heat content from the mooring at 140°W. This balance is based on the difference between night-time and day-time fluxes and relies on the assumption that the advective flux of heat changes over periods longer than the diurnal.

An additional loss term for the upper layer is the penetrative irradiance. This is the visible light which has not been absorbed and penetrates beyond the base of the surface layer, and is thus a heat loss for that layer. Lewis *et al.* [1990] found that the penetrative irradiance exiting the mixed layer of the western equatorial Pacific was of the same magnitude as the climatological net surface heat flux, implying that little heat was absorbed in this layer. At 110°W, Hayes *et al.* [1991] used mooring

data to study the variability of sea-surface temperature between 1986 and 1988. They concluded that the changes in sea-surface temperature were controlled primarily by one-dimensional processes: net incoming heat flux and the losses due to turbulent mixing and penetrative irradiance at the base of the mixed layer. Zonal advection contributed to the heat flux variability, but the fluctuations of the two were poorly correlated. Meridional advection was associated with the presence of instability waves and may be an important source of intra-seasonal variability. Meridional diffusion had an important role in seasonal heating and was crucial to balance the budget in the winter period.

During the Tropic Heat 1 experiment, the turbulent heat flux at the base of the mixed layer was comparable to the net surface heat flux into the ocean [Gregg *et al.*, 1985, Peters *et al.*, 1988, Moum *et al.*, 1989]. A simple one-dimensional analysis for the top 20 m [Moum *et al.*, 1989] revealed that the turbulent heat flux at that depth was 70% of the surface heat flux. Penetrative irradiance was not large: at 20 m, only  $19 \text{ W m}^{-2}$  were lost to the mixed layer in the form of light [Moum *et al.*, 1989]. The similarity between the surface fluxes and the turbulent heat flux at the base of the mixed layer indicate that the advective transport of heat may be important in determining the changes in heat content of this layer [Moum *et al.*, 1989]. Conversely, variability in the turbulent heat flux, or in the penetrative irradiance, may lead to large changes in sea surface temperature (Chapter 5).

Here an attempt is made to model the diurnal variability in sea-surface temperature as a balance between one-dimensional fluxes: the incoming heat flux at the surface and the losses at depth due to turbulent mixing and penetrative irradiance. This is then compared with the observed change in heat content of the surface layer.

The time series for each of these terms is shown in Figure 3.11. The surface layer was defined as 15 m deep, this is within the mixed layer for most of the time series, and at the top of the diurnal thermocline during the day-time shallow mixed layers (Figure 3.1). This depth was chosen because the temporal pattern in heat content (Figure 3.11a) mirrored the observed changes in surface temperature (Figure 2.10),

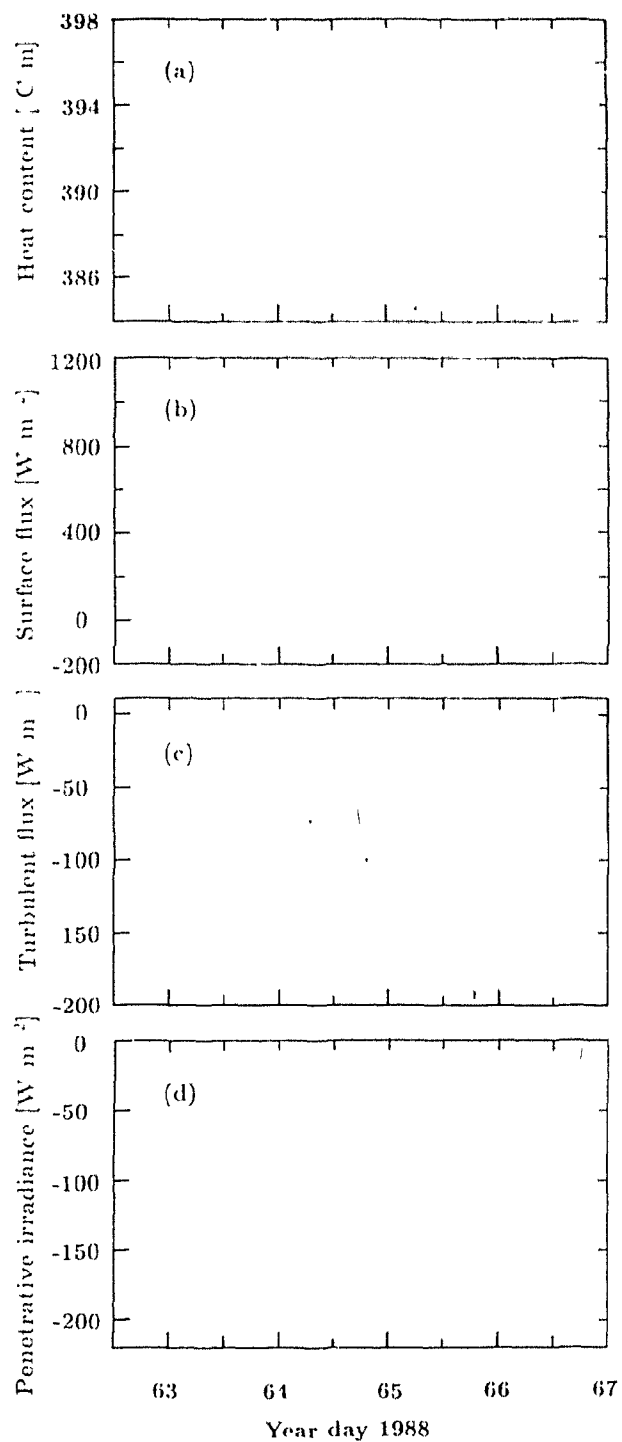


Figure 3.11: Time series of the terms of the one-dimensional heat flux: heat content (a), net surface heat flux (b), turbulent heat flux at 15 m (c) and penetrative irradiance at 15 m (d).

notably the diurnal cycle and the sharp cooling after year day 65. The net incoming heat flux (Figure 3.11b) was very large during the day, due to high solar irradiance values and low heat losses due to latent, sensible and long-wave heat fluxes.

At the base of the layer, the turbulent heat flux (Figure 3.11c) was intermittent: with values ranging from +2 (upward) to  $-196 \text{ W m}^{-2}$ . Although the night-time values of turbulent heat flux were generally greater than those of the previous day (except for day 64), there is not a strong diurnal cycle in turbulent heat flux as in the Tropic Heat 1 experiment [Imawaki *et al.*, 1988, Moum *et al.*, 1989]. The trend is of increasing heat flux with time. The mean for the time series was  $-40 \text{ W m}^{-2}$ . The penetrative irradiance (Figure 3.11d) was estimated using the incoming visible light just below the surface and the attenuation coefficient,  $K_2$ , of  $0.067 \text{ m}^{-1}$ . This value was the average attenuation coefficient for the top 20 m estimated at noon on the five days. The maximum noon-time irradiant heat loss was around  $-210 \text{ W m}^{-2}$ , and the average was  $-80 \text{ W m}^{-2}$ . Although the maximum values of the two loss terms are comparable, the on-off diurnal periodicity of the penetrative irradiance contrasts with the intermittent turbulent diffusion term.

To compare the terms of the one-dimensional balance, we have averaged them over twelve hour periods (0600–1800 and 1800–0600). The predicted heating rate for the layer is the difference between the incoming heat at the surface and the losses at depth. This is then compared to the observed heating, given by the change in heat content over the twelve hour period. The net incoming heat flux (Figure 3.12a) is around  $800 \text{ W m}^{-2}$ , during the day and less than  $-200 \text{ W m}^{-2}$  at night, with very little variability from day to day. The total heat loss at depth (Figure 3.12b) shows a strong diurnal cycle and the loss at night (due to turbulent mixing) increases with time. The predicted heating rate (Figure 3.12c) for the surface layer shows a strong diurnal periodicity, with a trend of decreasing day-time heating with time.

The observed heating (Figure 3.12d) was much more variable: the day-time heating rate for 63 and 64 was minimal and the night-time cooling was very large. The

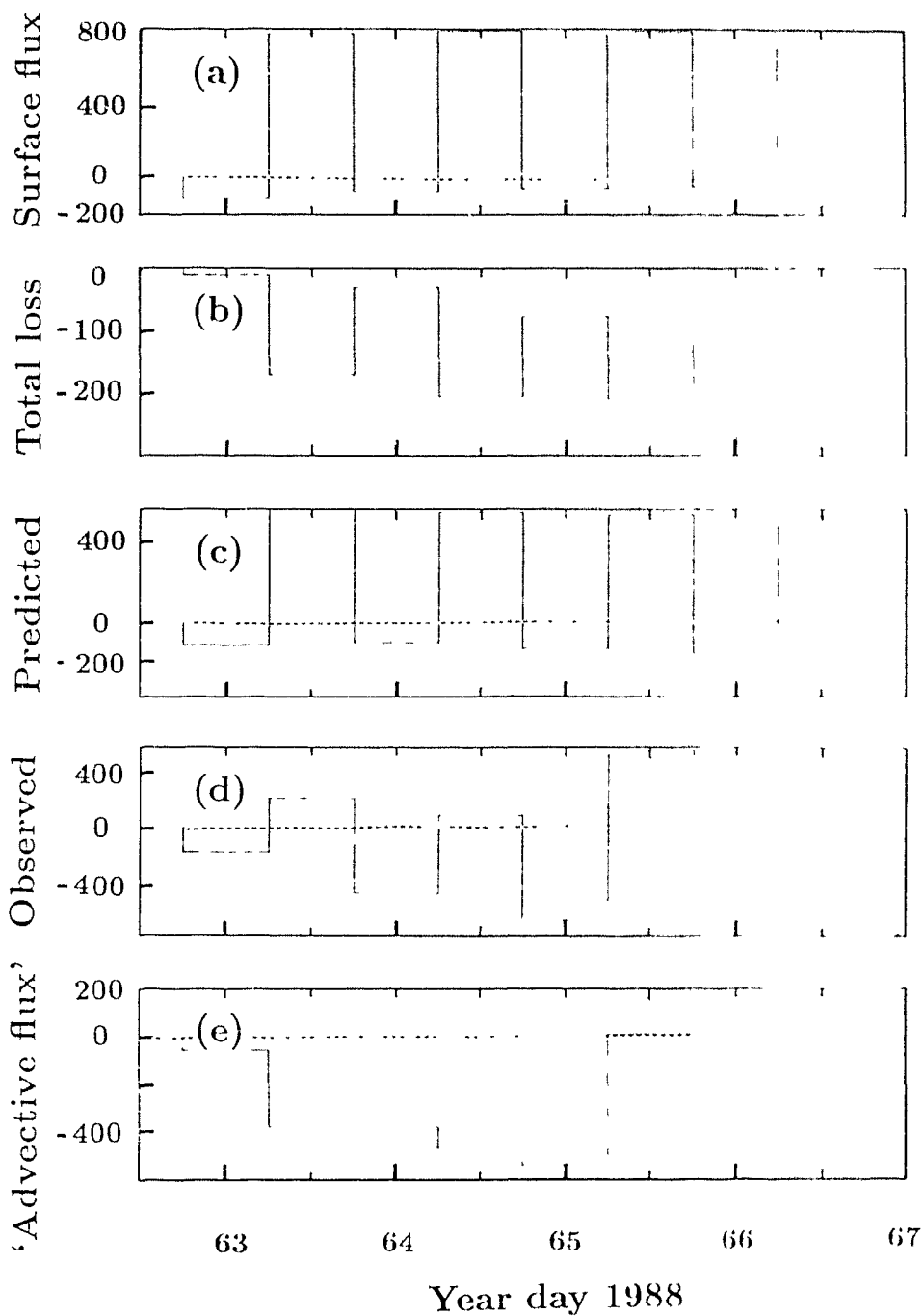


Figure 3.12: Heat budget for the surface layer during the time series. Twelve-hour averages of incoming heat flux (a), total heat losses at 15 m (b) and predicted heating rate (c), observed heating rate (d) and the 'advective' residual (e).

difference between the observed and predicted heating rates is presented in Figure 3.12e. This difference is within the error of the various terms for the night of year day 62 and after 65. The greater cooling observed between year day 63 and the night between days 64 and 65 cannot be explained by the concurrent one-dimensional heat fluxes. It is proposed that the discrepancy is due to advective transport [Imawaki *et al.*, 1988, Moum *et al.*, 1989]. This is the same event commented on in section 2.4.2. It is concluded in that section that the most likely cause of such a rapid change in upper water column properties results from the meridional transport of the 'displaced' zonal current system to  $0^\circ$ .

## 3.5 Discussion

### 3.5.1 Spatial and temporal variability in the equatorial region

#### Equatorial maximum in dissipation

The detailed sampling carried out in the Tropic Heat program allowed close examination of variability in the equatorial region. Dissipation varies on a wide range of temporal scales, from the inter-annual (ENSO) to the diurnal [Moum *et al.*, 1989, Peters *et al.*, 1989, Hebert *et al.*, 1991b]. The 12-day time series studied by Moum *et al.* [1989] showed that wave-like motions with periods ranging from 4 to 21 days modulate the higher frequency (diurnal) variability. Likewise, short time scale variations in the buoyancy flux and wind speed also introduce variability [Hebert *et al.*, 1991a]. Extensive averaging may be needed to distinguish the spatial pattern. The vertical structure of dissipation is also important to understand the meridional variability, and distinguishing between the dissipation in the mixed layer and thermocline has been illustrative [Peters *et al.*, 1989, Hebert *et al.*, 1991a]. The latitudinal pattern of dissipation in the mixed layer can be obscured by the increase in mixed layer depth poleward of  $0^\circ$  [Peters *et al.*, 1989]. Both Peters *et al.* [1989] and Hebert *et al.* [1991b]

found that thermocline dissipation was maximum in the equatorial region.

The meridional pattern of dissipation of TKE and thermal variance was examined here by comparing the values at each depth bin along the transect. Because mixed layer depth changes considerably with latitude (Figure 3.1), this approach implies comparison between mixed layer and thermocline values. Peters *et al.* [1989] integrated  $\epsilon$  with depth and separated the mixed layer and thermocline values. Hebert *et al.* [1991a] studied the average dissipation in the mixed layer and thermocline. Their observations of a maximum in thermocline dissipation at  $0^\circ$  are consistent with the present result of a larger peak at depth. The decision to compare each depth bin rather than integrated or averaged values, was to better distinguish the vertical structure of the mixing regime at each site. For example, the high values observed at  $10^\circ\text{N}$  are confined to the upper part of the mixed layer as corresponds to direct surface forcing, and the high  $\epsilon$  and  $\chi$  measurements at  $0^\circ$  extend throughout the top 60 m (Figure 2.8). In fact the highest values are observed below 40 m. The averaged or integrated values of  $\epsilon$  or  $\chi$  over the top 70 m reveal the same characteristic peak. Although 70 m was the lowest depth sampled at the equator, off-equatorial dissipation values below that depth were less than  $10^{-8} \text{ W kg}^{-1}$ .

The meridional structure was clearly visible in the present data set (Figures 2.8 and 3.2). The larger dissipation rates associated with the equatorial region were statistically significant, even when considering the bias introduced by insufficient sampling away from  $0^\circ$ . The maximum was related to the presence of the EUC as well as to the meridional flow, which can be decisive in bringing  $Ri$  to critical values. Spatial variability was not so clear for Tropic Heat 1: Peters *et al.* [1989] found that the mean value at  $1.5^\circ\text{N}$  and S was smaller than the confidence limits of the equatorial data set, using the same null hypotheses and methods as used here. Large temporal variability in the equatorial region obscures the meridional structure, as in the case of Tropic Heat 1 [Peters *et al.*, 1989, Moum *et al.*, 1989, Hebert *et al.*, 1991a]. The weaker diurnal variability during our sampling period no doubt contributed to the visualization of the maximum. The weak variability associated with the diurnal cycle

is proposed here to be a direct result of the seasonal meteorological and hydrographic conditions (Chapter 2). From these observations, one would expect the equatorial maximum in dissipation to be more clearly visible in the spring.

### Temporal variability

Perhaps the most interesting result of Tropic Heat 1 was the extreme diurnal cycle in dissipation. In the present study, the classical diurnal cycle in  $\epsilon$  (maximum night-time values) was limited to the top bin (10–20 m) (Figures 2.16 and 2.17). The proposed explanation is in the less vigorous energy input due to winds or convective buoyancy flux, as well as the significantly shallower EUC core, which led to large stratification close to the surface, thus impeding convective surface-driven mixing. A modelling study [Schudlich and Price, 1991] that discussed the sensitivity of the diurnal cycle to various factors, found that if the core of the EUC was shallower, night-time mixing would not penetrate below the core. This is consistent with the present observations and confirms the role of the EUC depth in controlling the extent of nocturnal mixing.

The strong diurnal heating also enhanced stratification during the day, reducing the mixed layer to less than 10 m on a daily basis. Hebert *et al.* [1991b] found that for periods of low wind speeds, there was no diurnal cycle in dissipation. During our time series, the low values of the night-time buoyancy flux were a consequence of the low wind speeds, the air-sea temperature difference and relative humidity. Thus, the lack of large diurnal changes in dissipation, is not an anomaly from the ‘basic state’ as observed in Tropic Heat 1, but rather the two may be manifestations of the seasonal variability of the region. Our observations are probably the norm for spring conditions of low winds, shallow intense EUC, large incoming irradiance values and low surface heat losses.

Attempts to parameterize the dissipation rates with surface forcing confirm the above conclusions. The buoyancy flux was important in determining the depth of the mixed layer, but was not correlated to the observed  $\bar{\epsilon}_{ml}$  for either the latitude or twelve-hour averages (Tables 3.3 and 3.1). The relationship between wind and

dissipation was poor throughout the transect, both on an individual station basis and for the daily and latitude averages (Tables 3.1, 3.3 and Figures 3.3, 3.5). Although the energy dissipated in the mixed layer was approximately 1% of the wind energy flux at 10 m, the temporal patterns are not comparable (Figure 3.5). For a given wind speed, the mixed layer (and thermocline) dissipation was greater at the equator (Figures 3.3). The poor relationship between wind and energy dissipation is a consequence of the low wind speeds observed for most of the cruise. At  $0^\circ$ , the average wind speed was  $5 \text{ m s}^{-1}$ , at the lower end of the range of wind speeds studied by Oakey and Elliott [1982] and Oakey [1985].

In Tropic Heat 1, dissipation was higher than predicted by scaling with the surface forcing [Moum *et al.*, 1989] and the excess was attributed to shear production [Peters *et al.*, 1989]. In the present data, as well, surface forcing alone was not sufficient to explain the dissipation in the mixed layer at  $0^\circ$ . Dissipation was modelled using similarity scaling [Lombardo and Gregg, 1989] and, as reported by Peters *et al.* [1989], the modelled dissipation was smaller than the observations and the two were poorly correlated (Figure 3.4a and Table 3.3). Away from the equator, the mixed layer dissipation was smaller than modelled and for the latitude averages, the two were related (Figure 3.4b and Table 3.1).

The twelve-hour average value of mixed layer dissipation was best explained by the shear between 14 and 22 m (Table 3.3). This was also the case for the 12 day time series studied by Moum *et al.* [1989]. Likewise, the ratio between observed and modelled dissipation was highly correlated to the shear (Figure 3.7 and Table 3.3) as observed by Peters *et al.* [1989]. This indicates that the excess dissipation is associated with shear production. Because of the weak coupling between surface forcing and dissipation values at  $0^\circ$ , *i.e.* the lack of large diurnal changes to great depth, and the shallowness of the EUC, we expect the dissipation to be less clearly related to wind and buoyancy flux, and more related to shear than in Tropic Heat 1. This is seen to be the case.

The time series at the equator was characterized by a decrease in SST and increase

in salinity on year day 64 (Figure 2.11). This coincides with a shift from southward to northward velocities below 50 m depth and intensification of the EUC (Figure 2.11). It is possible that we sampled the shift from the southward to northward phase of a 20-day oscillation, but longer velocity time series or satellite images of SST during that period would be necessary to corroborate this option. It is proposed that the EUC was centered south of  $0^\circ$  when we commenced the time series. We then sampled a change from south to northward velocity which returned the zonal current system to the equator.

A simple one-dimensional model of the processes controlling the diurnal temperature signal of the surface layer was applied. It was found that for a 15 m deep surface layer, the mean penetrative irradiance was twice the turbulent heat flux. The predicted rate of heating, obtained by subtracting the losses at depth from the incoming heat at the surface, was in agreement with the observed heating for two and a half days (Figure 3.12). On year day 63 and 64, the intense cooling event could not be accounted for by one-dimensional processes.

The agreement between the predicted and observed heating rates for the upper layer in a region with such large advective fluxes is unexpected. However, it does conform to the observations of other authors [Peters *et al.*, 1988, Moum *et al.*, 1989, Hayes *et al.*, 1991]. The similarity between the incoming heat flux at the surface and the losses at depth observed during Tropic Heat 1 indicates that the heat content is determined by the advective transport [Moum *et al.*, 1989]. In our observations in March, the incoming heat was greater than the losses at depth. Since the one-dimensional heat fluxes appear to be in close balance with the changes in upper kayer heat content, small changes in any of the vertical or horizontal flux terms could lead to very large changes in the surface temperature. This was the case for our short time series, where a sharp cooling event took place in response to enhanced advective transport.

### 3.5.2 The role of turbulent mixing in the large-scale momentum balance

In the absence of Coriolis force at  $0^\circ$ , turbulent stress divergence has been proposed as a significant term in the energy balance of the zonal current system [Crawford, 1982, Gregg *et al.*, 1985, Bryden and Brady, 1989]. Recent measurements seem to indicate however that the length scale of decay is smaller than necessary to balance the zonal pressure gradient [Dillon *et al.*, 1989].

The wind stress imposed at the surface is transported downwards by turbulent mixing. The vertical friction opposes the zonal pressure gradient, decelerating the eastward flowing EUC. Previous measurements of microstructure have revealed that the balance between the zonal pressure gradient and the turbulent stress divergence is not simple. For Tropic Heat 1, the decay scale of the turbulent flux of momentum was much shorter than that of the zonal pressure gradient [Peters *et al.*, 1988, Dillon *et al.*, 1989]. The turbulent stress divergence was too small at all depths in Tropic Heat 2 [Hebert *et al.*, 1991b].

In our time series, the vertical distribution of turbulent stress was different from previously published observations (Figure 3.10). Instead of decreasing with depth from maximum values just below the sea surface, a maximum was observed at 55 m. Because of this deep maximum, the turbulent stress divergence becomes positive, reinforcing the zonal pressure gradient and accelerating the eastward flow.

The sum of the annual mean terms of the zonal momentum balance of Bryden and Brady [1985, 1989] was close to the observed integrated stress divergence between 0 and 60 m (Table 3.4). This agreement is a consequence of the vertical structure of turbulent stress (the low wind stress at the surface and the high values of diffusivity at depth). The similarity in magnitude of the vertical friction term and the remaining terms of the balance meant that the residual was only -19% of the zonal pressure gradient.

The shortness of the time series and the limited depth range sampled render questionable any agreement with an annual average. However, the vertical structure of

the turbulent stress may be typical for spring conditions. The agreement does support the hypothesis that vertical friction may play an important role in the downward transport of momentum on a seasonal basis.

### 3.6 Summary

1. The equatorial maximum in turbulent energy dissipation found in the previous chapter was further tested to take into account the limitations of sampling. The 95% confidence intervals of the equatorial maximum between  $1^{\circ}\text{S}$  and  $0^{\circ}$  were distinct from the the uncertainty associated with the low sampling frequency and insufficient sampling of the diurnal cycle away from  $0^{\circ}$
2. The dissipation rates of the upper water column were poorly correlated with either the local wind speeds or the night-time buoyancy flux independently. Similarity scaling was used to model the mixed layer dissipation with the surface forcing terms. The observed dissipation values were larger than modelled at  $0^{\circ}$  and smaller off the equator. Although observed and modelled dissipation were poorly related for the equatorial time series, the two were weakly correlated for the latitude averages.
4. The ratio of observed to modelled dissipation for the daily averages at  $0^{\circ}$  was highly correlated to the shear between 14 and 22 m. The average mixed layer dissipation was also highly correlated to the shear.
5. The weak surface forcing terms and upper water column structure result in a shallow diurnal cycle. The poor coupling between air-sea fluxes and mixed layer dissipation results from the seasonal conditions: low wind speeds, high air temperature and cool SST and a shallow intense EUC. Thus, the absence of deep mixing at night is probably typical for the season, rather than a deviation from the 'basic state' observed in Tropic Heat 1.

6. At  $0^\circ$ , the role of vertical friction in the annual mean budget of momentum was assessed. The average turbulent stress was maximum at 55 m. This deep maximum was observed in 18 of the 24 stations. The maximum in turbulent stress at depth led to an acceleration of  $5 \cdot 10^{-7} \text{ m s}^{-2}$  above the EUC core.

The annual mean values for the terms of the zonal momentum balance [Bryden and Brady, 1985, Bryden and Brady, 1989, Dillon *et al.* 1989] between 0 and 60 m were compared with the turbulent stress term. The residual of balancing the annual mean and the turbulent stress was only -19% of the zonal pressure gradient. This agreement is probably fortuitous as we are comparing a long-term annual mean with the average of a four and a half day time series, and have only resolved part of the relevant depth range (0-200 m). However, the different vertical structure of the turbulent stress term may be typical for boreal spring, and the agreement indicates that perhaps turbulent friction plays a role in the downward transport of momentum on a seasonal basis.

8. The heat content of the upper layer was explained within the uncertainty of the terms by one-dimensional fluxes for two-and-a-half days of the equatorial time series. The heat loss at the base of the 15 m layer was due to turbulent transport and to penetrative irradiance. The latter was, on the mean, twice as large as the turbulent heat flux at that depth. The one-dimensional fluxes of heat cannot account for the sharp cooling observed on year days 64 and 65. It is attributed to advective transport, probably associated with the observed intensification of the EUC.



# Chapter 4

## A physical estimate of new production

### 4.1 Introduction

New production is defined as the primary production that results from nutrients that have been ‘newly’ introduced into the euphotic or sunlit layer (as opposed to recycled nutrients from within the layer) [Dugdale and Goering, 1967, Eppley and Peterson, 1979]. The major source of new nutrients to the euphotic zone in the laterally homogeneous open ocean is the influx of deep water through upwelling and transport due to turbulent mixing [Eppley *et al.*, 1979].

New production can be estimated by measuring the amount of labelled nitrate that is incorporated into particles [Dugdale and Goering, 1967], by using sediment traps to quantify the particle flux out of the euphotic layer, or by estimating the flux of nitrate into the euphotic zone. The turbulent supply of nitrate has been inferred from microstructure measurements of dissipation by Lewis *et al.* [1986] for the oligotrophic Atlantic subtropical gyre and by Crawford [Crawford and Dewey, 1989] for the continental shelf of British Columbia. In the case of Lewis *et al.* [1986] direct comparison to nitrate uptake rates was made and agreement found within the respective measurement errors. Hamilton *et al.* [1989] explored the role of nitrate

transport associated with salt finger fluxes for the same data set.

This chapter will discuss the supply of nitrate to the euphotic zone in the equatorial region through turbulent diffusion and through the balance between upwelling and meridional divergence. In the vicinity of  $0^\circ$ , advective flow will be the major mechanism of nitrate supply. Away from the equator, where the upwelling velocities are very small or negligible and the neighboring surface waters are equally nutrient starved, the main source of nitrate will be that due to turbulent fluxes. In this section, estimates of the physical rate of supply are compared with two concurrent measurements of biological consumption: incorporation of  $^{15}\text{N}$ -labelled nitrate into particles [Wilkerson and Dugdale, 1991] and the rate of nitrate utilization [Eppley and Renger, 1991] to provide an approximate nitrate budget for the equatorial region.

## 4.2 Material and methods

The nitrate supply to the illuminated upper layer (euphotic zone) will be explored in this section. The base of this layer is defined by the depth at which the visible irradiance (400–700 nm) is 1% of the surface value. This is the criterion used by Wilkerson and Dugdale [1991] and was adopted here to enable comparison between their measurements and the physical supply.

### 4.2.1 Turbulent nitrate flux

The turbulent flux of nitrate at the base of the euphotic zone was calculated assuming gradient transport, using the eddy diffusivity for mass,  $K_\rho$  (Eq. (2.7)) and the gradient in nitrate concentration at that depth.

$$J_{NO_3} = -K_\rho \frac{\partial[NO_3]}{\partial z}. \quad (4.1)$$

where the square brackets denote concentration. The 95% confidence intervals (denoted as 95% C.I.) for  $K_\rho$  and the turbulent nitrate flux were estimated using the bootstrap method [Efron and Gong, 1983].

## 4.2.2 Simple advective box model

An advective balance between upwelling and the north-south transport was carried out for meridional boxes going between 1°S and 1°N, 5°S and 5°N and 10°S and 10°N. The zonal (east-west) circulation, albeit very strong, is not taken into account, because we have no data away from 150°W. Neglecting the zonal flow is justified when estimating the upwelling velocity because of the small value of the zonal divergence ( $\partial u/\partial x < 10^{-7} \text{ s}^{-1}$ , while  $\partial v/\partial y \simeq 5 \cdot 10^{-7} \text{ s}^{-1}$ ) in the upper 70 m of the water column [Bryden and Brady, 1989]; it leads to an underestimate of upwelling velocity of around 17%.

Absolute velocities are needed for the advective balance. The ADCP data presented in Chapter 2 was re-analysed to obtain an average velocity profile for each side of the meridional boxes. The meridional (north-south) shear profiles from ADCP (Chapter 2) at each latitude were averaged to provide a latitude mean and then integrated to obtain the velocity relative to the ship at each depth bin. This was done to avoid spurious effects associated with the arbitrary reference level of 14 m used previously. The level of no motion was found by assuming that the depth-integrated north-south transport over the sampled depth range (top 150 m) was zero. Other levels of no motion were tested and rejected. The criteria used to choose the level of no motion were: (a) that the velocities be ‘reasonable’ according to classical circulation pictures and available literature values; and (b) that the net heat transport estimates obtained from using these velocities be comparable to the measured surface heat flux and to other heat flux divergence values from the literature. The assumption of null north-south transport over the top 150 m is consistent with the zero upwelling velocity at around that depth as reported by Bryden and Brady [1985], Brady and Bryden [1987] and Hurlin and Freitag [1987].

A ‘population’ of 1000 meridional velocity profiles was obtained from the mean profile at each latitude by adding a random velocity error in the range of  $\pm 0.05 \text{ m s}^{-1}$  to each depth interval of the latitude velocity profile. This population of velocity estimates was then used to calculate the upwelling velocity from continuity and the

divergence of heat and nitrate (net balance of nitrate/heat supply and export). Given the average velocity for each box side (70 m deep, the depth of the euphotic layer) and the equation of two-dimensional continuity, the upwelling velocity for the meridional ‘box’ is

$$w = H \frac{\Delta v}{L} \quad (4.2)$$

where  $w$  is the vertical velocity and  $v$  is the flow leaving (entering) the region,  $H$  is the depth and  $L$  the length of the ‘box’.

The advective supply at the bottom of the box (upwelling) and loss (at the northern and southern boundaries of the box) of nitrate and heat are given by

$$\text{NITRATE SUPPLY} = w_i [NO_3]_B \quad [\text{mmol m}^{-2} \text{ s}^{-1}] \quad (4.3)$$

$$\text{HEAT SUPPLY} = \rho C_p w T_B \quad [\text{W m}^{-2}] \quad (4.4)$$

$$\text{NITRATE LOSS} = \int_{EL} \left( \frac{v_N [NO_3]_N}{L} - \frac{v_S [NO_3]_S}{L} \right) dz \quad (4.5)$$

$$\text{HEAT LOSS} = \rho C_p \int_{EL} \left( \frac{v_N T_N}{L} - \frac{v_S T_S}{L} \right) dz \quad (4.6)$$

where  $EL$  is the integration domain (over the euphotic layer), the subscripts  $S$ ,  $N$  and  $B$  denote the nitrate concentration or temperature at the southern, northern and bottom sides of the box respectively and  $v_N$ ,  $v_S$  are the meridional velocities at the northern and southern sides of the box. A cartoon of the advective box model is shown in Figure 4.1. The ‘population’ of 1000 velocity estimates and the corresponding distributions of  $w$  and of the fluxes of heat and nitrate enable us to find a mean and confidence intervals (95% C.I.) associated with the assumed 0.05 m s<sup>-1</sup> error in velocity. The balance in nitrate or heat transport is given by the upwelled input of nitrate/heat from the bottom minus the loss from the sides.

### 4.2.3 Estimates of biological consumption of nitrate

Data from fellow scientists on the WEC88 cruise were used to compare the physical supply estimates with two measures of biological uptake rates,

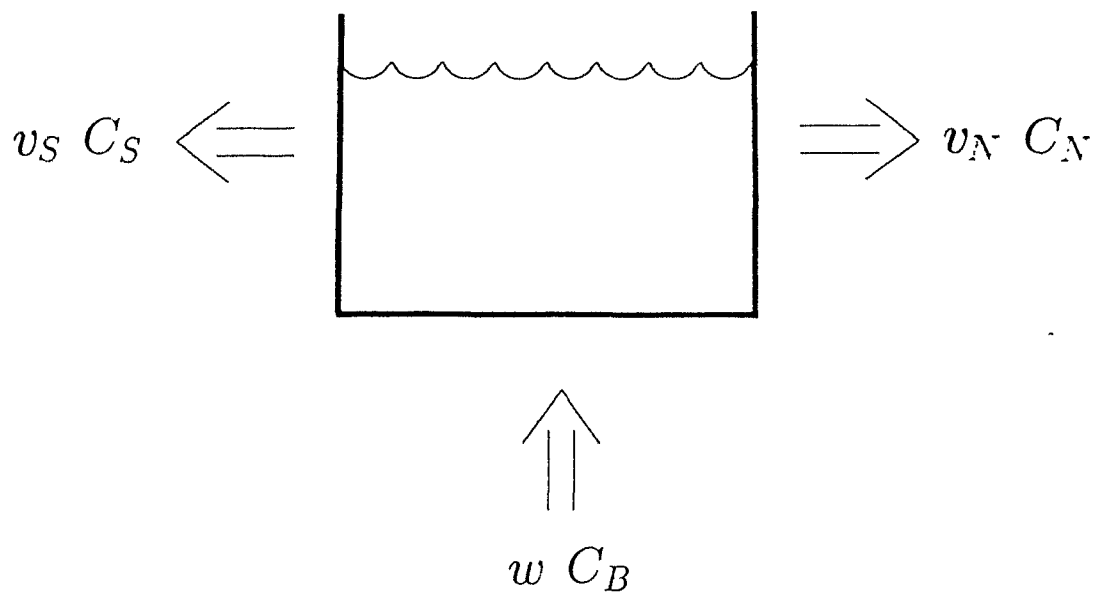


Figure 4.1: Cartoon of the two-dimensional advective box model. The advective supply of a scalar,  $C$ , is a balance between the upwelling at the base of the box and the meridional loss from the sides.  $C$  denotes both temperature and nitrate concentration. The subscripts  $B$ ,  $N$ ,  $S$  denote the mean scalar value for the bottom, northern and southern boundaries of the box respectively.

those made using  $^{15}\text{N}$ -labelled nitrate uptake [Wilkerson and Dugdale, 1991] and using the chemiluminescent method to determine changes in nitrate concentration [Eppley and Renger, 1991]. The incorporation of  $^{15}\text{N}$ -labelled nitrate into particles was measured in six hour incubations [Dugdale *et al.*, 1991, Wilkerson and Dugdale, 1991]. The hourly rates given in Wilkerson and Dugdale [1991] were multiplied by twelve to obtain a daily value, following their assumption of no nitrate uptake at night [Dugdale *et al.*, 1991].

The other measure of biological consumption was made with the chemiluminescent method. This measures the nitrate concentration of the sample before and after incubation [Eppley and Renger, 1991]. Incubations were for twelve hours between  $2^\circ\text{N}$  and  $3^\circ\text{S}$  and for twenty-four hours elsewhere. The rate of nitrate disappearance in the incubations was integrated for the depth intervals available (always within the euphotic zone) and the hourly rates were multiplied by twenty-four for the daily value, because of the large night-time disappearance rates observed [Eppley and Renger, 1991].

## 4.3 Results

### 4.3.1 Turbulent nitrate supply and measured biological uptake rates

The turbulent nitrate flux into the upper layer depends on the gradient in nitrate concentration and the vertical diffusivity at the base of the euphotic zone. High nitrate concentrations ( $> 5 \text{ mmol m}^{-3}$ ) are observed in the surface waters of the equatorial region (Figure 2.5). The nitracline shoals around  $8\text{--}10^\circ\text{N}$  and in the equatorial region and deepens south of  $0^\circ$ . The gradient in nitrate concentration (Figure 4.2a) is quite large (of order  $10^{-1} \text{ mmol m}^{-4}$ ) within  $2^\circ$  of the equator, with maxima at  $1^\circ\text{S}$  and  $1^\circ\text{N}$ . These high values are found in the equatorial region because of the large nitrate concentrations in the upper water column. The gradient is larger at  $1^\circ\text{N}$  and  $1^\circ\text{S}$  than at  $0^\circ$  because there is very little difference in nitrate concentration in

the surface waters at  $0^\circ$ . Poleward of  $5^\circ\text{S}$ , the gradient becomes very small as the nitracline deepens (Figures 2.5, 4.2a). There is a maximum at  $10^\circ\text{N}$  associated with the shallow nitracline found there. Maximum values of vertical diffusivity,  $K_\rho$ , at the base of the euphotic zone are observed at  $0^\circ$ , falling sharply at  $1^\circ\text{N}$  and  $2^\circ\text{S}$  (Figure 4.2b). Poleward of the equatorial region, the values are very low, more so to the north (around  $5 \cdot 10^{-7} \text{ m}^2 \text{ s}^{-1}$ ) than to the south (around  $5 \cdot 10^{-6} \text{ m}^2 \text{ s}^{-1}$ ).

The meridional pattern of the turbulent supply of nitrate (Figure 4.3) is similar to that of diffusivity and accentuated by the nitrate gradient. For reference, the turbulent rate of nitrate supply found in the subtropical Atlantic gyre [Lewis *et al.*, 1986],  $0.14 \text{ mmol m}^{-2} \text{ day}^{-1}$ , is also shown. In the equatorial region ( $0^\circ$ – $1^\circ\text{S}$ ) nitrate supply is maximum ( $1$ – $3 \text{ mmol m}^{-2} \text{ day}^{-1}$ ) and elsewhere it is very small ( $< 10^{-2} \text{ mmol m}^{-2} \text{ day}^{-1}$ ).

Comparison is made between the turbulent rate of supply of nitrate and two measures of nitrate consumption: the incorporation of  $^{15}\text{N}$ -labelled nitrate into particles [Wilkerson and Dugdale, 1991] and the rate of disappearance of nitrate from the chemiluminescent method [Eppley and Renger, 1991]. The incorporation of  $^{15}\text{N}$ -labelled nitrate into particles is maximum in the equatorial region and at  $1^\circ\text{N}$  although the meridional variability is not as large as in the case of the turbulent diffusion. For the region between  $6^\circ\text{N}$  and  $6^\circ\text{S}$ , the rate of nitrate disappearance was very large; in the equatorial region it was about seven times the measured rates of  $^{15}\text{N}$  uptake [Eppley and Renger, 1991, Wilkerson and Dugdale, 1991]. Disappearance was consistently larger than turbulent supply except at  $1^\circ\text{S}$ .

Because of the large advective transport in this region [Chavez and Barber, 1987], turbulent mixing of nitrate is not a good estimator of nitrate supply. This is evident from Figure 4.3 where consumption and turbulent supply differ by two orders of magnitude. Nitrate is also supplied to the surface waters through the upwelling of cold, nutrient rich water at  $0^\circ$  which is then transported poleward. The advective supply is addressed in the following section.

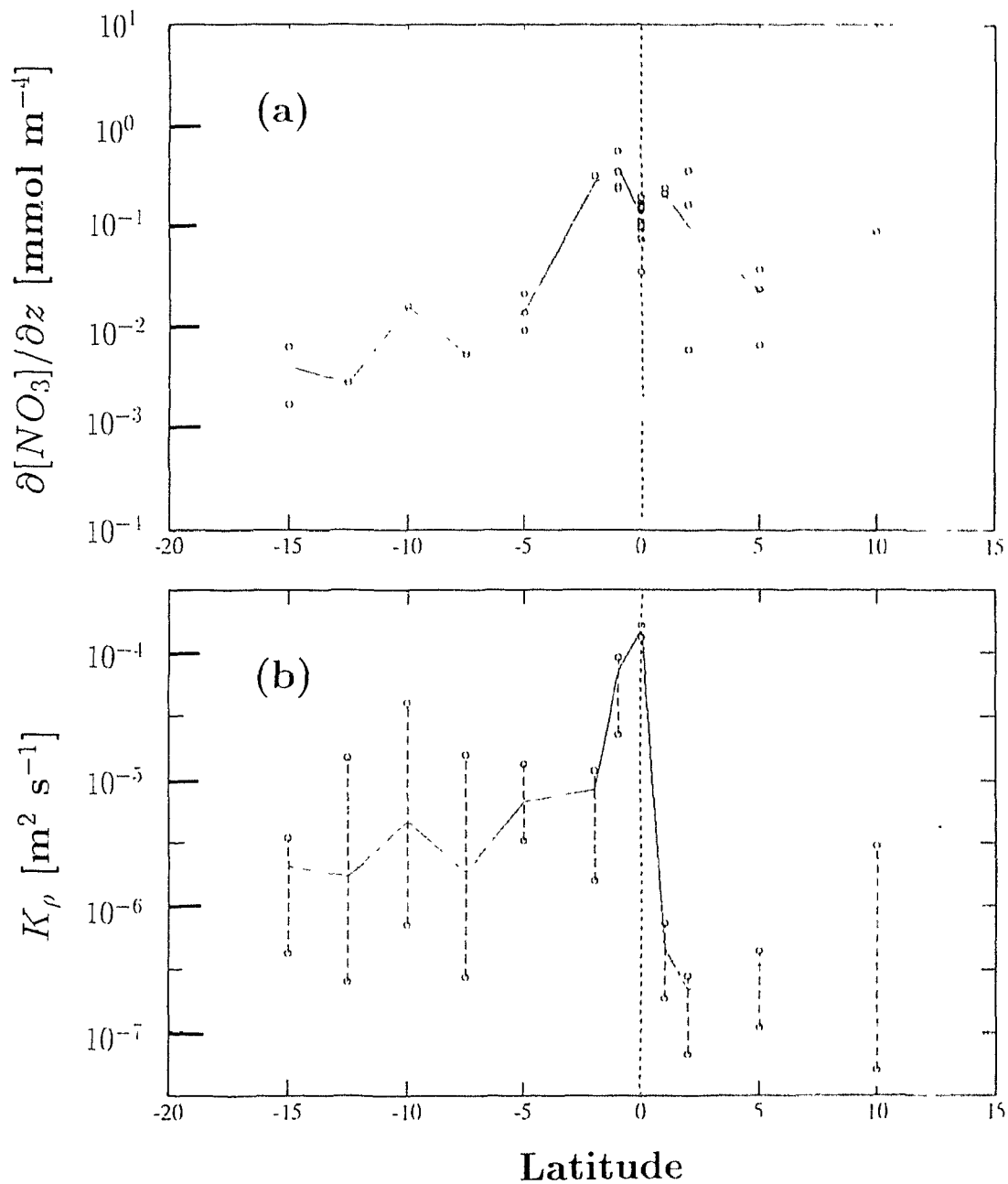


Figure 4.2: The nitrate concentration gradient at the base of the euphotic layer (a); the solid line is the mean gradient and the dots are the individual observations at each latitude. The vertical diffusivity,  $K_\rho$ , at the base of the euphotic zone (b); the error bars are the 95% confidence intervals calculated using the bootstrap method.

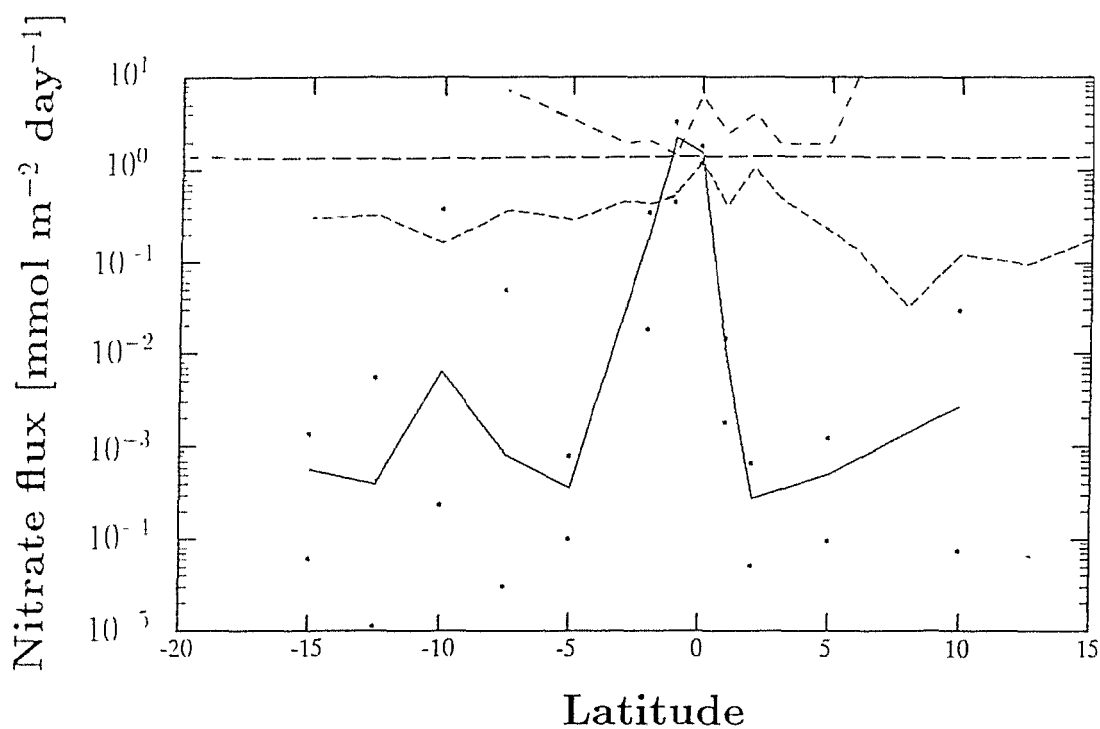


Figure 4.3: The turbulent rate of nitrate supply and the two measures of biological uptake. The solid line is the turbulent nitrate flux. The error bars are the 95% confidence intervals calculated using the bootstrap method. The dashed line is the rate of incorporation of nitrate into particles [Wilkerson and Dugdale, 1991]. The dash-dotted line is the rate of nitrate disappearance [Eppley and Renger, 1991].

### 4.3.2 Simple two-dimensional advective balance

The results of the advective balance are shown in Table 4.1 for each of the equatorial 'boxes'. The upwelling velocities obtained are consistent with literature values of  $w$  from both models and measurements. For  $1^{\circ}\text{N}$ – $1^{\circ}\text{S}$  we found the upwelling velocity to be  $1.3 \cdot 10^{-5} \text{ m s}^{-1}$  (95% C.I.:  $0.5$ – $2.1 \cdot 10^{-5} \text{ m s}^{-1}$ ); this is comparable to the result of a three-dimensional model for  $0.75^{\circ}\text{N}$ – $0.75^{\circ}\text{S}$  [Bryden and Brady, 1985] ( $2.5 \cdot 10^{-5} \text{ m s}^{-1}$ ) as well as to other estimates [Brady and Bryden, 1987, Halpern and Freitag, 1987]. The upwelling velocity obtained for  $5^{\circ}\text{N}$ – $5^{\circ}\text{S}$  is  $6.5 \cdot 10^{-6} \text{ m s}^{-1}$  (95% C.I.:  $4.8$ – $7.9 \cdot 10^{-6} \text{ m s}^{-1}$ ), which is similar to the results of Wyrтки [1981] who suggested a  $w$  of  $4 \cdot 10^{-6} \text{ m s}^{-1}$  for the region between  $5^{\circ}\text{N}$  and  $5^{\circ}\text{S}$ ,  $90^{\circ}$  and  $180^{\circ}\text{W}$ .

In general terms, the water leaving the box from the sides is warmer and has a lower nitrate content than the water entering the box at the bottom (Figure 4.1). This is the result of the upper water column processes: solar heating and biological nitrate consumption. When estimating the potential for new production, Chavez and Barber [1987] set an upper bound by ignoring the water leaving the box. Some of the upwelled nitrate is removed from the region by the diverging flow before the phytoplankton are able to take it up. For the region studied by Chavez and Barber [1987] approximately half of the upwelled nitrate is exported laterally, and their estimate of potential new production is consequently too large by a factor of two. Here, the difference between the upwelling and the meridional export of nitrate is presented as a more realistic estimate of the biological uptake. The uncertainties associated with this calculation can be evaluated by comparing the heat flux divergence with the measured surface heat fluxes and turbulent loss. Comparison can also be made with other studies of the heat budget of the region (see Discussion).

The two-dimensional heat divergence for the box going from  $1^{\circ}\text{N}$  to  $1^{\circ}\text{S}$  is  $206 \text{ W m}^{-2}$  (95% C.I.:  $53$ – $360 \text{ W m}^{-2}$ ) and for the box from  $5^{\circ}\text{N}$  to  $5^{\circ}\text{S}$ ,  $80 \text{ W m}^{-2}$  (95% C.I.:  $60$ – $100 \text{ W m}^{-2}$ ). The net heating between  $10^{\circ}\text{N}$  and  $10^{\circ}\text{S}$  is virtually zero. This suggests that the upwelling-divergence cell is closed in the meridional plane.

Table 4.1: The two-dimensional advective nitrate balance of the equatorial region. The nitrate change is the net supply of nitrate to the box in  $\text{mmol NO}_3 \text{ m}^{-2} \text{ day}^{-1}$ . In square brackets is the corresponding new production using the Redfield ratio of 6.6 carbon/1 nitrogen in  $\text{mg carbon m}^{-2} \text{ day}^{-1}$ . The heat change is the heating rate in the box in  $\text{W m}^{-2}$ .

BOX	w [ $\text{m s}^{-1}$ ]	NITRATE CHANGE [ $\text{mmol m}^{-2} \text{ s}^{-1}$ ]	HEAT CHANGE [ $\text{W m}^{-2}$ ]
<b>1°N–1°S</b>	$1.3 \cdot 10^{-5} \text{ m s}^{-1}$	4.25 [336]	206
95% C.I.	$(0.5\text{--}2.1 \cdot 10^{-5})$	(0.71– 7.9)	(53–360)
<b>5°N–5°S</b>	$6.5 \cdot 10^{-6} \text{ m s}^{-1}$	1.9 [150]	79
95% C.I.	$(4.8\text{--}7.9 \cdot 10^{-6})$	(1.38–2.28)	(57–100)
<b>10°N–10°S</b>	$-1.6 \cdot 10^{-6} \text{ m s}^{-1}$	-0.7 [-47]	-3
95% C.I.	$(-0.8\text{--} -2.5 \cdot 10^{-6})$	(-0.4 – -1.1)	(-14 – 9)

The water in the euphotic layer increases its temperature by solar heating and by the lateral influx of warm water. The loss of warm water through downwelling is comparable, in terms of heat flux, to the incoming surface heating in this region. The converging flow and downwelling between  $5^\circ$  and  $10^\circ$  inferred from the two-dimensional advective heat balance is also seen in satellite observations of sea surface temperature [P. Flament, personal communication, 1991].

The supply versus export of nitrate was also calculated for each meridional box (Table 4.1). Upwelling of cold, nutrient rich water introduces nitrate into the euphotic zone ( $12 \text{ mmol m}^{-2} \text{ day}^{-1}$  and  $3.4 \text{ mmol m}^{-2} \text{ day}^{-1}$  for the  $1^\circ\text{N}$ – $1^\circ\text{S}$  and  $5^\circ\text{N}$ – $5^\circ\text{S}$  boxes respectively), where it can be utilized by phytoplankters. Poleward advective transport occurs at the northern and southern sides of the box (a total of  $8 \text{ mmol m}^{-2} \text{ day}^{-1}$  for the  $1^\circ\text{N}$ – $1^\circ\text{S}$  box and  $1.5 \text{ mmol m}^{-2} \text{ day}^{-1}$  for  $5^\circ\text{N}$ – $5^\circ\text{S}$ ). This is a non-biological loss of nitrate to the region. If the predominant balance is between vertical input and lateral export, the net advective supply is a measure of the biological consumption. Nitrate is supplied to the euphotic layer within  $5^\circ\text{N}$  and  $5^\circ\text{S}$ . Between  $1^\circ\text{N}$  and  $1^\circ\text{S}$ ,  $4.2 \text{ mmol m}^{-2} \text{ day}^{-1}$  are consumed before the water flows poleward; between  $5^\circ\text{N}$  and  $5^\circ\text{S}$ , the supply is  $1.9 \text{ mmol m}^{-2} \text{ day}^{-1}$ . For the meridional box between  $10^\circ\text{N}$  and  $10^\circ\text{S}$  there is a net advective export of nitrate of  $0.7 \text{ mmol m}^{-2} \text{ day}^{-1}$ .

### 4.3.3 The nitrate budget for the equatorial region

By estimating the average values for each of the main terms of the nitrate balance for the previously defined meridional boxes, we can compare the relative contributions of each term. The rates of nitrate supply due to advective and turbulent transport and the loss terms as measured by biological uptake of  $^{15}\text{N}$ -labelled nitrate [Wilkerson and Dugdale, 1991] and the nitrate disappearance [Eppley and Renger, 1991] are given in Table 4.2 and Figure 4.4.

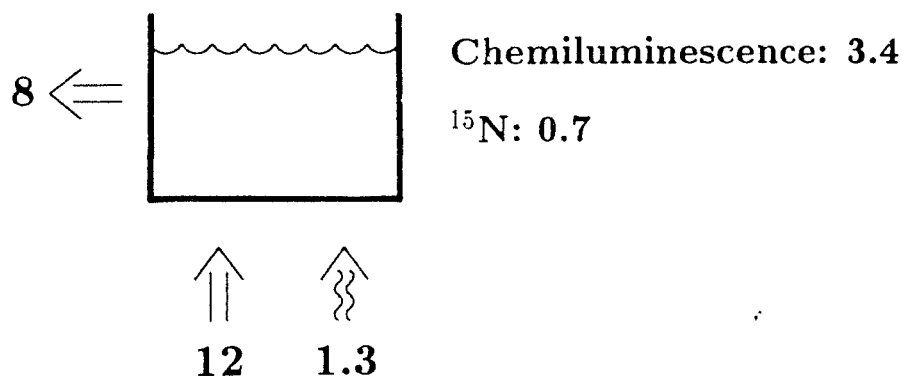
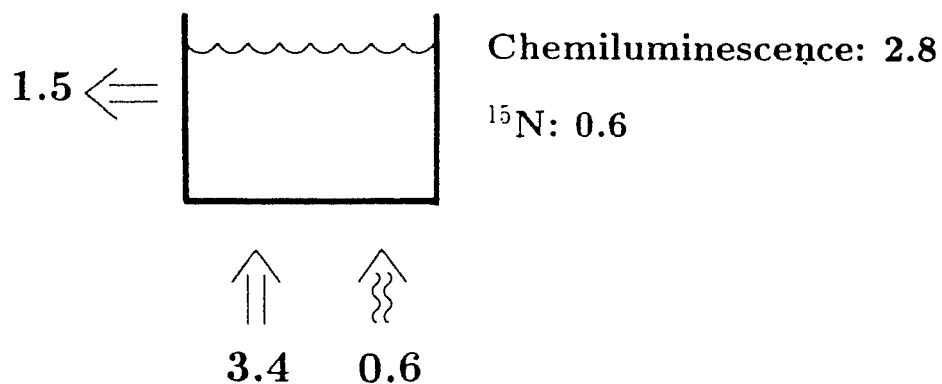
(a)  $1^{\circ}\text{N}-1^{\circ}\text{S}$ (b)  $5^{\circ}\text{N}-5^{\circ}\text{S}$ 

Figure 4.4: Nitrate budget for the meridional boxes. The wiggly lines represent turbulent fluxes, the straight lines advective. The vertical arrows are vertical transports, the horizontal ones represent the total lateral export. The budget for the box from  $1^{\circ}\text{N}$  to  $1^{\circ}\text{S}$  is shown in (a) and for the box going from  $5^{\circ}\text{N}$  to  $5^{\circ}\text{S}$  in (b).

Table 4.2: The nitrate budget of the equatorial Pacific. The biological consumption terms are the  $^{15}\text{N}$  uptake from Wilkerson and Dugdale [1991] and the rates of nitrate disappearance using the chemiluminescent method from Eppley and Renger [1991]. (The disappearance term when referring to the  $5^\circ\text{N}$ – $5^\circ\text{S}$  box actually only includes data from  $5^\circ\text{N}$ – $3^\circ\text{S}$ .) All values are given in  $\text{mmol NO}_3 \text{ m}^{-2} \text{ day}^{-1}$ .

BOX	ADV	TURB	PHYS. SUPPLY	$^{15}\text{N}$	CHEMIL.
<b><math>1^\circ\text{N}</math>–<math>1^\circ\text{S}</math></b>	4.25 $\left\{ \begin{array}{l} IN:12 \\ OUT:8 \end{array} \right.$	1.3	5.5	0.74	3.4
95% C.I.	(-0.05–8.4)	(0.5–1.7)	(0.45–10.14)		
<b><math>5^\circ\text{N}</math>–<math>5^\circ\text{S}</math></b>	1.91 $\left\{ \begin{array}{l} IN:3.4 \\ OUT:1.5 \end{array} \right.$	0.57	2.48	0.57	2.79
95% C.I.	(1.32–2.48)	(0.2–0.8)	(1.52–3.38)		

For a box restricted to  $1^\circ$  of the equator the main physical supply term is upwelling. Turbulent diffusion is 30% of the advective term, a significant contribution. The total physical supply is around  $5.5 \text{ mmol m}^{-2} \text{ day}^{-1}$  (95% C.I.: 0.45–10.14  $\text{mmol m}^{-2} \text{ day}^{-1}$ ). This is much larger than the biological consumption as measured using the  $^{15}\text{N}$  technique [Wilkerson and Dugdale, 1991]. Although the latter falls within the 95% confidence intervals of the estimate of physical supply, the  $^{15}\text{N}$ -labelled nitrate uptake is smaller than the uncertainty of this estimate at the 92% level (92% C.I.: 1.07–9.82  $\text{mmol m}^{-2} \text{ day}^{-1}$ ). The rate of nitrate disappearance [Eppley and Renger, 1991] is of the same order of magnitude as the total physical supply for this region.

For  $5^\circ\text{N}$ – $5^\circ\text{S}$  upwelling continues to prevail; the turbulent supply term is again 30%. As before, the total physical supply ( $2.48 \text{ mmol m}^{-2} \text{ day}^{-1}$ ; 95% C.I.: 1.52–3.28  $\text{mmol m}^{-2} \text{ day}^{-1}$ ) is larger than the measured incorporation of  $^{15}\text{N}$ -labelled nitrate into particles, even given the large uncertainty of the estimate of physical supply. The physical supply is similar in magnitude to the rate of nitrate disappearance.

## 4.4 Discussion

The primary source of new nutrients to the euphotic zone in most of the deep ocean is turbulent transport [Eppley *et al.*, 1979, King and Devol, 1979, Lewis *et al.*, 1986]. In the equatorial region, where upwelling is strong and persistent, the advective supply of nitrate is larger than the turbulent supply. Along the meridional transect, with the exception of the equatorial region ( $0^\circ$ – $2^\circ\text{S}$ ), the turbulent flux of nitrate was very small (less than  $10^{-2} \text{ mmol m}^{-2} \text{ s}^{-1}$ ). Very large values were observed at  $0^\circ$  and  $1^\circ\text{S}$  (1 to 3  $\text{mmol m}^{-2} \text{ day}^{-1}$ ).

Away from  $0^\circ$ – $2^\circ\text{S}$ , the measured vertical transport of nitrate was insufficient to account for the observed biological uptake (as measured by the incorporation of  $^{15}\text{N}$ -labelled nitrate [Wilkerson and Dugdale, 1991] or the rate of disappearance of nitrate [Eppley and Renger, 1991]). This is consistent with our understanding of

equatorial dynamics, where the meridional transport of nutrient-rich upwelled water is an additional source of nitrate.

However, in the low-nutrient waters poleward of the equatorial influence (approximately beyond  $7^\circ$ , see Figure 2.5), the major nitrate source is due to turbulent mixing across the nitracline. For this region, as in the oligotrophic Atlantic subtropical gyre [Lewis *et al.*, 1986], one expects an approximate balance between turbulent diffusion and biological uptake. Although the supply and consumption rates of nitrate were within the respective errors of determination for the Lewis *et al.* study [1986], the turbulent flux was six times smaller than the measured uptake of  $^{15}\text{N}$ -labelled nitrate. Hamilton *et al.* [1989] found that the nitrate fluxes estimated from a salt finger convection model are up to an order of magnitude greater than those resulting from a turbulent mixing model and the agreement with the measured nitrate uptake improved noticeably.

In our transect, even considering the uncertainty of the measurements of turbulent flux, the biological consumption terms are much larger. Poleward of  $2^\circ$ , each latitude was occupied usually for only 24 hours and sometimes only day-time microstructure measurements were made. Turbulence is highly intermittent and increased mixing rates are expected to occur associated with sporadic events (high winds, storms, breaking internal waves) or with nocturnal mixing [Shay and Gregg, 1984]. With our short sampling time at the higher latitudes of the transect, it is unlikely that we could adequately represent the local statistics. The present data set is made up of the average of a series of snapshots of the flux of nitrate at each latitude. The Lewis *et al.* [1986] measurement was a two-week mean of the nitrate flux across the thermocline (100–400 m depth), and was more likely to provide a reasonable estimate of the actual physical supply. The role of salt fingers is not likely to be important in the equatorial Pacific because the density ratio between the temperature and salinity gradients is larger than the critical value ( $R_\rho < 2$ ) favorable for salt finger formation (For the equatorial Pacific:  $4.5 \geq R_\rho \geq 2.9$ ).

To better estimate the physical supply of nitrate to the equatorial region, a simple

two-dimensional advective balance of nitrate and heat has been evaluated. This simple model is implemented using the data from our meridional transect and consequently is imperfect from several aspects: the data are not synoptic, sampling was limited to 150°W (no zonal component) and there are no absolute velocities.

- The lack of synopticity is the largest source of error. The nitrate concentration, temperature and velocities used for the northern and southern sides of the meridional box are at most 2-day averages at each site, which in turn were sampled eight days (for the 1°N–1°S box) to twenty three days (for the 10°N–10°S box) apart. Since the time-scales of variability of the region can be as short as 4 to 21 days [Wunsch and Gill, 1976, Chereskin *et al.*, 1986], I present these conclusions as an order of magnitude estimate. For a ‘true’ advective balance study it would be necessary to have mooring data (with temperature and nitrate) for two sites north and two south of 0° for time periods at least 60 days (preferably around 400 days [Bryden and Brady, 1989]), thus enabling measurement of both meridional and zonal components.
- The neglect of the zonal component is a result of our limited data, which are restricted to 150°W. Because the zonal divergence is small in the top 100 m [Bryden and Brady, 1989], we expect that the error associated with determining the upwelling velocity from the meridional divergence alone is not large (about 17%). The obtained upwelling velocities are consistent with other three-dimensional models [Wyrтки, 1981, Bryden and Brady, 1985] as well as with measurements [Brady and Bryden, 1987, Halpern and Freitag, 1987].

Although the east-west velocities ( $0.2 \text{ m s}^{-1}$ ) are larger than the meridional ones ( $0.05 \text{ m s}^{-1}$ ), the zonal gradients in temperature and nitrate concentration are smaller than in the meridional. The zonal flux of nitrate, using the gradient between 135°W [Peña *et al.*, 1990] and 150°W, is around  $9 \cdot 10^{-8} \text{ mmol m}^{-2} \text{ s}^{-1}$ , while the meridional flux is order  $5 \cdot 10^{-7} \text{ mmol m}^{-2} \text{ s}^{-1}$ . For heat, it is  $1.3 \cdot 10^{-7} \text{ °C m}^{-2} \text{ s}^{-1}$  in the zonal and  $5 \cdot 10^{-7} \text{ °C m}^{-2} \text{ s}^{-1}$  in the meridional. The larger

meridional contribution supports the assumption that the advective supply of nitrate is determined mainly by the balance between upwelling and meridional flow.

- Another source of error is the lack of absolute velocity measurements. So as to have a better understanding of the variability of the velocity field, a ‘population’ of velocity estimates was estimated by adding a random error to each depth interval of the mean velocity profile. The confidence intervals thus obtained are very large because the error value used,  $0.05 \text{ m s}^{-1}$ , is of the same magnitude as the observed speeds. The resulting uncertainty in the divergence of heat and nitrate is greatest for  $1^{\circ}\text{N}$ – $1^{\circ}\text{S}$  because the small size of the box makes it more sensitive to the uncertainty in velocity magnitude. The level of no motion was found by assuming that there was no integrated transport over the sampled range. If, for example, a 21-day wave were passing [Cherchkin *et al.*, 1986] and there were a net north or southward velocity at both edges of the meridional box, the conclusions would be erroneous. However, the inferred advective pattern conforms in sign and magnitude with the classical circulation pattern so the resulting advective balance is likely a good estimator of the ‘mean’.

An independent check on the results from the two-dimensional model can be made by comparing the estimates of heat transport divergence with heating rates from the surface heat flux and the outgoing turbulent heat flux at the base of the euphotic layer. The heating rate of a given layer, in a one-dimensional balance (see section 3.4.2) is given by the difference between the net incoming heat flux at the surface and the heat losses at the base of the layer.

For the region between  $1^{\circ}\text{N}$  and  $1^{\circ}\text{S}$ , the average net surface heat flux was  $210 \text{ W m}^{-2}$ . The loss at the base of the euphotic layer was due principally to turbulent mixing; the penetrative irradiance at this depth [Lewis *et al.*, 1990] is negligible. The mean turbulent heat flux at 70 m between  $1^{\circ}\text{N}$  and  $1^{\circ}\text{S}$  is  $60 \text{ W m}^{-2}$ , leading to a net heating of  $150 \text{ W m}^{-2}$ . This is comparable to the estimated two-dimensional heat divergence for that box ( $206 \text{ W m}^{-2}$ ) and within the 95% confidence intervals of the

advective estimate.

For the box going from 5°N to 5°S, the net surface heat flux is 240 W m<sup>-2</sup>, while the turbulent heat flux out of the euphotic layer is 26 W m<sup>-2</sup>. This implies a heating rate of 210 W m<sup>-2</sup>. This is larger than the heating rate obtained in the advective balance, 79 W m<sup>-2</sup>. However, the 95% confidence intervals of the net surface heat flux are large: 87–395 W m<sup>-2</sup>, and the uncertainties associated with the advective estimate and the heating rate overlap.

The heating rate obtained from the simple two-dimensional balance is comparable, as well, to that found using a three-dimensional model of the region between 5°N and 5°S and 150–110°W [Bryden and Brady, 1985]: 57 W m<sup>-2</sup>. These external consistency checks support the advective balance estimates to within an order of magnitude.

An additional loss term that so far has been neglected is mixing due to horizontal diffusion. The role of horizontal diffusion in the nitrate balance can be addressed by using a simple box-model type formulation as given in Eppley *et al.* [1979] in which the role of horizontal diffusion processes is compared to that of vertical mixing. For the 5°N–5°S box, the loss of nitrate due to diffusion from the sides is negligible because of the weak horizontal gradient.

Bryden and Brady [1989] propose that the horizontal eddy fluxes can be parameterized with an eddy diffusivity of order 10<sup>3</sup> m<sup>2</sup> s<sup>-1</sup> (between 0.01–1.4 · 10<sup>3</sup> m<sup>2</sup>s<sup>-1</sup> for the top 100 m at 152°W). The values used in equatorial models are typically somewhat larger, between 10<sup>3</sup> m<sup>2</sup>s<sup>-1</sup> and 5 · 10<sup>3</sup> m<sup>2</sup>s<sup>-1</sup> [Bryden and Brady, 1989, Wacongne, 1989].

If we take 3 · 10<sup>2</sup> m<sup>2</sup>s<sup>-1</sup> as a characteristic diffusivity value for the euphotic depth (Table 2, Bryden and Brady [1989]), the loss to horizontal diffusion is 0.22 mmol m<sup>-2</sup> day<sup>-1</sup> for the region; this is 17% of the nitrate supply due to vertical mixing and falls within the uncertainty of that term.

If we assume a larger horizontal diffusivity, 10<sup>3</sup> m<sup>2</sup> s<sup>-1</sup>, horizontal mixing of nitrate is 0.72 mmol m<sup>-2</sup> day<sup>-1</sup>, a significant portion of the turbulent nitrate supply (55%)

although it still falls within the 95% confidence intervals.

Thus, it seems that the loss due to horizontal diffusion is less than a factor of two of the vertical mixing term, which is well within the uncertainty of this estimate. Consequently, it does not seem to be a major sink for the nitrate balance of the region, especially compared with the large advective term.

The estimate of the total physical supply of nitrate into the euphotic zone for the equatorial region is compared with two measurements of biological nitrate uptake [Eppley and Renger, 1991, Wilkerson and Dugdale, 1991]. The rate of nitrate incorporation into particles [Wilkerson and Dugdale, 1991] is smaller than the 92% confidence intervals for the physical supply of nitrate for 1°N–1°S and smaller than the 95% confidence intervals for 5°N–5°S. The total physical nitrate supply is comparable to the measured nitrate utilization [Eppley and Renger, 1991].

The large discrepancy between the two measures of nitrate consumption was unexpected and is explored in detail by Eppley and Renger [1991]. They found high disappearance rates of nitrate during both day and night and conclude that the day-time estimates are correct but that the night-time rates are suspect. The 'anomalously' high nitrate disappearance rates may be related to the release of dissolved organic nitrogen (DON) and to an active microbial food web.

The conversion of nitrate to DON has been invoked before to explain higher nitrate consumption than particulate nitrate production [Eppley and Renger, 1991; and references therein]. Toggweiler [1989] reports that a balance solely between upward nutrient flux and sinking particles in a three-dimensional modelling study led to ever-increasing nutrient concentrations and particle export rates. The sinking particles remineralized at depth and the high-nutrient waters converged at 0° due to the deep geostrophic flow, thus leading to increasing nutrient concentration of the upwelling water. The most realistic simulations (nutrient distributions and particulate carbon flux comparable to the sediment trap results) were obtained when half of the new production due to upwelled nutrients went into a pool of dissolved organic nutrients. The concentration of DON was not assayed during our cruise, but the production

of dissolved organic carbon (DOC) was measured in a series of experiments and was only 10% of the particulate carbon production. Obviously, more data is needed on the production of DON and on its distribution in the equatorial region.

The large night-time disappearance rates suggest the existence of an active microbial community [Eppley and Renger, 1991]. The presence of picoplankton, that are actively consuming nitrate and too small to be completely retained by the filters used in the  $^{15}\text{N}$  method (Whatman GF/F) may account for an uncertainty of a factor of two [Eppley and Renger, 1991] or greater. Altabet [1990] found that 16–54% of the material collected on an Anopore filter ( $< 0.7\mu\text{m}$ ) leaked through a GF/F filter, and that this percentage was largest at depth. At 60 m the North Atlantic, 80% of the nitrate uptake was not detected with the GF/F filters. In this case, since the uptake in the surface water was much greater than at depth, the integrated uptake rates were not significantly underestimated. In the equatorial Pacific at  $135^\circ\text{W}$  [Peña, unpublished manuscript], the uptake rates at depth were similar to or greater than in the surface waters. For the equatorial time series at  $150^\circ\text{W}$ , Wilkerson and Dugdale [1991] found that the uptake rate was larger in the upper part of the euphotic layer. Obviously, the uptake of nitrate by very small cells will be confounded with the DON fraction. It is very important that the potential source of error associated with incomplete retention by the GF/F filters be addressed for the region.

In conclusion, the similarity in magnitude of the obtained rate of physical nitrate supply and the nitrate disappearance rates support these measurements, but do not explain the low measured particulate nitrate production. The physical supply of nitrate and the measured primary production imply that new production is 66–80% of the total production for  $1^\circ\text{N}$ – $1^\circ\text{S}$ ; between  $5^\circ\text{N}$ – $5^\circ\text{S}$ , it is 40%. These values are consistent with the day-time new production estimate of Eppley and Renger [1991] (60% of total production) but are higher than those derived from particulate nitrate production [Murray *et al.*, 1989, Wilkerson and Dugdale, 1991, Dugdale *et al.*, 1991] or export fluxes [Betzer *et al.*, 1984, Coale and Bruland, 1987, Murray *et al.*, 1989]. The present estimates of physical supply underline the potential importance of the

equatorial ocean in global new production. The difference between new production estimates from nitrate disappearance or physical supply and from particle formation or export suggests that the role of DON in the equatorial upwelling system is indeed an important one.

## 4.5 Summary

1. Nitrate supply to the euphotic zone in the equatorial region results from vertical mixing and from the advective balance between upwelling and meridional transport.
2. Turbulent nitrate supply is very large at  $0^\circ$  and  $1^\circ\text{S}$ , of order  $1 \text{ mmol m}^{-2} \text{ day}^{-1}$ . Away from this region, the supply due to vertical mixing is less than  $10^{-2} \text{ mmol m}^{-2} \text{ day}^{-1}$  and is two orders of magnitude smaller than the measured nitrate consumption.
3. A simple two-dimensional advective balance was carried out for meridional boxes spanning  $0^\circ$ . Between  $1^\circ\text{N}$  and  $1^\circ\text{S}$ , the net supply was  $4.25 \text{ mmol m}^{-2} \text{ day}^{-1}$ . For a box going from  $5^\circ\text{N}$  to  $5^\circ\text{S}$ , the net supply was around  $2 \text{ mmol m}^{-2} \text{ day}^{-1}$ .
4. The turbulent flux of nitrate to the meridional boxes was 30% of the net advective supply in both cases, this is a significant rate of nitrate supply.
5. The incorporation of  $^{15}\text{N}$  labelled nitrate into particles [Wilkerson and Dugdale, 1991] was smaller and the rate of disappearance of nitrate [Eppley and Renger, 1991] was of similar magnitude to the total nitrate supply.
6. The loss of nitrate due to lateral mixing, using characteristic values of horizontal diffusivity, was found to be within the uncertainty of the vertical mixing estimates and much smaller than the advective supply.

7. An analysis of the uncertainties and assumptions inherent to the methods used lead to the conclusion that the estimated nitrate supply provides a description to an order of magnitude of the 'mean' nitrate budget.
8. The estimated nitrate supply rates imply that new production is 66–80% of the total between 1°N and 1°S and 40% between 5°N and 5°S. These high values underscore the potentially large role of the equatorial Pacific in global biogeochemical cycles.
9. The agreement between the estimated nitrate supply and the nitrate disappearance rates and the discrepancy with the  $^{15}\text{N}$  uptake rates (and of previous estimates of particulate export flux) indicate that the role of dissolved organic nitrogen or of small cells ( $< 1\mu\text{m}$ ) may be very important and should be investigated further.

# Chapter 5

## Influence of phytoplankton on the thermal structure of the upper ocean

### 5.1 Introduction

In this short chapter, the role of phytoplankton in the vertical structure and heat budget of the upper layer is discussed. Chlorophyll, by modifying the optical attenuation coefficient of the water column, determines the vertical profile of light absorption, and hence the vertical distribution of heating. Some experimental evidence of instances in which changes in the chlorophyll concentration have led to variability in the surface water temperature will be presented and a simple non-dimensional parameter to quantify the role of the vertical light profile in the upper layer heat budget proposed. The focus will be specifically on the diurnal change in surface layer temperature.

#### 5.1.1 Diurnal heating of the oceans

During clear daylight hours, solar heating produces a warm surface layer. This heated surface water has increased buoyancy and stabilizes the water column, thus inhibiting

propagation of turbulent mixing. Under low wind stress conditions, the surface layer can become progressively warmer and very large diurnal heating signals ( $> 3^{\circ}\text{C}$ ) may be observed [Stramma *et al.*, 1986, Price *et al.*, 1987]. For higher winds, the temperature change is less ( $< 0.5^{\circ}\text{C}$ ), but extends to greater depth as the stress imposed at the surface mixes the water column and inhibits the formation of a stable warm surface layer. When the sun sets, heat goes toward the atmosphere from the water through evaporative and radiative cooling, leading to unstable stratification. The resulting buoyancy flux combined with wind mixing produces a mixing layer that intensifies and deepens as the night goes on. In Chapters 2 and 3, the diurnal cycle of turbulent mixing has been discussed for the equatorial time series measurements. This diurnal mixing cycle can be very pronounced, such as in the Tropic Heat observations [Peters *et al.*, 1988, Moum *et al.*, 1989].

### 5.1.2 The role of light in the diurnal heating signal

Approximately half of the incoming solar irradiance is in the infra-red and is absorbed within the first meter, the remaining is in the visible (wavelengths ranging between 300 and 700 nm). The downwelling irradiance in the visible decreases exponentially with depth, with an attenuation length scale governed by the absorption of the water itself and by the amount of absorbing substances dissolved or suspended in the water column. In the open ocean, where the concentrations of suspended and dissolved materials are small, the concentration of phytoplankton pigments is the major determinant of the vertical profile of downwelling light [Jerlov, 1976]. If the chlorophyll concentration in the surface layer is low, light will exit the base of the layer, becoming an energy loss term for the heat budget of the layer. If, conversely, the chlorophyll concentration is high, the light will be strongly absorbed close to the surface and a negligible amount of energy will be lost in the form of penetrative irradiance.

The importance of this process to the mixed layer dynamics has been noted from theoretical and modelling studies, of which notable examples are Denman [1973], Woods [1980] and Zaneveld *et al.* [1981].

The role of chlorophyll concentration in the thermal structure and heat budget of the upper ocean has two main consequences. On the one hand, penetrative irradiance (the heat loss at the base of the upper layer) may be a large component in the heat budget of the upper layer of the ocean (see Section 3.4.2). Since the importance of the penetrative irradiance term is dependent on the chlorophyll concentrations (and these may be subject to seasonal and longer term variability), the balance of terms controlling the heating rate of the surface ocean may be altered on these time scales.

On the other hand, varying chlorophyll concentrations, in response to either changes in the food-web structure or in nutrient concentrations, are accompanied by changes in the temperature of the upper layer. The change in surface layer temperature influences the stability and affects the potential energy budget of the upper water column. This leads to changes in the mixed layer depth. Although virtually all the visible light is absorbed within the water column, if the surface layer becomes very warm, it can affect the air-sea heat exchange and subsequently lead to changes in the total heat content [Mazumder *et al.*, 1990].

## 5.2 Some experimental evidence of the importance of variability in the chlorophyll concentration

Mazumder *et al.* [1990] studied small lakes and enclosures with and without planktivorous fish. When planktivorous fish were present, it was observed that the zooplankton stocks were grazed, and the phytoplankton concentrations bloomed. In the absence of planktivorous fish, the microzooplankton grazing of the phytoplankton kept the chlorophyll concentrations at lower levels. A direct relationship was found between the Secchi depth (the depth at which a white disk disappears from view: a measure of the optical attenuation length scale) and the mixed layer depth. When the attenuation length scale was short, light was absorbed in the upper part of the water

column, increasing the temperature and consequently the stability. Greater stability implies greater resistance to mixing and the temperature increase led to decreased mixed layer depths. As this shallow mixed layer continues receiving solar irradiance, the temperature increases and the sensible heat flux back to the atmosphere increases as well. Less heat propagates below the base of the mixed layer because although the gradient is strong, turbulent mixing is suppressed. Therefore the total measured heat content of the water column is less and the temperature of the lower layer is less than in lakes where the atmospheric forcing was the same but the chlorophyll concentration was less. The differences in thermal structure for lakes/enclosures with and without planktivorous fish were greatest for the months with greater incoming heat flux.

Sathyendranath *et al.* [1991] address the role of varying chlorophyll concentrations on a seasonal time scale. In the Arabian Sea, seasonal upwelling associated with the southwest monsoon leads to enhanced nutrients in the surface waters and blooms of phytoplankton. The chlorophyll concentrations go from  $0.05 \text{ mg chl m}^{-3}$  to  $10 \text{ mg chl m}^{-3}$ . To address the potential role of the changes in chlorophyll concentration in the sea-surface temperature, they used a Kraus-Turner mixed layer model [Kraus and Turner, 1967] and monthly averages of chlorophyll concentration from the Coastal Zone Color Scanner (CZCS). They ran the mixed layer model with monthly averages of surface forcing twice: (a) ignoring the presence of chlorophyll in the upper water column and (b) using the chlorophyll concentration to determine the vertical profile of light absorption. They found that the difference between the two model runs could be as large as  $3.6^\circ\text{C}$ . Taking into account the chlorophyll concentration led to increased warming during the heating phase of the seasonal cycle and to decreased cooling during the cooling phase. Variations in the sea-surface temperature modify the air-sea heat exchange, which in the tropics is important in determining the weather and climate. For example, the generation of tropical storms is related to the presence of high sea-surface temperatures.

Lewis *et al.* [1990], as commented in section 3.4.2, carried out a study to assess the role of penetrative irradiance in the heat budget of the equatorial Pacific. The mixed layer depth, from the Levitus atlas, is deepest in the central region, and shoals to the east and west (a shallow halocline is observed in the western basin [Lukas and Lindstrom, 1991]). The penetrative irradiance at the base of the mixed layer was obtained using the attenuation coefficient for 490 nm from CZCS. It was found that in the western basin, the net surface heat flux was comparable to the heat loss in the form of light at the base of the mixed layer. Because of the wide-spread implications in climate, fisheries and agriculture of the ENSO [Philander, 1990], large effort has gone into modelling the interaction between ocean and atmosphere in the equatorial region. Current models, which assume that the net surface heat flux is absorbed in its entirety in the mixed layer, consistently overestimate the SST of the western basin. Changes in the attenuation length scale of the water column in this region would lead to variability in the heating rate of the upper layer, with implications for the heat exchange with the atmosphere.

On a shorter time scale, the role of penetrative irradiance in determining the diurnal signal of the surface layer was discussed for a four and a half day time series at  $0^\circ$  (section 3.4.2). Although the penetrative irradiance was only 12% of the total incoming heat flux at the surface, it was the same order of magnitude as the surface heat loss and was larger than the turbulent heat flux at that depth. Thus, it was an important term in the one-dimensional heat budget, although it was observed that the advective transport of heat was more important in determining the observed changes in heat content.

In the next section, a simple model to describe the role of chlorophyll concentrations in the diurnal signal of surface layer temperature is proposed.

### 5.3 A simple model describing the role of chlorophyll in the heating rate of the upper ocean

The downward irradiance is parameterized using the following expression:

$$E(z) = \frac{E(0)}{2} e^{-K_1 z} + \frac{E(0)}{2} e^{-K_2 z} \quad (5.1)$$

where  $E(0)$  is the irradiance at the sea surface,  $E(z)$  is the irradiance at a given depth  $z$ , the first term represents the infra-red and the second term the visible. Although a fully spectral model is more exact, Simpson and Dickey [1981] found that for dynamical purposes, the model with two exponential terms was able to resolve the major features of the vertical profile of light absorption. The attenuation coefficients,  $K_1$  and  $K_2$  in  $\text{m}^{-1}$  are given by:

$$K_1 = 1.67 \quad (5.2)$$

$$K_2(\text{chl}) = 0.121 [\text{chl}]^{0.428} \quad (5.3)$$

where  $[\text{chl}]$  is the concentration of chlorophyll in  $\text{mg m}^{-3}$ . The attenuation coefficient used for the infrared ( $K_1$ ) is taken from Paulson and Simpson [1977], obtained by doing an empirical fit to data from Jerlov [1976] of the vertical profile of downwelling light for different water types (*i.e.* with different light absorption characteristics). The attenuation coefficient for the visible light (300–700 nm) is taken to be a function of chlorophyll concentration,  $[\text{chl}]$ . This power law formulation [Morel, 1988] is applicable to open ocean-type waters, and is valid for chlorophyll concentrations ranging from 0.3 to 30  $\text{mg m}^{-3}$ .

The mixed layer depth is parameterized with the Monin-Obukhov length:

$$D \sim \frac{-u_*^3}{0.4J_b} \quad (5.4)$$

where, as explained in section 3.2,  $u_*$  is the friction velocity, proportional to the wind stress, and  $J_b$  is the buoyancy flux ( $J_b = g\alpha/\rho C_p (E(0) + Q_+)$ ), where  $Q_+$  is the sum of latent, sensible and long-wave heat fluxes. The Monin-Obukhov length was

chosen to provide the mixed layer depth because it incorporates both wind stress and convection. The Monin-Obukhov length results from dimensional analysis as the depth scale if no external time scale is taken into account in the one-dimensional heating rate [Price *et al.*, 1986]. It is an estimator of the mixed layer depth only in the case of net surface heating and when a balance is established between the increased potential energy due to warming and the kinetic energy dissipated by wind mixing.

The energy absorption, or radiant heating, due to downwelling light is given by the divergence of the irradiance profile [Siegel and Dickey, 1987]

$$\frac{\partial T}{\partial t} = -\frac{1}{\rho C_p} \frac{\partial E(z)}{\partial z} \quad (5.5)$$

while the heating rate of the water column is expressed by the one-dimensional heat equation:

$$\frac{\partial T}{\partial t} = -\frac{1}{\rho C_p} \frac{\partial (E(z) + J_q(z))}{\partial z} \quad (5.6)$$

where  $J_q$  is the turbulent heat flux as defined in section 2.2. To find the temperature change of the entire mixed layer, Eq. (5.6) is integrated between  $D$  and the surface:

$$\int_0^D \frac{\partial T}{\partial t} dz = \frac{1}{\rho C_p} \int_0^D \frac{\partial (E(z) + J_q(z))}{\partial z} dz \quad (5.7)$$

which becomes for a an interval of time  $\Delta t$ :

$$\frac{\Delta T}{\Delta t} = \frac{1}{D} \frac{1}{\rho C_p} [E(z) + J_q(z)]_0^D \quad (5.8)$$

$$\frac{\Delta T}{\Delta t} = \frac{1}{D} \frac{1}{\rho C_p} \left( E(0) + Q_+ - \frac{E(0)}{2} (e^{-K_1 D} + e^{-K_2 D}) + J_q(D) \right) \quad (5.9)$$

The temperature change in the mixed layer is proportional to the difference between the net incoming heat flux at the surface and the energy lost at depth due to turbulent mixing and penetrative irradiance (section 3.4.2). Since  $K_1^{-1}$  is generally much smaller than  $D$ , the infrared light penetrating the base of the mixed layer is negligible and the term  $E(0) e^{-K_1 D}$  can be omitted so Eq. (5.9) becomes

$$\frac{\Delta T}{\Delta t} = \frac{1}{D} \frac{1}{\rho C_p} \left( E(0) + Q_+ - \frac{E(0)}{2} e^{-K_2 D} + J_q(D) \right) \quad (5.10)$$

For a given value of the surface flux, the radiant heating of the layer depends on the non-dimensional parameter  $K_2D$ , the ratio of the attenuation length scale  $K_2$  and the depth of the mixed layer. If the attenuation length scale is large (small  $K_2$ ), the amount of light lost to the mixed layer may be important; for short attenuation length scales (or deep mixed layers), most of the visible light will be absorbed within the mixed layer. The parameter  $K_2D$  is a function of the chlorophyll concentration and of the wind speed: since  $K_2$  is proportional to the square root of  $[chl]$  and  $D$  is proportional to the wind speed cubed, the dependence on the latter is generally more significant.

In Figure 5.1 we see the parameter dependence of  $K_2D$  on the chlorophyll concentration and on the wind speed. For high wind speeds ( $> 12 \text{ m s}^{-1}$ ) or low ones ( $< 5 \text{ m s}^{-1}$ ),  $K_2D$  is greater than, or less than one, respectively, regardless of the chlorophyll concentration.  $K_2D$  increases asymptotically with chlorophyll concentration for wind speeds between 5 and  $10 \text{ m s}^{-1}$ .  $K_2D$  increases exponentially with wind speed; the wind speed at which  $K_2D$  becomes irrelevant to the heating profile ( $K_2D > 5$ ) depends on the chlorophyll concentration. It is around  $10 \text{ m s}^{-1}$  for waters with  $20 \text{ mg chl m}^{-3}$ , and greater than  $15 \text{ m s}^{-1}$  for  $1 \text{ mg chl m}^{-3}$ .

Another heat loss at the base of the layer is due to turbulent mixing. The turbulent heat flux (section 2.2) is given by the eddy diffusivity, which in turn can be related to wind or convective mixing (section 3.3.2), and the temperature gradient at the base of the layer. The temperature gradient depends on the heating rate and time of the day. Because of the difficulty in parameterizing this term, it will be neglected for the rest of the discussion. Although the turbulent heat flux may be a large component of the one-dimensional heat budget, it is only dependent on the radiant heating inasmuch the temperature gradient and stability increase. We therefore consider it an 'external' variable such as the incoming surface fluxes. This simplification will lead to excessively large diurnal temperature signals.

The diurnal signal in temperature can be further studied by non-dimensionalizing Eq. (5.10). The total surface heat flux is designated by  $Q(0)$ ,  $Q(0) = E(0) + Q_+$ .

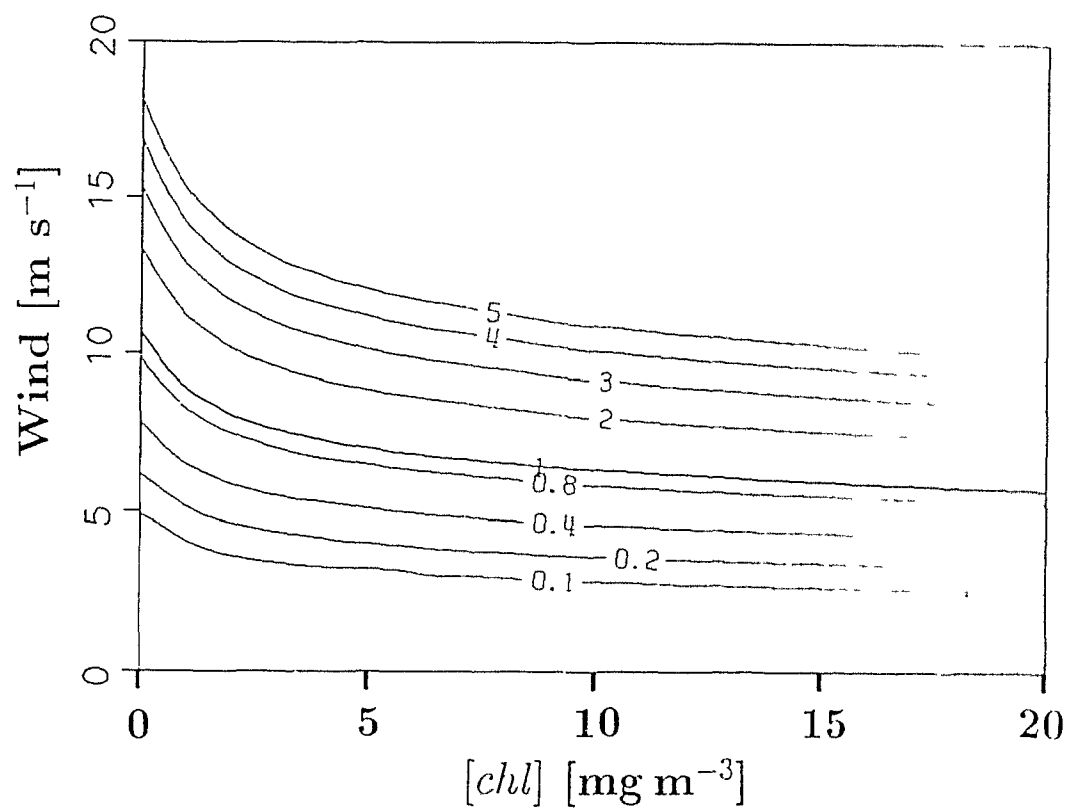


Figure 5.1: The parameter dependence of  $K_2D$  on chlorophyll concentration and wind speed.

If all the heat is absorbed in the layer  $D$  and there is no heat loss due to turbulent mixing, the maximum heating rate is given by:

$$\left(\frac{\Delta T}{\Delta t}\right)_{max} = \frac{Q(0)}{D \rho C_p} \quad (5.11)$$

Then, dividing Eq. (5.10) by Eq. (5.11) the non-dimensional temperature change is obtained:

$$\frac{\Delta T/\Delta t}{(\Delta T/\Delta t)_{max}} = \frac{1/(D \rho C_p) (E(0) + Q_+ - E(0)/2e^{-K_2 D} + J_q(D))}{Q(0)/(D \rho C_p)}$$

$$\frac{\Delta T^*}{\Delta t} = 1 - \frac{E(0)}{2Q(0)} e^{-K_2 D} + \frac{J_q(D)}{Q(0)} \quad (5.12)$$

The non-dimensionalized heating rate is thus a function of  $K_2 D$ , the ratio between the mixed layer depth and optical length scale and  $E(0)/Q(0)$ , the ratio of short-wave to total surface heat flux or the contribution of light to the incoming heat. We disregard  $J_q(D)/Q(0)$  as stated above. It can be an important: for our equatorial time series it was only 0.06 but for Moum *et al.* [1989] it was 0.7. Further work should be carried out to incorporate the turbulent heat loss into this simple one-dimensional model.

The non-dimensionalized heating rate is expressed as a function of  $K_2 D$  and  $E(0)/Q(0)$  in Figure 5.2. In the day-time of the spring and summer months, the ratio between the incoming light and the total heat flux will be positive. If the sum of radiative, latent and sensible heat ( $Q_+$ ) is negative, the ratio  $E(0)/Q(0)$  will be greater than one. Conversely, when  $Q_+$  is positive, *i.e.* heat going into the ocean, the ratio is less than zero. In this case (infrequent, only observed with very cold waters underlying warm air), radiant heating is not an important term in the one-dimensional balance. For low values of  $E(0)$ , the penetrative irradiance becomes negligible and, even for low values of  $K_2 D$ , most of the heat is absorbed in the mixed layer.

For  $E(0)/Q(0)$  greater than one, the role of penetrative irradiance is small for  $K_2 D$  values greater than two: the heating rate is 90% of maximum values when  $K_2 D$  is larger than 1.5, and approaches 100% for  $K_2 D$  greater than 2.5. In these cases it is appropriate to neglect the penetrative irradiance.

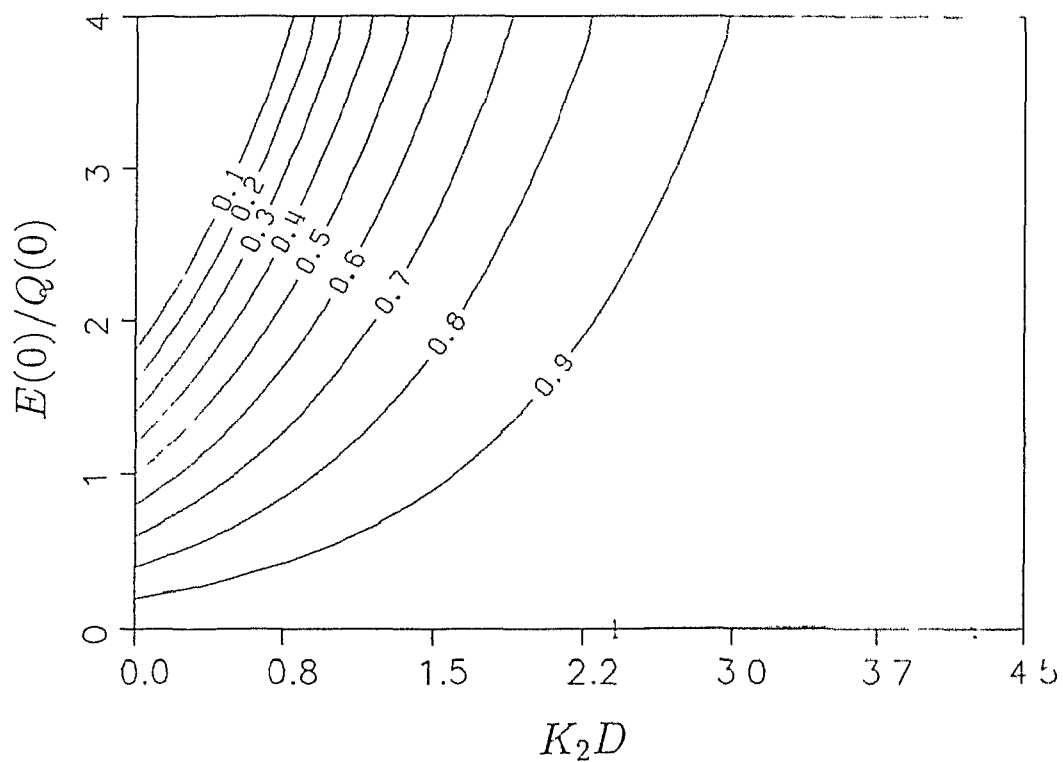


Figure 5.2: The parameter dependence of  $\Delta T^*/\Delta t$  on the non-dimensional parameters  $K_2D$  and  $E(0)/Q(0)$ .

Consequently, the region in the parameter space where penetrative irradiance can significantly affect the heating rate is for  $K_2D$  values around one or less. The amount of heat lost to the mixed layer is proportional to the relative importance of the short-wave flux: for low solar irradiance values, only 10% of the energy is lost while for very high  $E(0)/Q(0)$ , and  $K_2D$  less than 0.8, up to 90% of the incoming light exits the mixed layer. When the optical attenuation length scale is smaller or similar to the mixed layer depth, the ratio between short-wave and total flux is crucial in determining the heating rate. For large ratios  $E(0)/Q(0)$ , small changes in  $K_2D$ , will lead to greater heating rates. This is very important for example, in spring conditions in the north Atlantic. The mixed layer shoals as the surface heat flux increases. The chlorophyll concentrations can change from 0.5 to 10 mg m<sup>-3</sup> (and the attenuation length scale varies accordingly from 30 m to 3 m). At this moment, as the ratio of incoming solar irradiance becomes larger than one and the chlorophyll concentration increases, the heating rate of the upper layer will increase very rapidly.

## 5.4 Conclusions

Experimental and modelling studies have shown that including the concentration of chlorophyll to determine the radiant heating of the surface layer leads to larger surface temperatures than just considering the absorption of water alone [Mazumder *et al.*, 1990, Sathyendranath *et al.*, 1991]. Conversely, the assumption that all the incoming irradiance is absorbed within the mixed layer is mistaken for regions with long attenuation length scales [Lewis *et al.*, 1990]. The optical properties of the surface layer are relevant to the rate of radiant heating of this layer.

For deep mixed layers it can be assumed that all the incoming light is absorbed within the layer. Thus, the concentration of photosynthetic pigments will not be a controlling factor of upper layer structure when and where the mixed layer is deep. For shallow mixed layers, the optical attenuation length scale is crucial in determining the surface heating. For example, in spring at 110°W, 0°, where the mixed layer is

not determined by one-dimensional fluxes [Philander, 1990], as the surface heat flux starts to increase, the amount of heat actually absorbed by the mixed layer may be less than expected [Hayes *et al.*, 1991], thus reducing the actual heating rate. If additionally, the chlorophyll concentration changes on a seasonal basis, or on longer time scales, a single parameterization [Price *et al.*, 1986, Price *et al.*, 1987] of the optical attenuation coefficient is not necessarily appropriate. If the time period of study is one of expected variability (*e.g.* spring bloom), the optical attenuation length scale can vary by a factor of 10.

The non-dimensional parameter  $K_2D$  is indicative of the importance of penetrative irradiance in the mixed layer heating. If  $K_2D$  is one or less, the energy absorbed in the layer  $D$  varies from 10 to 70% of the available energy for heating. In the equatorial time series described in section 3.4.2., the  $K_2D$  was one, and the penetrative energy loss was on average 25% of the net incoming heat flux at the surface. The penetrative irradiance at 15 m was the largest loss term in the one-dimensional budget. Even for  $K_2D$  values of 2.12, where the exiting light is only 12% of the net incoming heat flux (the equatorial time series with  $D = 35$  m), the mean penetrative irradiance was the same size as the turbulent heat flux at depth and comparable to the surface heat losses. Hence, the role of penetrative irradiance depends not only on the depth of the mixed layer and the chlorophyll concentration, but on the magnitude of the other terms in the one-dimensional heat budget.

The non-dimensionalized heating rate revealed that for  $K_2D$  values greater than 3, the heating rate will be essentially maximum. When the mixed layer depth and the optical length scale are comparable, the ratio of short-wave and total surface heat flux becomes important. If the ratio is less than one (rare), radiant heating is unimportant and the penetrative heat loss also. For  $E(0)/Q(0)$  greater than one, small changes in  $K_2D$  imply significant changes in the heating rate of the upper layer.

This simple model neglects turbulent heat flux, and further work is needed to incorporate this term into the balance. It can be an important contribution: the turbulent heat flux at the base of the mixed layer was 70% of the net surface flux at

0° in Tropic Heat 1 [Moum *et al.*, 1989].

The mixed layer depth is the single most important factor determining the heating rate of the layer. For shallow mixed layers, it is important to determine the optical length scale: if  $K_2D$  is less than three, a simple comparison between the exiting light and the other loss terms of the one-dimensional balance is warranted. The magnitude of the seasonal and longer term variability of the chlorophyll concentration and mixed layer depth make this simple calculation very important in some regions, such as the north Atlantic or the Arabian Sea.

# Chapter 6

## Conclusions

This thesis has addressed the interaction of large-scale physical forcing and vertical mixing in the equatorial Pacific in spring 1988. This was then placed in the context of nitrate supply to the upper layer. The large-scale patterns of scalars (*e.g.* temperature, nutrients, chlorophyll), relative velocities and vertical mixing parameters were presented for the meridional transect and the equatorial time series. The observed distributions in time and space were then interpreted in terms of their controlling factors. For example, nutrients were studied as a function of physical transport and biological consumption and turbulent dissipation was addressed in relation to the surface forcing and water column structure. The major conclusions of the thesis are:

- The hydrography and air-sea fluxes were typical for boreal spring. It is proposed that the observed temporal and spatial variability of dissipation was determined by this large-scale forcing.

The EUC was shallow and intense; the incoming irradiance was high; the air was warmer than the sea surface and the wind speeds were low.

This implied that the mixed layer was shallow during the day and that night-time heat losses were small. The heat absorbed at the surface was not mixed downwards because the wind stress was too low. The shallow EUC core led to a stratified layer close to the surface.

- The observed temporal and spatial patterns of mixing reflect these constraints. The diurnal cycle at  $0^\circ$  was limited to the top 20 m, and the largest dissipation values were observed at 55 m.

Because the temporal variability was not large, the meridional pattern of dissipation presented a statistically significant maximum associated with the EUC between  $0^\circ$  and  $1^\circ\text{S}$ .

The observed mixed layer and thermocline dissipation rates at the equator were not correlated with either wind or the buoyancy flux. Dissipation was modelled using similarity scaling, yielding lesser values than observed. The mixed layer dissipation was correlated to the shear between 14 and 22 m.

Dissipation values increased with depth to maximum values around 55 m. This led to different vertical distributions of the turbulent flux of heat and momentum than the results of Tropic Heat.

- The residual of the balance between the long-term annual momentum terms and the turbulent stress divergence between 0 and 60 m was -19% of the zonal pressure gradient. The agreement is interesting as it indicates that the turbulent stress within the water column plays a different role in the large-scale balances on a seasonal basis.
- The one-dimensional heat budget of the upper layer was determined by the large incoming solar irradiance at the surface. The penetrative irradiance was the major heat loss term at the base of the layer. In Tropic Heat 1, the penetrative irradiance was small and the turbulent heat loss was large at the base of the upper layer.
- The nitrate supply in the equatorial region is due mainly to advective supply from upwelling and meridional flux. The turbulent nitrate supply is 30% of the advective supply. This large value is probably of seasonal nature, as the large diffusivities observed at depth for this time series were absent in Tropic Heat 1.

The nitrate supply is balanced by the measured rate of nitrate disappearance but is greater than the rate of particulate incorporation of nitrate. This underscores the need to quantify the role of dissolved organic nitrogen in the equatorial ocean.

- Increases in nitrate supply to 150°W, 0° probably will not affect the phytoplankton standing stock, as the nutrients are already in excess. A change in the advective balance could entail a decrease in nitrate supply and subsequent disequilibria between grazers and phytoplankton.
- Changes in chlorophyll concentration are evaluated in terms of their role in the heating rate of the upper ocean. The non-dimensional parameter  $K_2D$  indicates when penetrative irradiance may be a significant loss term to the surface layer. The non-dimensionalized heating rate was proportional to  $K_2D$  and to the ratio of short-wave heat flux to the total surface flux.

The intensive measurements made at 0° in Tropic Heat 1 revealed a fascinating picture of intense turbulence and strong temporal variability that have been taken by some to be the basic state for the region. Tropic Heat 2, in April 1987, the results of which are now appearing in the literature, presented very different conditions. It is necessary for further measurements to be made throughout the annual cycle to fully comprehend the processes governing the equatorial system [Hebert *et al.*, 1991b].

Our data set, although not as detailed or complete as those taken during Tropic Heat, is important as the first set of intensive measurements taken during a 'typical' spring. Likewise, the goal of the cruise was to assess the role of the equatorial region in global biogeochemical cycles. This meant that emphasis was placed on chemical, optical and biological measurements.

Although there were similarities between the present results and those of Tropic Heat (the general magnitudes of the parameters, the relationship with some of the forcing terms, the large-scale patterns), there were also significant differences (such as the weak diurnal cycle at 0° and a significant equatorial maximum of dissipation).

It is proposed that the differences result from the seasonal variability in hydrographic and meteorological forcing.

Future studies are needed throughout the annual cycle to address the variability of the equatorial region. Its role in large-scale global biogeochemical cycles and weather make this objective a priority. It is not possible to understand the role of vertical mixing of momentum in the basin-wide balance nor in global new production without additional comprehensive and, preferably, interdisciplinary studies.

## Bibliography

- ALTABET, M. A. (1990). Organic C, N, and stable isotopic composition of particulate matter collected on glass-fiber and aluminum oxide filters. *Limnology and Oceanography*, 35:902-909.
- BAKER, M. A. AND GIBSON, C. H. (1987). Sampling turbulence in the stratified ocean: Statistical consequences of strong intermittency. *Journal of Physical Oceanography*, 17:1817-1836.
- BATCHELOR, G. K. (1959). Small scale variation of convected quantities like temperature in a turbulent fluid. *Journal of Fluid Mechanics*, 5:113-133.
- BETZER, P. R., SHOWERS, W. T., LAWS, E. A., WINN, C. D., DiTULLIO, G. R., AND KROOPNICK, P. R. (1984). Primary productivity and particle fluxes on a transect of the equator at 153°W in the Pacific Ocean. *Deep Sea Research*, 31:1-11.
- BJERKNES, J. (1969). Atmospheric teleconnections from the equatorial Pacific. *Monthly Weather Review*, 97:163-172.
- BRADY, E. C. AND BRYDEN, H. L. (1987). Estimating vertical velocity at the equator. In *Oceanol. Acta, Proceedings International Symposium on Equatorial Vertical Motion, Paris, 6-10 May, 1985*, pages 33-37.

- BRYDEN, H. L. AND BRADY, E. C. (1985). Diagnostic model of the three-dimensional circulation in the upper equatorial Pacific ocean. *Journal of Physical Oceanography*, 15:1255–1273.
- BRYDEN, H. L. AND BRADY, E. C. (1989). Eddy momentum and heat fluxes and their effects on the circulation of the equatorial Pacific. *Journal of Marine Research*, 47:55–79.
- CHAVEZ, F. P. (1989). Size distribution of phytoplankton in the central and eastern tropical Pacific. *Global Biogeochemical Cycles*, 3:27–35.
- CHAVEZ, F. P. AND BARBER, R. T. (1987). An estimate of new production in the equatorial Pacific. *Deep Sea Research*, 34:1229–1243.
- CHERESKIN, T. K., MOUM, J. N., P. J. STABENO, D. R. C., PAULSON, C. A., REGIER, L. A., AND HALPERN, D. (1986). Fine-scale variability at 140°W in the equatorial Pacific. *Journal of Geophysical Research*, 91:12,887–12,898.
- COALE, K. H. AND BRULAND, K. W. (1987). Oceanic stratified euphotic zone as elucidated by  $^{234}\text{Th}$ : $^{238}\text{U}$  disequilibria. *Limnology and Oceanography*, 32:189–200.
- CRAWFORD, W. R. (1982). Pacific equatorial turbulence. *Journal of Physical Oceanography*, 12:1137–1149.
- CRAWFORD, W. R. AND DEWEY, R. K. (1989). Turbulence and mixing: sources of nutrients on the Vancouver Island continental shelf. *Atmosphere-Ocean*, 27(2):428–442.
- CULLEN, J. J., LEWIS, M. R., DAVIS, C. O., AND BARBER, R. T. (1991). Photosynthesis characteristics and estimated growth rates indicate grazing is the proximate control of primary production in the Equatorial Pacific. *Journal of Geophysical Research*, this volume.
- DENMAN, K. L. (1973). A time-dependent model of the upper ocean. *Journal of Physical Oceanography*, 3:173–184.

DENMAN, K. L. AND MIYAKE, M. (1973). Upper layer modification at Ocean Station Papa: observations and simulations. *Journal of Physical Oceanography*, 3:185-196.

DILLON, T. M., MOUM, J. N., CHERESKIN, T. K., AND CALDWELL, D. R. (1989). Zonal momentum balance at the equator. *Journal of Physical Oceanography*, 19:561-570.

DUGDALE, R. C. AND GOERING, J. J. (1967). Uptake of new and regenerated forms of nitrogen in primary productivity. *Limnology and Oceanography*, 12:196-206.

DUGDALE, R. C., WILKERSON, F., BARBER, R., AND CHAVEZ, F. (1991). Estimating new production in the equatorial Pacific. *Journal of Geophysical Research*, in press.

EFRON, B. AND GONG, G. (1983). A leisurely look at the bootstrap, the jackknife and cross-validation. *The American Statistician*, 37:36-48.

EPPLEY, R. W. AND RENGER, E. (1991). Nitrate utilization by plankton in the equatorial Pacific, March 1988 along 150°W. *Journal of Geophysical Research*, in press.

EPPLEY, R. AND PETERSON, B. (1979). Particulate organic matter flux and planktonic new production in the deep ocean. *Science*, 282:677-680.

EPPLEY, R., RENGER, E., AND HARRISON, W. (1979). Nitrate and phytoplankton production in southern California coastal waters. *Limnology and Oceanography*, 24:483-494.

ERIKSEN, C. C. (1985). The Tropic Heat Program: an overview. *EOS*, 66:50-52.

FELDMAN, G. C. (1986). Variability in the productive habitat in the eastern equatorial Pacific. *EOS, Trans. Amer. Geophys. Union*, 67:106-108.

GILL, A. E. (1982). *Atmosphere-Ocean Dynamics*. Academic Press, London.

GREGG, M. C. (1987). Diapycnal mixing in the thermocline. *Journal of Geophysical Research*, 92:5249–5286.

GREGG, M. C., PETERS, H., WESSON, J. C., OAKEY, N. S., AND SHAY, T. J. (1985). Intensive measurements of turbulence and shear in the equatorial undercurrent. *Nature*, 318:140–144.

HALPERN, D. AND FREITAG, P. H. (1987). Vertical motion in the upper ocean of the equatorial Eastern Pacific. In *Oceanol. Acta, Proceedings International Symposium on Equatorial Vertical Motion, Paris, 6-10 May, 1985*, pages 19–26.

HALPERN, D., KNOX, R. A., LUTHIER, D. S., AND PHILANDER, S. G. H. (1989). Estimates of equatorial upwelling between 140° and 110°W during 1984. *Journal of Geophysical Research*, 94:8018–8020.

HAMILTON, J. M. AND RUDDICK, M. R. L. B. R. (1989). Vertical fluxes of nitrate associated with salt fingers in the world's oceans. *Journal of Geophysical Research*, 94:2137–2145.

HAYES, S. P., CHANG, P., AND MCPHADEN, M. J. (1991). Variability of the sea surface temperature in the eastern equatorial Pacific during 1986–1988. *Journal of Geophysical Research*, 96:10,553–10,566.

HEBERT, D., MOUM, J. N., AND CALDWELL, D. R. (1991a). Does ocean turbulence peak at the equator? : Revisited. *Journal of Physical Oceanography*, in press.

HEBERT, D., MOUM, J. N., PAULSON, C. A., CALDWELL, D. R., CHERESKIN, T. K., AND MCPHADEN, M. J. (1991b). Detailed structure of the upper ocean in the central equatorial Pacific during April 1987. *Journal of Geophysical Research*, 96:7127–7136.

- HOREL, J. D. AND WALLACE, J. M. (1981). Planetary-scale atmospheric phenomena associated with the Southern Oscillation. *Monthly Weather Review*, 109:813-829.
- IMAWAKI, S., NILER, P. P., GAUTIER, C. H., HALPERN, D., KNOX, R. A., LARGE, W. G., LUTHER, D. S., MCWILLIAMS, J. C., MOUM, J. N., AND PAULSON, C. A. (1988). A new method for estimating the turbulent heat flux at the bottom of the daily mixed layer. *Journal of Geophysical Research*, 93:14,005-14,012.
- JANOWIAK, J. E. (1988). Seasonal Climate Summary: The global climate for March-May 1988: The end of the 1986-1987 Pacific Warm Episode and the onset of widespread drought in the United States. *Journal of Climate*, 1:1019-1042.
- JERLOV, N. G. (1976). *Marine Optics*. Elsevier, New York.
- KING, F. D. AND DEVOL, A. H. (1979). Estimates of vertical eddy diffusion through the thermocline from phytoplankton nitrate uptake rates in the mixed layer of the eastern tropical Pacific. *Limnology and Oceanography*, 24:645-651.
- KRAUS, E. B. AND TURNER, J. S. (1967). A one-dimensional model of the seasonal thermocline: II. the general theory and its consequences. *Tellus*, 36A:292-305.
- LEWIS, R., M., HARRISON, W. G., OAKEY, N. S., HEBERT, D., AND PLATT, T. (1986). Vertical nitrate fluxes in the oligotrophic ocean. *Science*, 234:870-873.
- LEWIS, M. R., CARR, M.-E., FELDMAN, G., ESAIAS, W., AND MCCLAIN, C. (1990). Satellite estimates of the influence of penetrating solar radiation on the heat budget of the equatorial Pacific Ocean. *Nature*, 347:543-545.
- LIU, W. AND GAUTIER, C. (1990). Thermal forcing in the tropical Pacific from satellite data. *Journal of Geophysical Research*, 95:13209-13217.

- LOMBARDO, C. P. AND GREGG, M. C. (1989). Similarity scaling of viscous and thermal dissipation in a convecting surface boundary layer. *Journal of Geophysical Research*, 94:6273-6284.
- LUKAS, R. AND LINDSTROM, E. (1991). The mixed layer of the western equatorial Pacific Ocean. *Journal of Geophysical Research*, 96, suppl.:3343-3357.
- MANGUM, L. J. AND HAYES, S. P. (1984). The vertical structure of the zonal pressure gradient in the eastern equatorial Pacific. *Journal of Geophysical Research*, 89:10441-10449.
- MAZUMDER, A., TAYLOR, W. D., MCQUEEN, D. J., LEAN, D. R. S., AND LAFONTAINE, N. R. (1990). A comparison of lakes and lake enclosures with contrasting abundances of planktivorous fish. *Journal of Plankton Research*, 12:109-124.
- MCPHADEN, M. J. AND HAYES, S. P. (1990). Variability in the eastern equatorial Pacific Ocean during 1986-1988. *Journal of Geophysical Research*, 95:13,195-13,208.
- MCPHADEN, M. J. AND TAFT, B. A. (1988). Dynamics of seasonal and intraseasonal variability in the eastern equatorial Pacific. *Journal of Physical Oceanography*, 18:1713-1732.
- MILES, J. W. (1961). On the stability of heterogeneous shear flows. *Journal of Fluid Mechanics*, 10:496-508.
- MOREL, A. (1988). Optical modeling of the upper ocean in relation to its biogenous matter content (case I waters). *Journal of Geophysical Research*, 93:10,749-10,768.
- MOUM, J. N. AND CALDWELL, D. R. (1985). Local influences on shear flow turbulence in the equatorial ocean. *Science*, 230:315-316.

- MOUM, J. N., CALDWELL, D. R., AND PAULSON, C. A. (1989). Mixing in the equatorial surface layer and thermocline. *Journal of Geophysical Research*, 94:2005-2021.
- MOUM, J. N., PAULSON, C. A., CHERESKIN, T. K., AND REGIER, L. A. (1986). Does oceanic turbulence peak at the equator? *Journal of Physical Oceanography*, 16:1991-1994.
- MURRAY, J., DOWNS, J., STROM, S., WEI, C., AND JANNASCH, H. (1989). Nutrient assimilation, export production and  $^{234}\text{Th}$  scavenging in the eastern equatorial Pacific. *Deep Sea Research*, 36:1471-1489.
- NIILER, P. AND STEVENSON, J. (1982). The heat budget of tropical ocean warm-water pools. *Journal of Marine Research*, 40 suppl.:465-480.
- OAKEY, N. S. (1985). Statistics of mixing parameters in the upper ocean during JASIN phase 2. *Journal of Physical Oceanography*, 15:1662-1675.
- OAKEY, N. S. (1988). Epsonde: An instrument to measure turbulence in the deep ocean. *IEEE Journal of Oceanic Engineering*, 13:124-128.
- OAKEY, N. S. AND ELLIOTT, J. A. (1982). Dissipation within the surface mixed layer. *Journal of Physical Oceanography*, 12:171-185.
- OSBORN, T. R. (1980). Estimates of the local rate of vertical diffusion from dissipation measurements. *Journal of Physical Oceanography*, 10:83-89.
- OSBORN, T. R. AND COX, C. S. (1972). Oceanic finestructure. *Geophysical Fluid Dynamics*, 3:321-345.
- OSBORN, T. R. AND CRAWFORD, W. R. (1980). An airfoil probe for measuring velocity fluctuations in water. In DOBSON, F. W., HASSE, L., AND DAVIS, R., editors, *Air-Sea Interactions: Instruments and Methods*, pages 369-386. Plenum: New York.

- PACANOWSKI, R. C. AND PHILANDER, S. G. H. (1981). Parameterization of vertical mixing in numerical models of the tropical Pacific. *Journal of Physical Oceanography*, 11:1443-1451.
- PAULSON, C. A. AND SIMPSON, J. J. (1977). Irradiance measurements in the upper ocean. *Journal of Physical Oceanography*, 7:952-956.
- PEÑA, M. A., LEWIS, M. R., AND HARRISON, W. G. (1990). Primary productivity and size structure of phytoplankton biomass on a transect of the equator at 135°W in the Pacific Ocean. *Deep Sea Research*, 37:295-315.
- PETERS, H. AND GREGG, M. C. (1988). Some dynamical and statistical properties of equatorial turbulence. In NIHOUL, J. C. J. AND JAMART, B. M., editors, *Small-scale turbulence and mixing in the ocean*, pages 185-200. Elsevier Oceanography Series, 46.
- PETERS, H., GREGG, M. C., AND TOOLE, J. M. (1988). On the parameterization of equatorial turbulence. *Journal of Geophysical Research*, 93:1199-1218.
- PETERS, H., GREGG, M., AND TOOLE, J. M. (1989). Meridional variability of turbulence through the equatorial undercurrent. *Journal of Geophysical Research*, 94:18003-18009.
- PHILANDER, G. (1989). El Niño and La Niña. *American Scientist*, 77:451-459.
- PHILANDER, S. G. (1990). *El Niño, La Niña and the Southern Oscillation*. Academic Press.
- PRICE, J. F., WELLER, R. A., BOWERS, C. M., AND BRISCOE, M. G. (1987). Diurnal response of sea surface temperature observed at the Long Term Upper Ocean Study (34°N and 70°W) in the Sargasso Sea. *Journal of Geophysical Research*, 92:14,480-14,490.

- PRICE, J. F., WELLER, R. A., AND PINKEL, R. J. (1986). Diurnal cycling: Observations and models of the upper ocean response to diurnal heating and cooling and wind mixing. *Journal of Geophysical Research*, 91:8411-8427.
- RICHMAN, J. AND GARRETT, C. (1977). The transfer of energy and momentum by the wind to the surface mixedlayer. *Journal of Physical Oceanography*, 7:876-881.
- ROHR, J. AND VAN ATTA, C. (1987). Mixing efficiency in stably stratified growing turbulence. *Journal of Geophysical Research*, 92:5481-5488.
- SATHYENDRANATH, S., GOUVELA, A. D., SHETYE, S. R., RAVINDRAN, P., AND PLATT, T. (1991). Biological control of surface temperature in the Arabian Sea. *Nature*, 349:54-56.
- SCHUDLICH, R. R. AND PRICE, J. F. (1991). Diurnal cycles of current, temperature and turbulent dissipation in a model of the equatorial upper ocean. *Journal of Physical Oceanography*, in press.
- SHAY, T. AND GREGG, M. (1984). Turbulence in an oceanic convective mixed layer. *Science*, 310:282-285.
- SIEGEL, D. A. AND DICKEY, T. D. (1987). On the parameterization of irradiance for open ocean photoprocesses. *Journal of Geophysical Research*, pages 14,648-14,662.
- SIMPSON, J. J. AND DICKEY, T. D. (1981). Alternative parameterizations of downward irradiance and their dynamical significance. *Journal of Physical Oceanography*, 11:876-882.
- SMITH, S. D. (1988). Coefficients for sea-surface wind stress, heat flux, and wind profiles as a function of wind speed and temperature. *Journal of Geophysical Research*, 93:15,467-15,472.

STRAMMA, L., CORNILLION, P., WELLER, R. A., PRICE, J. F., AND BRISCOE, M. G. (1986). Large diurnal sea surface temperature variability: satellite and *in situ* measurements. *Journal of Physical Oceanography*, 16:827–837.

SVERDRUP, S. U. (1947). Wind-driven currents in a baroclinic ocean with application to the equatorial currents of the eastern Pacific. *Proceedings of the National Academy of Science*, 33:318–326.

TOGGWEILER, J. R. (1989). Is the downward dissolved organic matter (DOM) flux important in carbon transport? In BERGER, W. H., SMETACEK, V. S., AND WEFER, G., editors, *Productivity of the ocean: present and past*, pages 65–84. Wiley-Interscience.

TOOLE, J. M., PETERS, H., AND GREGG, M. C. (1987). Upper ocean shear and density variability at the equator during Tropic Heat. *Journal of Physical Oceanography*, 17:1397–1406.

TRENBERTH, E. K., BRANSTATOR, G. W., AND ARKIN, P. A. (1988). Origins of the 1988 North American Drought. *Science*, 242:1640–1645.

TSUCHIYA, M. (1979). Seasonal variation of the equatorial zonal geopotential gradient in the eastern equatorial Pacific. *Journal of Marine Research*, 37:399–407.

WACONGNE, S. (1989). Dynamical regimes of a fully nonlinear stratified model of the Atlantic Equatorial Undercurrent. *Journal of Geophysical Research*, 94:4801–4815.

WHITLEDGE, T. E., MALLOY, S. C., PATTON, C. J., AND WIRICK, C. D. (1981). *Automated nutrient analyses in seawater*. BNL 51398, Brookhaven National Laboratory, Upton, NY.

WILKERSON, F. AND DUGDALE, R. (1991). Measurements of nitrogen productivity in the equatorial Pacific Ocean at 150°W. *Journal of Geophysical Research*, in press.

- WILSON, D. AND LEETMA, A. (1988). Acoustic Doppler Current Profiling in the equatorial Pacific in 1984. *Journal of Geophysical Research*, 93:13947-13966.
- WOODS, J. D. (1980). Diurnal and seasonal variation of convection in the wind-mixed layer of the ocean. *Quarterly Journal of the Royal Meteorological Society*, pages 379-394.
- WUNSCH, C. AND GILL, A. E. (1976). Observations of equatorially trapped waves in Pacific sea level variations. *Deep Sea Research*, 23:371-390.
- WYRTKI, K. (1974). Sea level and the seasonal fluctuations of the equatorial currents in the western Pacific Ocean. *Journal of Physical Oceanography*, 5:91-103.
- WYRTKI, K. (1975a). El Niño - the dynamic response of the equatorial Pacific ocean to atmospheric forcing. *Journal of Physical Oceanography*, 5:572-584.
- WYRTKI, K. (1975b). Fluctuations of the dynamic topography in the Pacific Ocean. *Journal of Physical Oceanography*, 5:450-459.
- WYRTKI, K. (1981). An estimate of equatorial upwelling in the Pacific. *Journal of Physical Oceanography*, 11:1205-1214.
- WYRTKI, K. AND KILONSKY, B. (1984). Mean water and current structure during the Hawaii to Tahiti Shuttle experiment. *Journal of Physical Oceanography*, 14:242-254.
- ZANEVELD, J. R., KITCHEN, J. C., AND PAK, H. (1981). The influence of optical water type on the heating rate of a constant depth mixed layer. *Journal of Geophysical Research*, 86:6426-6428.